THE DISTRIBUTION OF ORGANIC MATERIAL IN MARS-ANALOGUE VOLCANIC ROCKS, AS DETERMINED WITH ULTRAVIOLET LASER-INDUCED FLUORESCENCE SPECTROSCOPY

CATHERYN HELENA RYAN

A THESIS SUBMITTED TO THE FACULTY OF GRADUATE STUDIES IN PARTIAL FULFILLMENT OF THE REQUIREMENTS FOR THE DEGREE OF MASTER OF SCIENCE

GRADUATE PROGRAM IN EARTH & SPACE SCIENCE
YORK UNIVERSITY
TORONTO, ONTARIO
JUNE 2019

Abstract

With continuous advancements in technology and space research, the priorities of space agencies and researchers who study the surface of Mars with robotics have shifted from characterizing the environment to detecting signs of life. Hence, research programs such as the Biologic Analog Science Associated with Lava Terrains (BASALT) research project (Lim et al., 2019) have been developed to test exploration capabilities and return samples from two Mars-analogue volcanic environments. Furthermore, new frontiers in planetary instrumentation are being explored with the goal of detecting organic materials in planetary and planetary-analogue rocks. One such tool, the York University ultraviolet laser-induced fluorescence (LIF) spectroscopy instrument, was used in this research to detect and characterize the distribution of potential organic biosignatures in samples returned from two BASALT mission deployments. These samples represent a range of alteration conditions found in the volcanic environments of Hawai'i Volcanoes National Park and Craters of the Moon National Monument. LIF mapping and LIF time-resolved measurements were taken of nine basaltic samples. Samples were also analyzed using scanning electron microscopy with electron-dispersive x-ray spectroscopy (SEM-EDS) to characterize the mineralogy present at fluorescent points-of-interest and confirm the presence of carbonaceous material. Finally, He-gas pycnometry and micro-computerized tomography were used to determine the porosity of the samples, which could be compared to the results from LIF and SEM-EDS measurements. LIF was shown to be a useful tool for *in situ* measurements of Mars-analogue samples, and could be applied to future Mars missions.

Dedication

I dedicate this thesis to all the excellent teachers and mentors I've had since the age of five, for encouraging me and fostering a love of education that has led me to a Master's degree and beyond.

Acknowledgements

This work has been a huge undertaking personally and professionally, and I could write a whole separate thesis about how grateful I am for the help I've received.

First and foremost, I have to thank my supervisor, Dr Michael Daly. He took a chance on me, deciding to see past my academic difficulties on paper to the potential I had waiting to spill over. His guidance and mentorship gave me the opportunity to push my comfort zone beyond what I thought capable. I have grown immeasurably as a researcher and a person over the last two-and-a-half years, and I have Mike to thank for a lot of that. It has been a privilege to work with him.

I must acknowledge my unofficial co-supervisors, Dr Greg Slater and Dr Allyson Brady, of McMaster University, for creating the space in this project for me and providing me with invaluable direction throughout. Additionally, the rest of the NASA BASALT Science Team, for giving me useful insights and a sense of how I fit into the broader picture. Darlene, Shannon, Scott, Rick, and Charles have been especially helpful with feedback during team meetings.

The Planetary Instrumentation Lab at York has been my home over the course of this degree, and numerous people have helped me with various aspects of my research, from understanding MatLab to understanding lasers to improving my writing. I owe a massive debt of gratitude to Keagan Lee, for his exceptional work as my assistant during the summer of 2018; without him, this could have taken much longer. Emmanuel, Pamela, Jim, Cosette, Dylan, Beth, and Kristen all contributed in some way with their expertise and mentorship. To everyone else in PIL, your friendship and support has meant so much to me.

Personally, I wouldn't be here without the help of an incredible social support network. Singing Out and QUIPS have given me a community I didn't even know I needed and friends I will have for life. My therapists have been integral to my well-being. My friends, especially Adeene, have helped with proofreading, motivation, and hugs when needed.

Finally, to my family, especially my parents. Their steadfast support and love have meant the world to me. I don't have enough words to describe what having these incredible people in my life has done for me, but I know I wouldn't be who or where I am

today without them. To Ellie, as well. She may not be much of a researcher, but having a wagging tail and many kisses to come home to helps make each day worth it. I love you.

Table of Contents

List of Tables

List of Figures

1 Introduction

1.1 Study Motivations

1.1.1 An introduction to planetary analogue missions

Planetary surface missions, whether crewed or robot-driven, are an enormous undertaking by any space agency. The cost and risk factors are huge, necessitating many field tests on Earth before implementation in space.

Planetary analogue missions, with a crew of astronauts, robots, or some combination thereof, therefore provide the opportunity to test new mission concepts and train personnel for future missions. They operate under simulated Earth-to-space conditions, involving physical separation between a mission control centre and the field site as well as differing degrees of autonomy in the field. Importantly, an analogue mission provides quick feedback on the effectiveness of any new operational conditions.

Any field campaign, especially those including sample return, can provide us with real science results. An Earth-based science laboratory has a huge advantage in accuracy and versatility over any field equipment, and can be used to confirm or reject hypotheses developed based on *in situ* data. Additionally, the examination of analogue environments gives a better understanding of the processes that formed them and their potential to support life. These data are crucial for developing our understanding of other planetary bodies.

1.1.2 Mars instrumentation

Space agencies such as the National Aeronautics and Space Administration (NASA), the Canadian Space Agency (CSA), and the European Space Agency (ESA) have conducted several robotic missions to Mars over the past decades. With the improvement of technology, their goals have shifted from understanding the geological environment of Mars, to assessing its habitability, to actively searching for signs of extant or extinct life (Mars Exploration Program Analysis Group & Hamilton, 2015).

Some crucial considerations in the design and inclusion of an instrument on a Mars mission are the need for sample preparation, the distance from which the instrument can be operated, and whether the analyses cause damage to the sample. Laser-induced fluorescence (LIF) spectroscopy is a non-destructive, stand-off technique that requires

minimal sample preparation, making it ideal for such conditions. Its ability to detect the presence of organic matter in volcanic samples is a major focus of this study. If proven successful, this study will further demonstrate the applicability of LIF in a Mars-analogue setting, building on the work of Abedin et al. (2015), Eshelman et al. (2015, 2016), Groemer et al. (2014), Hamilton et al. (2016), and Smith et al. (2014).

1.1.3 Characterization of basalt as a habitable environment

This study uses samples of basalt collected during the 2016 deployments of the NASA Biologic Analog Science Associated with Lava Terrains (BASALT) analogue missions. These samples represent a range of alteration and environmental conditions, and thus have differing geochemical and physical properties. The other major focus of this research is to characterize the locations of any organic material within the rocks, and demonstrate their relationships to the different micro-habitats available in these samples. This work could show that certain conditions within a basaltic environment are preferred by micro-organisms for colonization, complementing the research of Cockell et al. (2019).

1.2 Study Objectives

This research has dual, complementary objectives: to assess the usefulness of LIF as a technique for detecting organic biosignatures in Martian-analogue volcanic rock samples; and to determine the relationships between the basalt's physical and geochemical characteristics and the distribution of organic biosignatures within it.

1.3 Thesis Outline

This thesis is structured as follows. Chapter 1 will briefly introduce the concept of analogue planetary missions and their role in furthering planetary science research. It will also cover the motivations behind the dual objectives of this study: instrumentation and astrobiology. Chapter 2 will discuss biosignatures in the framework of astrobiological research. Chapter 3 will provide an overview of the NASA BASALT research project, including the geological context of the mission deployment sites from which my samples were collected. Chapter 4 will give a more in-depth discussion of planetary instrumentation, and introduce the scientific mechanisms of LIF. Chapter 5 will further discuss the geological contexts of the samples used in this study, then overview the major

physical properties of each individual sample. Chapter 6 will introduce the experimental design, instrumentation, and methodologies of this study, including sample preparation, visual characterization, LIF, scanning electron microscopy (SEM), and porosity measurements. Chapter 7 will review the results of all experiments on a sample-by-sample basis, and conclude with a table that summarizes these results for comparison between samples. Chapter 8 will discuss the relationships between geological and fluorescence properties of the samples. It will also include a comparison of these data with the biological study of the same samples by Cockell et al. (2019). Finally, Chapter 9 will summarize the major findings of this research and their contribution to the field, and include recommendations for the continuation of this work.

2 Biosignatures in Astrobiology

A biosignature is a trace within the geologic record of past or extant life. The most common or obvious example of a biosignature is a fossil, but a fossil is almost always from a multi-cellular organism. Astrobiologists tend to focus on more subtle chemical or microscopic evidence of single-celled creatures. There are three general categories of biosignatures: geochemical, including isotopic and biomineralization; structural, including macroscopic structures like stromatolites; and organic, including complex organic molecules that are only produced biogenically. This research focuses on organic biosignatures, but geochemical and structural will be reviewed below as well.

2.1 Geochemical and Structural Biosignatures

Isotopic biosignatures are typically presented as enriched or depleted ratios of certain stable isotopes of bio-relevant elements: carbon, hydrogen, nitrogen, oxygen, phosphorous, and sulfur (CHNOPS), as well as iron. These are all elements that microbes utilize during their metabolism, which causes isotopic fractionation that can be distinct from fractionation occurring during abiotic processes.

Biomineralization is the process wherein a microbe uses parts of a mineral as its energy source, and converts it through metabolism into another mineral. A prominent example and possible Mars analogue is the Río Tinto river in Spain. Río Tinto represents an extremely mineralogically and hydrologically active environment, with surprisingly high biodiversity (Amils et al., 2014). Río Tinto originates in the core of the Iberian Pyrite Belt (IPB), which contains massive bodies of iron, copper, zinc, and lead sulfides, formed by hydrothermal activity. Hence, the river contains high concentrations of dissolved heavy metals, and a low pH of approximately 2.3 due to acid mine drainage activity. The Iberian Pyrite Belt Subsurface Life Detection (IBPSL) team drilling projects showed that the characteristic dynamic geochemistry and dissolved heavy metals were due to a large underground bioreactor. Microbes process iron, metal sulfides, nitrate, sulfate, and CO_2, driving the unique water conditions at the river's surface. As all of the conditions present at Río Tinto were or are available on Mars, Río Tinto gives us the hypothesis that large-scale biomineralization could be a viable process on Mars.

Structural biosignatures, such as microtubules or stromatolites, can be observed in rocks through microscopy or even with the naked eye. They are formed when microbes colonize the surface or interior of a rock and are subsequently mineralized, or leave behind void spaces that could not be abiotically generated. As their detection typically requires high-magnification microscopy and the ability to break open a sample for examination, their discovery by a Mars rover is currently considered impossible.

Stromatolites are well-regarded as excellent biosignatures on Earth, and possibly some of the oldest (Wacey, 2010). They form from permineralized biofilm layers in shallow water, and can be recognized by their distinctive laminae and shapes.

Microtubules in basaltic and impact glass were studied by Izawa *et al.* (2010), Banerjee *et al.* (2011), and Sapers *et al.* (2015 a; 2015 b; 2014). Microtubules in glasses form when microorganisms dissolve the rock as they extract bio-essential elements during chemolithotrophic metabolism. These micron-scale structures are detectable in petrographic microscopy. As similar crystal structures can form abiotically, it is important in these studies to determine other lines of evidence to support their biogenicity.

2.2 Organic biosignatures

Possibly the best biosignatures available are complex organic molecules that are remnants of cellular structures or microbial metabolism. While many complex organics can be formed abiotically (e.g., amino acids in meteorites (Cronin & Pizzarello, 1983) or polycyclic aromatic hydrocarbons [PAH] in the interstellar medium (Voit, 1992)), certain molecules like photosynthetic pigments, phospholipid cell membranes, and deoxydibonucleic acid (DNA) are unique to life. A major concern, however, is the survival of these molecules over geologic time and exposure to the high radiation of the Martian surface.

There is evidence that certain biomolecules can become bound to clay mineral matrices through adsorption and therefore be better preserved in the rock record. Numerous studies (Blanco et al., 2011; Khanna & Stotzky, 1992; Orofino et al., 2010) have shown that clay minerals, with their partially-charged molecular surfaces, can adsorb charged organic molecules and even act as catalysts in the creation of larger organic molecules. Rapid burial of biomolecules within a clay would aid in preservation, and the

existence of chemical equilibrium between the organics and clays would discourage further chemical degradation. As clays are widespread on Mars (Bishop et al., 2008; Ehlmann et al., 2009, 2011; Michalski et al., 2009; Poulet et al., 2005), including at the Mars 2020 landing site in Jezero Crater (Ehlmann et al., 2008; Fassett et al., 2007; Goudge et al., 2015a), these findings are especially relevant to the search for biosignatures on the Martian surface.

Two studies, Baqué *et al.* (2016) and Dartnell and Patel (2014), experimentally examined the issue of organic molecule preservation under Martian conditions. Dartnell and Patel (2014) showed that photosynthesis-related molecules degraded relatively quickly when exposed to the surface, while tryptophan and carotenoid pigments were still highly detectable after multiple days. This means that a rover with a fluorescence-detecting instrument could potentially expose sub-surface organic molecules through drilling or wheel scrapes, and still have time to measure these molecules before they degrade completely. In a complementary study, Baqué *et al.* (2016) revealed that Martian regolith has some protective effects against damaging UV radiation. The molecule β-carotene was always detectable, no matter the thickness of the regolith, while photosynthetic pigments were strongly bleached in all experiments.

3 The Biologic Analog Science Associated with Lava Terrains Research Project

Habitability is defined as the environmental parameters, both chemical (the availability of essential elements and the conditions required for chemical reactions to proceed) and physical (temperature, pressure, humidity, radiation), necessary to sustain life. These are in turn delineated by the biological constraints exhibited by known terrestrial extremophiles (L. Dartnell, 2011; Preston & Dartnell, 2018). Astrobiologists must accordingly include investigations into environmental conditions in their research.

Environmental research is focussed on analogue environments that closely mimic the past or present conditions of another planet's surface. Environments fall into a few broad categories. In extreme environments, such as arid deserts or volcanic hydrothermal pools, organisms must develop similarly extreme coping mechanisms in order to survive. Gentler habitats like lakes and rivers or coastal areas have provided the best preservation of fossils on Earth. Furthermore, scientists use environmental simulation experiments to demonstrate what could happen to biosignatures exposed to the current harsh surfaces of planetary bodies, as discussed above (Baqué et al., 2016; L. R. Dartnell & Patel, 2014).

Beyond geological and biological investigations of environmental analogues, it is imperative to simulate the exploration technologies and conditions appropriate to a planetary surface mission. Numerous projects have involved the deployment of human and/or robotic explorers to Martian analogue environments under simulated constraints. These include the Desert Research And Technology Studies (DesertRATS), conducted from 1997 to 2011 in the high desert of northern Arizona (Ross et al., 2013); the CanMars Mars Sample Return analogue mission in southern Utah in 2015 and 2016 (Osinski et al., 2018); the MARS2013 Mars Analogue Mission in Morocco (Groemer, Soucek, et al., 2014); and the Hawai'ian Space Exploration Analog and Simulation (HI-SEAS), ongoing since 2013 (Binsted, 2015). To expand upon these and other studies, the NASA Biologic Analog Science Associated with Lava Terrains (BASALT) research project was developed in 2015 (Lim et al., 2019).

BASALT combines simulated crewed missions to Martian-analogue volcanic environments with returned-sample science. Its goals cover both research into human

factors, technology, and logistics during a mission simulation (Beaton et al., 2019; Stevens et al., 2019), and scientific investigation of the biologic habitability of volcanic environments. Three 3-week deployments were conducted over the course of the project. In 2016, two lava flows at Craters of the Moon National Monument, Idaho, USA were used as field sites. Two deployments to Hawai'i Volcanoes National Park were conducted in 2016 at Mauna Ulu, and 2017 at Keanakako'i Overlook and Kilauea Iki (Hughes et al., 2018).

3.1 BASALT mission deployments

BASALT deployments operated under simulated Mars conditions, with an elaborate communication architecture between the field and Mission Control. The field sites were chosen months in advance by the Science Team members. Through examining aerial photography and satellite remote-sensing data of the overall field areas (each overall field area being approximately 0.5 to 2 km^2; see fig. 3.1), they would select polygons about 2000-3000 m^2 around sites of potential interest: active or relict fumaroles, or unaltered lava flows. Meanwhile, the Exploration Team would develop the different scenarios to test in the field: technologies like light detection and ranging (LIDAR), panoramic cameras, virtual/augmented reality headsets, and changes in communication constraints.

During these deployments, ten Mission Days (MD) were completed, involving a full work-flow of two Extra-Vehicular (EV) crew members going to the day's chosen field site to evaluate and collect samples. Each MD, the two EV crew would enter that day's field site with the goal of collecting a sample suite concurrent with the MD's stated objective, such as a suite of samples from an active magmatic fumarole with a sub-surface temperature of greater than 85 ^oC. The EV crew would be equipped with numerous technologies, including chest-mounted video cameras, audio communication, Wi-Fi - enabled point-and-shoot cameras, global positioning system (GPS) trackers, and instrumentation such as temperature probes, infrared (IR) cameras, and portable Raman, laser-induced breakdown spectroscopy (LIBS), and Fourier-transform IR (FTIR) spectrometers. All of these data would be transmitted directly to the two In-Vehicle (IV) crew members located at an on-site control centre. As EV and IV were both on simulated

Mars, they could communicate in real-time using audio and text. Their communications and data would also be shared with the remote Science Team in Mission Control, but a time delay of five or fifteen minutes would be applied in each direction to simulate the real transmission delay between Earth and Mars.

In Mission Control, the Science Team would watch and evaluate the data received from EV and IV about the field site, discussing and ranking any potential samples. Their rankings and notes, along with any requests for more information, would be relayed to IV and then EV through the delayed-communication network. Ultimately, although the EV crew collected the samples, the Science Team was responsible for choosing them. Samples were collected using sterile methods to prevent contamination, and placed immediately in a deep freezer upon their return to Mission Control. Each day's sample suite was collected from within an approximately 1 m^2 area and were all considered duplicates.

The samples were distributed at the end of the mission to representatives of each sub-team within the Science Team (biology, organic geochemistry, geology, archive), and returned to their respective laboratories for further analyses. Samples used in my study were originally returned to the Environmental Organic Geochemistry Laboratory in the School of Geography and Earth Sciences at McMaster University, Hamilton, Ontario. They were then transferred to the Planetary Instrumentation Laboratory, Centre for Earth and Space Science, at York University.

3.2 BASALT field sites

The field sites of Mauna Ulu (MU) and Craters of the Moon National Monument (COTM) (fig. 3.1; Lim et al., 2019) were chosen on the basis of their representing different Martian volcanic environments (Hughes et al., 2018). Both sites share similarities: sourced from mantle plume hot spots, erupting as fissure eruptions along magmatic rift zones, and with similar surface expressions such as a'a and pahoehoe flows and spatter ramparts (Hughes et al., 2018). However, they have significant differences in composition and weathering environments, with Hawai'i being exposed to a much warmer, rainier, and consistent climate than the cool, dry, seasonal setting of COTM.

Hawai'i's active volcanism is representative of a hypothesized early Mars environment, dominated by volcanism and impact events occurring in the presence of

liquid water (Clifford & Parker, 2001; Poulet et al., 2005; Squyres & Kasting, 1994; Westall et al., 2015). Mauna Ulu is a small shield volcano on the flanks of the much larger Kilauea volcanic system on the island of Hawai'i. It formed during continuous eruptions from 1969 – 1974 in the Kilauea East Rift Zone, and was, at the time, the longest-lasting and most voluminous eruption in more than 2200 years (Hawaiian Volcano Observatory, 2017). A prominent feature of the Mauna Ulu volcano continuing to 2016 is the active and relict meteoric fumaroles present on its flank. Studies have shown both that ocean island basalts, such as those in Hawai'i, are most similar in composition to Martian basalts (Schiffman et al., 2006; Seelos et al., 2010); and that the alteration minerals produced by Kilauea's fumaroles are similar to hydrothermal alteration products detected on Mars (Gerard & McHenry, 2012).

Despite being geologically quite young, Craters of the Moon represents the current, aged Mars environment. The Snake River Plain caldera-forming eruptions began about 15 million years ago, and this hot spot was positioned beneath south-central Idaho approximately 10-11 million years ago (Kuntz et al., 1982). The North American plate then moved to its current position and the hot spot became Yellowstone National Park. Residual heat from the hot spot at COTM was re-liberated during the Basin-and-Range rifting period in the southwestern United States, creating the many over-lapping lava flows present today in the area (Kuntz et al., 1982). The two lava flows examined, Big Craters (BC) and Highway Flow (HF), are 2100 – 2300 years old, and are composed of chiefly pahoehoe or a mix of pahoehoe and a'a flows, respectively (Kuntz et al., 1982).

As a Mars analogue, COTM offers numerous similarities. Its landscape features include caves, lava tubes, and the basaltic terrain and geomorphology associated with large volcanic provinces on Mars. Additionally, the basalts of COTM have a high phosphate content, relevant both because Martian basalts have a generally higher phosphate content than Earth's, and phosphorous is a bio-essential element (Adcock et al., 2018). COTM's basalts undergo chemical weathering as a dominant process, freeing up valuable nutrients for microorganisms (Adcock et al., 2018).

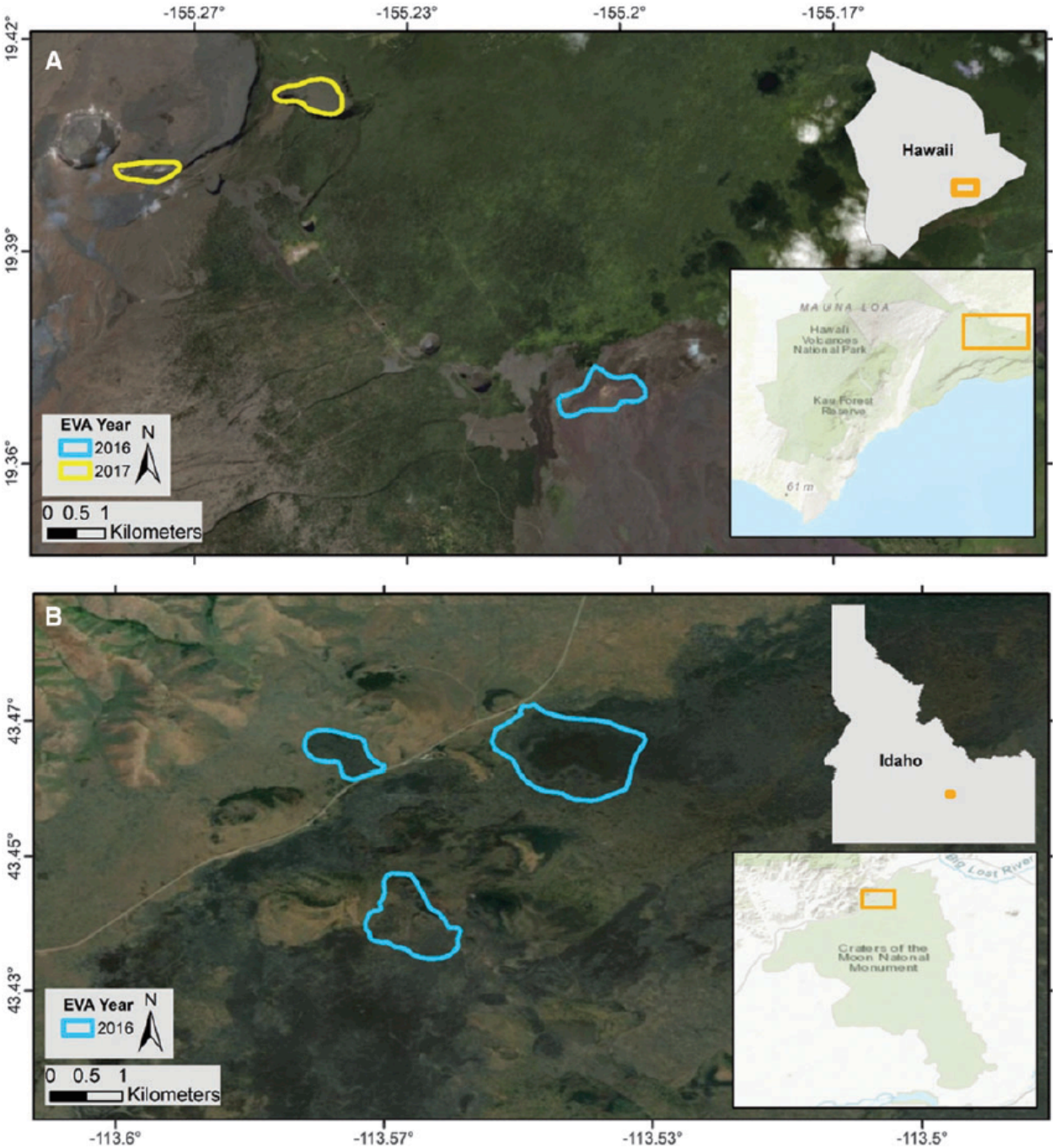

Figure 3.1 Maps of the field sites explored during the BASALT deployments (from Lim et al., 2019). Top: The Big Island of Hawai'i, with location of deployment highlighted. The Keanakako'i (left) and Kilauea Iki (right) sites are outlined in yellow (2017 deployment), and Mauna Ulu site is outlined in blue (2016 deployment). Bottom: the region of Idaho with Craters of the Moon National Monument highlighted. Clockwise from top left are the Highway Flow, North Crater Flow, and Big Craters Flow, outlined in blue (2016 deployment).

4 Planetary Instrumentation

Planetary instrumentation is highly specialized: adapted for the extreme environments of other planetary bodies, and for the specific tasks called for by the mission. Analytical instruments and imaging systems are designed to both broadly characterize a planetary environment and pinpoint the samples most likely to host biosignatures. They must then target these samples, measuring a variety of different attributes in the hopes of detecting the most minute signs of previous or current habitation.

Instrument concepts are applied to analogue missions to assess their ability to operate in the field and provide acceptable results. Samples collected in the field are then validated in a laboratory setting, with more complex and precise methods. Space agencies such as NASA, ESA, CSA, and the Russian Space Agency (Roscosmos) use these tests from the lab and the field to develop instrumentation payloads for Mars missions. As technology advances, agencies can move from attempts to define the Martian surface to targeting specific biosignatures.

4.1 Current and Future Mars Missions

4.1.1 Mars Exploration Rovers and Mars Science Laboratory

There have been three true rover missions to Mars thus far: the Mars Exploration Rovers (MER), *Opportunity* (2003 – 2019) and *Spirit* (2003 – 2010), and Mars Science Laboratory (MSL) or *Curiosity*, which landed in 2012 and continues operations today.

The MER instrumentation suite is identical across both rovers, and adapted for the primary goal of studying the rocks and soils on Mars that hold clues to past water. While astrobiology was not a stated goal, "following the water" is a key strategy for preliminary astrobiological surveys, in order to determine if an environment was or is habitable (Mars Exploration Program Analysis Group & Hamilton, 2015). To that end, two chemical analysis instruments, the Alpha Particle X-Ray Spectrometer (APXS) (Rieder et al., 2003) and the Mossbauer Spectrometer (Klingelhöfer et al., 2003) were included, in addition to multiple cameras for imaging rocks and terrain.

The results from the scientific experiments conducted by both rovers showed that their respective environments did contain hydrated minerals (Christensen & Ruff, 2004;

Klingelhöfer et al., 2004; McLennan et al., 2005; Ming et al., 2008; Rieder et al., 2004; Squyres et al., 2004). Additionally, *Spirit* documented outcrops showing rock coatings (Ming et al., 2008) and amorphous silica sinter deposits (Ruff et al., 2011), both of which could contain biosignatures if examined with tools available on Earth (Haskin et al., 2005; Ruff & Farmer, 2016). The rovers used their analytical instruments to determine mineralogy and geochemistry. While mineralogy does have the potential to be a biosignature (see ch. 2.1), it would require additional biosignature identification, such as the presence of complex organic molecules or biogenic morphologic structures, before a confirmation of biogenicity could be made. Such confirmation is impossible with APXS or Mossbauer.

Curiosity's instrument payload built and expanded upon the MER legacy, with newer, more sophisticated analytical tools. Along with an updated APXS (Campbell et al., 2012), MSL's science suite includes ChemCam (LIBS and Remote Micro-Imager [RMI]) (Maurice et al., 2012), CheMin (X-Ray Diffraction Spectroscopy [XRD]) (Blake et al., 2012), and Sample Analysis at Mars (SAM) with two modes of Gas Chromatography-Mass Spectrometry (GC-MS) and Tunable Laser Spectrometry (TLS) (Mahaffy et al., 2012). CheMin, ChemCam, and APXS are used together to determine mineralogy and bulk elemental composition in order to develop a chemostratigraphy model for Gale Crater. ChemCam is especially useful, as it has the ability to detect organic carbon in rocks.

The powerhouse of sample analysis in this suite is SAM. SAM is capable of detecting volatile organic compounds down to 10 ppb by mass, and do some determination of the isotopic composition of carbonaceous material. It can use wet chemistry methods to examine up to nine samples containing carboxylic acid, nucleo bases, or amino acids (Mahaffy et al., 2012). One of the most exciting discoveries since *Curiosity's* mission began is the detection of organic sulfide compounds in sediments: thiophene, 2- and 3-methylthiophenes, methanethiol, and dimethylsulfide (Eigenbrode et al., 2018). While these molecules are not in and of themselves biosignatures, they show sulfurization of organic macromolecules as being a once-active process on Mars. As sulfurization provides long-term protection against structural transformation and oxidation, it enhances preservation of these macromolecules.

The MER and MSL missions have not had biosignatures as their top priorities, but have been able to conclusively show that their respective environments once held liquid

water and therefore could have been habitable (Christensen & Ruff, 2004; Grotzinger et al., n.d.; Haskin et al., 2005; Martín-Torres et al., 2015; Milliken et al., 2010; Rieder et al., 2004; Squyres et al., 2004; Williams et al., 2013). The next two rover missions bound for Mars, NASA's Mars 2020 rover and ESA's ExoMars rover, will be equipped with instrument suites more suited for biosignature detection.

4.1.2 Mars 2020 and ExoMars

The Mars 2020 rover is projected to launch in July 2020 and land in February 2021 (Chang, 2018). Its landing site will be Jezero Crater, a site believed to have once hosted a lake and a river system, as well as volcanic and impact materials (Goudge et al., 2015b, 2017; Schon et al., 2012). This environment is well-suited to host evidence of past life, the finding of which is the main goal of the Mars 2020 mission. Mars 2020 will be built on the same chassis design as MSL, but support a new suite of instruments that expand MSL's capabilities.

The three main analytical instruments on Mars 2020 are:

- Planetary Instrument for X-Ray Lithochemistry (PIXL), a combination X-Ray Fluorescence Spectrometer (XRF) and micro-imager (Allwood et al., 2016);
- SuperCam, an expansion of ChemCam that incorporates 532 nm Raman spectroscopy and Time-Resolved Fluorescence (TRF) along with its 1064 nm IR laser for LIBS (Roger Craig Wiens et al., 2017); and
- Scanning Habitable Environments with Raman and Luminescence for Organics and Chemicals (SHERLOC), a 248.6 nm deep-ultraviolet (UV) Raman and fluorescence spectroscopy instrument (Beegle et al., 2015).

The incorporation of Raman into the instrument suite is novel to Mars missions, and deep-UV Raman specifically has been shown to be useful for the detection of organic molecules preferentially, compared to minerals (Abbey et al., 2017; Eshelman et al., 2014, 2015; Skulinova et al., 2014a). PIXL will be used to determine the abundance and distribution of elements correlated to visible textures in rocks and detect reduction/oxidation anomalies as potential chemical biosignatures (Allwood et al., 2015), working similarly to Electron Dispersive X-Ray Spectroscopy (EDS). In simulation tests, PIXL techniques have demonstrated the detection of chemical biosignatures in sandstone (Allwood et al., 2016), and shown that elemental distribution in stromatolites is likely

concurrent with microbial mats (Allwood et al., 2009). Finally, SuperCam is a stand-off instrument that can be operated up to 12 m away from the target rock, allowing for quick initial assessment of a sample. As with ChemCam, it uses LIBS to determine the bulk elemental composition of the sample, as well as ablate some surface dust. The Raman/TRF component of SuperCam is more suited to mineralogy than organic detection, acting complementary to SHERLOC (R C Wiens et al., 2017).

Rosalind Franklin, part of the ExoMars joint project between ESA and Roscosmos, is a rover also set to launch in July 2020 (ESA Media Relations Office, 2016). It will land in Oxia Planum, a region containing massive amounts of phyllosilicate minerals, fluvial morphologies such as a delta fan, and rocks from a wide age range (Quantin et al., 2015). ExoMars will host an instrument payload with some similar capabilities to the NASA rovers, as well as a drill capable of drilling up to 2 m into the subsurface and collect drill core samples approximately 3 cm long * 1 cm diameter (Vago et al., 2017).

Rosalind Franklin's analytical suite (the Pasteur payload) includes:

- Mars Multispectral Imager for Subsurface Studies (Ma_MISS), a microscopic imager and infrared spectrometer coupled with the drill, used to identify minerals within the borehole walls (De Sanctis et al., 2017);
- MicrOmega, a visible-near-IR spectrometer used to observe crushed sample material to characterize composition and structure at a grain-size level (Bibring et al., 2017);
- Raman Laser Spectrometer (RLS), a 532 nm green laser Raman instrument to further constrain mineralogy (Rull et al., 2017); and
- Mars Organic Molecule Analyser (MOMA), a GC-MS and laser desorption ionization mass spectrometer (LDI-MS), that operates similarly to MSL's SAM to look for organic compounds within rock samples, especially those from the drill core (Goesmann et al., 2017).

While Ma_MISS, MicrOmega, and RLS are all best suited to understanding the mineralogy and geochemistry of samples, MOMA is optimized for organic detection. Its LDI-MS technique is not as destructive as pyrolysis-based GC-MS, meaning non-volatile organic compounds can be detected before being oxidized or destroyed by perchlorates during the heating process (Goesmann et al., 2017; Goetz et al., 2018). Especially with the

access to sub-surface materials provided by the drill, the Pasteur suite offers a novel approach to the search for biosignatures on Mars.

4.2 Fluorescence and Raman Spectroscopy for Planetary Missions

Fluorescence and Raman spectroscopy work on similar principles: a sample molecule is excited by photons from a laser, and light is re-emitted (in a longer wavelength) as the molecule returns to its ground state (Figure 4.1). While Raman works on the principle of inelastic scattering of incoming light as it interacts with chemical bonds, fluorescence involves the absorption of incident photons by molecules and the conversion of this energy within the molecule before the molecule's return to ground state. Both techniques give results that show the presence of certain chemical bonds, such as C-C, C-H, SOx, etc., allowing for the identification of the molecular species present.

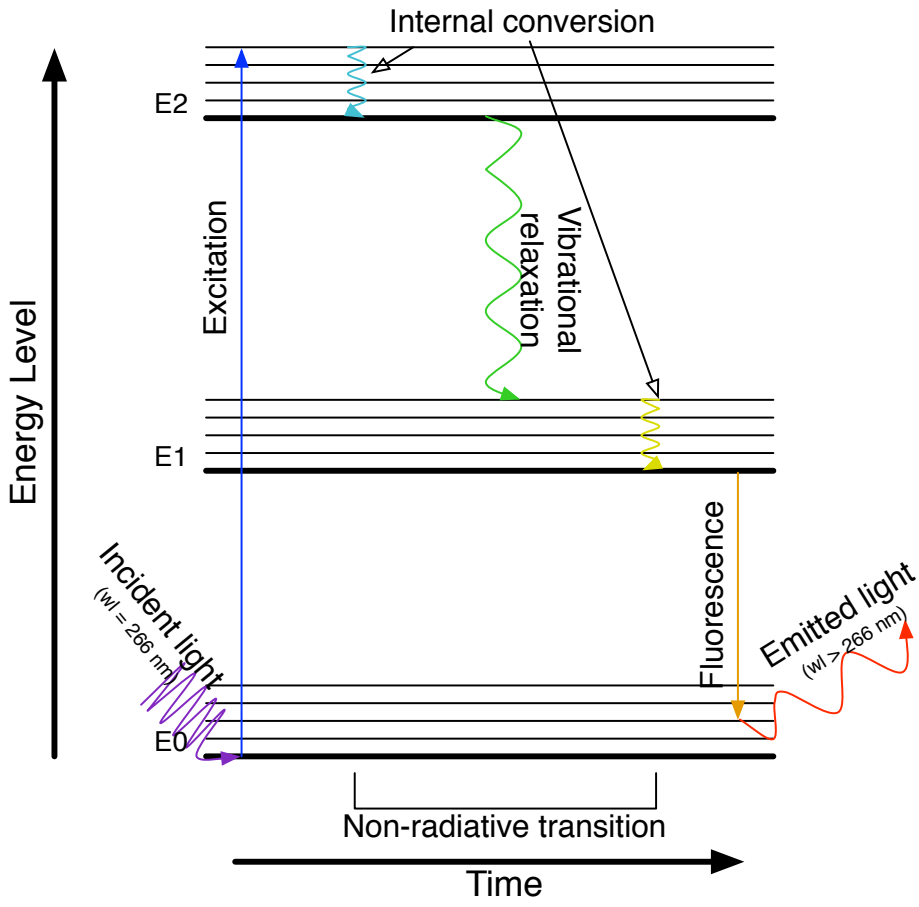

Figure 4.1 Energy (Jablonski) diagram of the mechanics of fluorescence emission by a molecule.

Different laser excitation wavelengths are used for different purposes; for example, longer wavelengths (visible and IR) often produce results overwhelmed by fluorescence from organics present, so visible and IR Raman is best suited for mineral identification where the fluorescence can be deleted. A deep-UV wavelength produces the best separation between

fluorescence and Raman effects in organic-containing samples, making it ideal for fingerprinting organic compounds (Beegle et al., 2015; E. Eshelman et al., 2014, 2015, 2017; Skulinova et al., 2014b).

Time-resolved fluorescence is another associated technique. As energy is absorbed and transformed by molecules, the emitted fluorescence signal will grow and decay over a period of time (nanoseconds to microseconds) (Figure 4.2). A detector with time-gating and time-delay capabilities in the nanosecond range can capture both the intensity of fluorescence at a range of wavelengths and the differences in intensity at each wavelength over time. This technique is especially useful for distinguishing mineral signals from organics in a mixed sample, as organic fluorescence decay times are much shorter (<10 ns) than mineral fluorescence decay times (Eshelman et al., 2015, 2017; Lymer, 2017; Skulinova et al., 2014a). This is due to both an inverse relationship between fluorescence absorption (and subsequent emission) intensity described in Eshelman (2016), and the common presence of trace amounts of rare earth or transition elements in minerals, which have extremely long decay times (Eshelman, 2016).

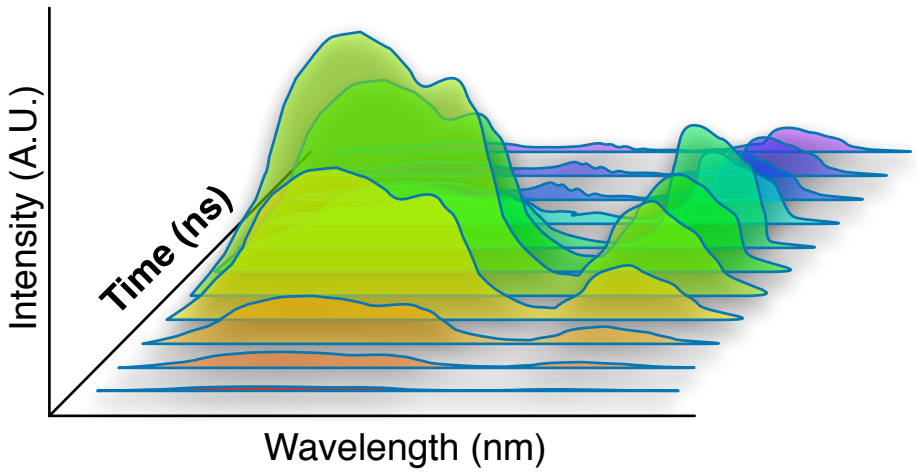

Figure 4.2 Diagram of time-resolved fluorescence

5 Samples

Out of the sixteen samples returned to York University from the 2016 BASALT deployments to Hawai'i and Idaho, nine were chosen for my analyses. These were based on communications within the BASALT science team before I began my work, where samples were prioritized by each research group. Therefore, my samples' replicates have all already been analyzed by the other research groups, allowing us to correlate results.

5.1 Hawai'i 2016

The 2016 BASALT deployment to Hawai'i Volcanoes National Park occurred from 1 to 18 November, 2016. As described in Chapter 3, the mission took place on the flanks of the Mauna Ulu volcano (Figure 5.1). Before the mission began, potential sampling targets were discussed amongst the BASALT science team, who ultimately laid out plans to collect three sample types for analyses: active meteoric fumarole, relict meteoric fumarole, and unaltered basaltic lava. These three types were chosen to represent a range of possible habitable environments.

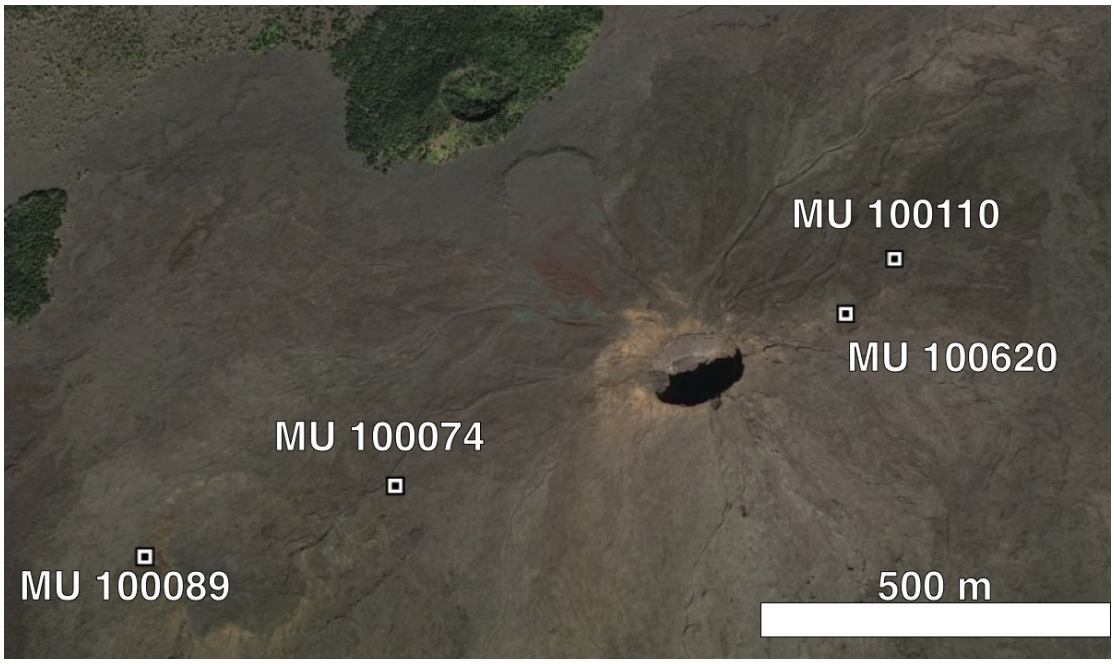

Figure 5.1 Locations of Hawai'i 2016 sample sites on the flanks of the Mauna Ulu volcano (images from Landsat/Google Earth).

The Mauna Ulu lavas present as shelly to dense pahoehoe flows. Lavas are more primitive in composition, deriving directly from a mantle plume (Hughes et al., 2018). These tholeiitic lavas contain 3 – 16 per cent by volume (vol%) olivine phenocrysts and microphenocrysts (Vinet & Higgins, 2010). The groundmass is composed of microcrystalline plagioclase, clinopyroxene, Ti-magnetite, and amorphous glass. The forsterite composition of the olivines was measured to be between 78 and 90 per cent by weight (wt%), concurrent with bulk rock compositions showing high magnesium content (Vinet & Higgins, 2010).

From Hughes et al., (2018), fumarolic alteration is caused by the release of steam and/or magmatic gases (H2O, CO_2, SO_2, HCl, HS, and F) during or following emplacement of volcanic features. The low pH of these gases cause the chemical breakdown of primary minerals such as plagioclase into clay minerals. The gases will also occasionally precipitate pure minerals on to the surfaces of rocks, such as sulfur crystals. The distinction between magmatic and meteoric fumaroles is the source of water: magmatic fumaroles are formed from water already contained within the magma, while meteoric fumaroles are sustained by rainwater and other surface sources. Our fumarolic samples were collected from both active and relict fumaroles on Mauna Ulu. Active fumaroles were clearly distinguished from relict by the presence of active steam venting, and confirmed with the use of the IR hand-held camera for capturing the temperature (Sehlke et al., 2019). The active fumaroles had temperatures at least 20 ^{o}C higher than the ambient ground, while relict fumaroles showed no significantly higher heat.

Both active and relict fumaroles could host common mineral deposits including native sulfur, sulfides, sulfosalts, sulfates, halides, oxides, hydroxides, carbonates, and borates (Hughes et al., 2018). While fumaroles do go extinct or dormant, they can still host some active alteration, aided still by meteoric water. Relict fumaroles will also often include alteration products with secondary materials introduced by fluids or directly deposited as sublimates (Hughes et al., 2018).

In contrast, unaltered basalt samples from both Hawai'i and Idaho consist of rocks collected from outcrops that have not been altered by volatiles (Hughes et al., 2018). These outcrops were located away from active fumaroles, and may have been protected from weathering.

Below, Table 5.1 summarizes the major physical characteristics of the Hawai'i 2016 (HI2016) sample suite, which includes two active fumarole samples, one relict fumarole samples, and one unaltered sample. Following that, photographs of each sample and its sampling context in the field are presented in Figures 5.2 to 5.5.

Table 5.1 Physical characteristics of analyzed samples from the Hawai'i 2016 (HI2016) sample suite. The "MU" in each sample number is in reference to Mauna Ulu, the volcano from which these samples were collected.

Sample	Slides analyzed	Sample type[1]	Date collected[1]	Notes from the field[1]	Figure	Colour	Alteration characteristics	Approx. median vesicle diameter (mm)	Approx. vesicle size range (min/max) (mm)
MU100074	A, B, E	Active meteoric fumarole	08/11/2016	Large patches of white precipitate. Mostly unaltered, other than some deep red syn-emplacement alteration. Temperature was ~ 60 – 65 °C.	5.2	Orange, red-brown, with some black matrix	White crystalline material (WCM) rind on one raw edge, penetrating 1 – 2 mm into sample interior.	2.5	0.5/4
MU100089	A, B, C	Active meteoric fumarole	09/11/2016	Triangular hole, lots of steam, clearly burned red/orange discolouration, white mineralization as outer coating and large white minerals inside, cm-scale crystals inside. Steam escaping was ~85 °C.	5.3	Black-grey	WCM rind on one exposed side. WCM is well-distributed into large pore spaces, with a high concentration at one side of sample grading into none at the other side. WCM has small "finger-shaped" crystals that show consistent orientation throughout sample.	2.5	0.5/4.5
MU100620	A, B, C	Relict fumarole	12/11/2016	Relict fumarole in unaltered pahoehoe flow. Bright orange alteration on smooth surfaces, white subsurface precipitate mineral on sample. Cold temps equal to nearby surface rock. Patchy colours with red, orange, white, yellow concentrated along cracks in surface expression.	5.4	Black-grey	WCM has some green-brown tinge in some vesicles. Not rind-forming, but found filling or coating all vesicles >1 mm at one end of sample and tapering off ~2 cm from that edge to empty vesicles. Many vesicles are oblong and indicate a lava flow direction during cooling.	3	1/7.5

[1] Data were acquired by BASALT Research Project, funded by NASA PSTAR Program (NNH14ZDA001N-PSTAR) grant (14-PSTAR14_2-007) to D.Lim. Information was gathered from the BASALT Exploration Ground Data Systems (xGDS) server, which stores all information relayed from the field during deployments.

MU100110	A	Unaltered basalt	11/11/2016	None		5.5	Black	Uniformly black-grey with some 1-2 mm olivine phenocrysts. Few interior and exterior vesicles contain a thin partial coating of WCM. One exposed edge shows some grey colour, due to weathering.	2.5	2/3

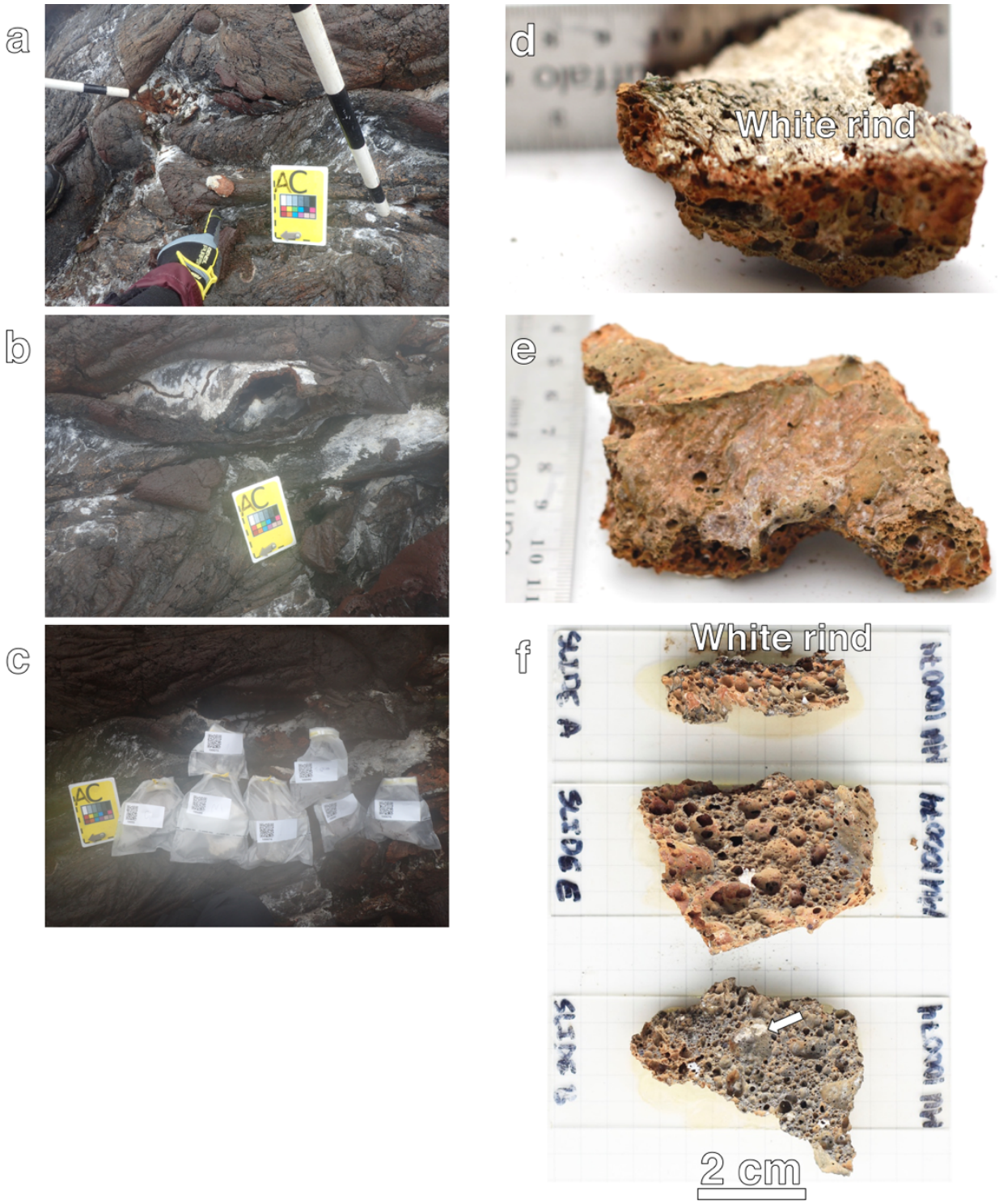

Figure 5.2 Images of sample MU100074. Images [a][1] and [b][1] are context photos taken by a member of the BASALT EV crew, showing the sampling site prior to sampling, while [c][1] shows all sample replicates in their labelled bags in the sampling site. Images [d] and [e] are photos taken of the whole sample before cutting. Image [f] shows (from left to right) slides A, E, and B. The white rind described in Table 5.1 is noted in [d] and [f]. Slide A was cut perpendicular to the white rind. Slide B was cut parallel to the white rind, such that the rind is the side adhered to the glass, and

slide E has the bottom of the sample [e] adhered to the glass. The arrow in [f] points to an example of WCM present in this sample's interior.

Figure 5.3 Images of sample MU100089. Image [a][1] shows all sample replicates in their labelled bags in the sampling site. [b][1] and [c][1] are context photos taken by a member of the BASALT EV crew, showing the sampling site prior to sampling. Image [d] shows (from left to right) slides A, B, and C. The arrows in [d] point to examples of WCM present in this sample's interior. Slides B and C were cut in a perpendicular direction to slide A. Their WCM crystals show a general growth trend parallel to the planes of the cut surfaces, while slide A's crystals have grown perpendicular to the plane of the cut surface.

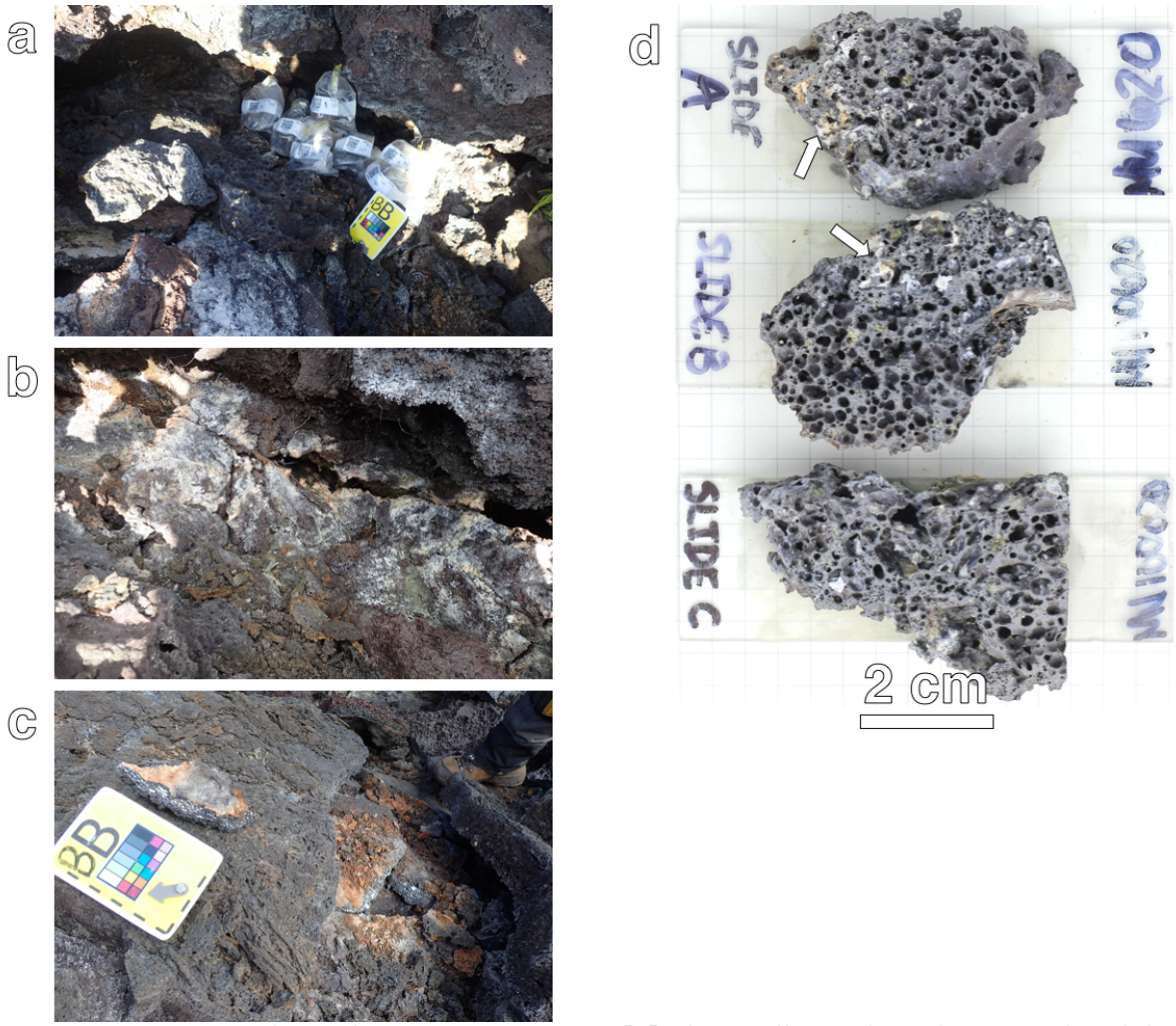

Figure 5.4 Images of sample MU100620. Image [a][1] shows all sample replicates in their labelled bags in the sampling site. [b][1] and [c][1] are context photos taken by a member of the BASALT EV crew, showing the sampling site prior to sampling. Image [d] shows (from left to right) slides A, B, and C. The arrows in [d] point to examples of WCM present in this sample's interior.

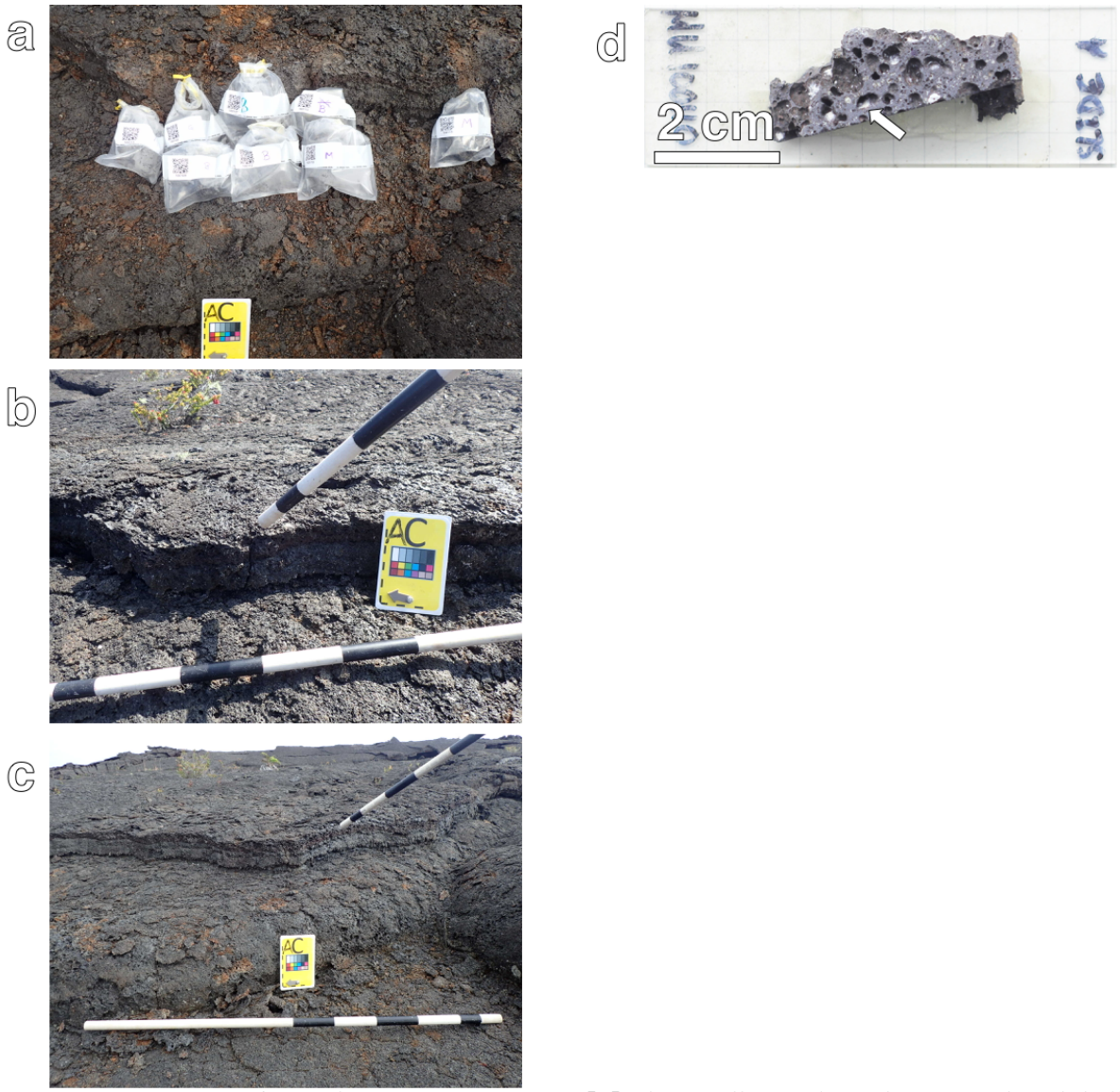

Figure 5.5 Images of sample MU100110. Image [a][1] shows all sample replicates in their labelled bags in the sampling site. [b][1] and [c][1] are context photos taken by a member of the BASALT EV crew, showing the sampling site prior to sampling. Image [d] shows (from left to right) slides A and B. Slide A was cut perpendicular to an exposed/weathered edge of the rock, while slide B was cut parallel to these edges. The arrow in [d] points to an example of WCM present in this sample's interior.

5.2 Idaho 2016

The BASALT deployment to Craters of the Moon National Monument (COTM) took place from 13 June to 1 July, 2016. Samples collected at all stations or sites-of-interest during simulated mission operations were returned to various BASALT-affiliated labs. However,

some returned samples were collected out-of-simulation, including two of the samples analyzed here. A map of all the sample locations is presented in Figure 5.6, below.

The basalts of COTM are compositionally different to those in Hawai'i. Chemically, they are more evolved, with a higher alkali metal content despite the more primitive silica composition (Hughes et al., 2018). This reflects their slightly more crustal derivation, as COTM's position with respect to the mantle plume had shifted with the movement of the North American plate while the lavas were still erupting. From Stout et al., (1994), the two lava flows investigated at COTM, Big Craters (BC) and Highway Flow (HF) differ slightly from each other. They share a common iron-rich composition, with high fayalite, iron-rich pyroxenes, and magnetites; along with dominant plagioclase in the groundmass. HF has been classified as a tristanite to trachyte, with higher silica content (~60 wt%), 60 – 90% fayalite (iron olivine end-member) in olivine microphenocrysts, and feldspar compositions of mostly sodium- to potassium- rich andesine, anorthoclase, oligoclase, and sanidine. BC is a trachybasalt, showing a slightly lower (~50 wt%) silica content, <60 % fayalite in olivine microphenocrysts, and sodium-rich andesine to anorthoclase feldspars.

As with the mission to Hawai'i, samples from COTM (the Idaho 2016 or ID2016 suite) were collected to represent a gradient of alteration conditions and types. Although there are no active fumaroles in COTM, two higher-alteration levels were defined: syn-emplacement alteration (high-temperature) and ambient (low) temperature alteration (Hughes et al., 2018). In syn-emplacement alteration, the alteration occurs near-instantaneously during eruption. Hot volcanic gases cause oxidation of iron species within the lava, causing a change in colour to the glass from dark grey-black to purple, red, and orange.

Lower-temperature alteration is the result of much longer-term processes such as chemical weathering due to meteoric or ground water influences under ambient climate conditions (Hughes et al., 2018). Water can act as a transport medium for the chemical constituents of secondary minerals, such as calcite, sulfates, smectites, and zeolites, as well as causing the breakdown of basaltic minerals. Olivine is the mineral least resistant to weathering and will readily decompose to iddingsite, a combination of goethite and smectite; iddingsite has been detected in Martian meteorites (Kuebler et al., 2003).

The samples in the ID2016 suite are described below, in Table 5.2, and pictured in Figures 5.70 - 5.11. These samples include two higher-temperature or syn-emplacement altered rocks, one lower-temperature altered rock, and two unaltered basalts.

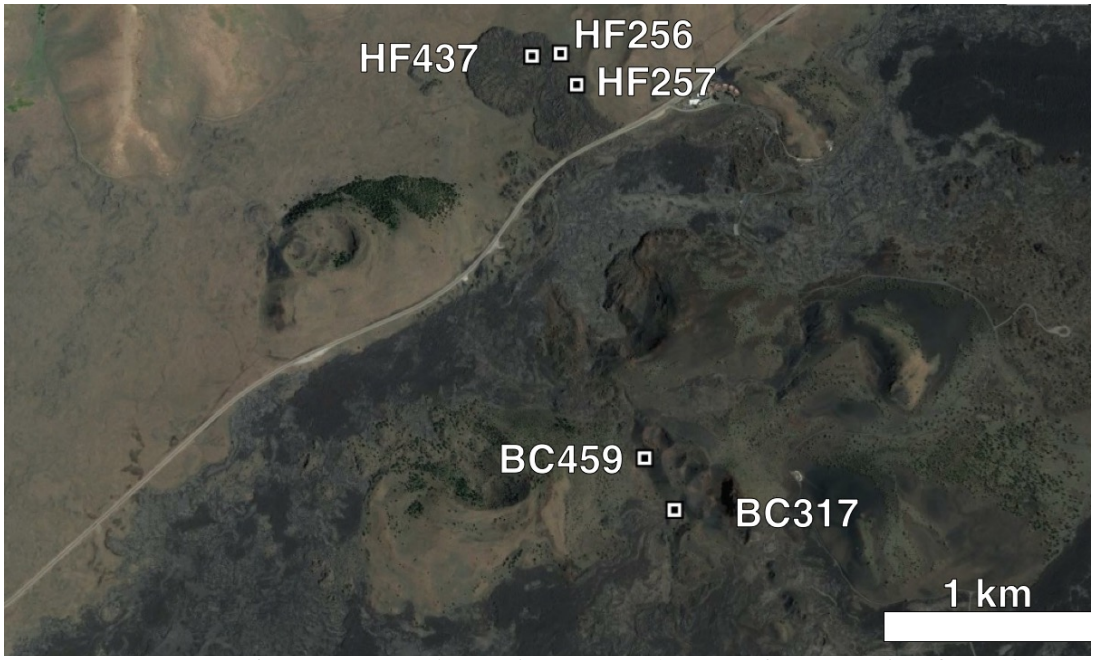

Figure 5.6 Locations of ID2016 samples within COTM (images from Landsat/Google Earth).

Table 5.2 Physical characteristics of analyzed samples from the Idaho 2016 (ID2016) sample suite. In the sample numbers, "HF" refers to samples collected from Highway Flow, while "BC" refers to samples collected from the Big Craters lava flow.

Sample	Slides analyzed	Sample type[1]	Date collected[1]	Notes from the field[1]	Figure	Colour	Alteration characteristics	Approx. median vesicle diameter (mm)	Approx. vesicle size range (min/max) (mm)
HF437	A, B, C, D	High-T alteration	25/06/2016	Very bright orange and red alteration and rough surface texture. Appears to have both high-T oxidation as well as subsequent meteoric ambient alteration.	5.7	Brown, black, red, orange	Streak of red-yellow-orange matrix through centre of slide A; otherwise, matrix is fairly uniform brownish-black.	1	0.5/3
BC459	A, C, D	Mod- to high-T alteration	28/06/2016	Out-of-simulation collection of highly-altered material near gas crack.	5.8	Tan, yellow, brown, red, black	Interior ranges from tan to bright yellow and dark maroon-red; black matrix only on some fresh cut surfaces	2	1/7
HF257	A, B, C, D	Low-T alteration	23/06/2016	~2.5 m high convoluted aggregate of lava; shows significant flow contortion and mixing of solid and semi-solid lava during emplacement. Possible zones of high and low-density material with expected frothy zones.	5.9	Brown, black	Slight colour change from black to brown through sample	1	0.5/5
HF256	A, B, C, D	Unaltered	24/06/2016	Outcrop of smooth, partly unaltered rock with blocks of smooth and rough surface textures underneath. White, buff, and light orange alteration. Thick tan alteration filling cracks in outcrop. Degassed, very few to no vesicles.	5.10	Black	None visible	0.5	0/1

BC317	A,B,C	Unaltered	22/06/2016	Very glassy – low permeability precludes fluid penetration. Dark colouration, some maroon tone. Very fine-grained, ~20% vesicularity, elongate smooth vesicle shape. Very dense between vesicles. Minor alteration of surface and in vesicles. No phenocrysts. Out-of-simulation collection.	5.11	Black, dark brown	Very small amounts of WCM in few vesicles	3	1/5

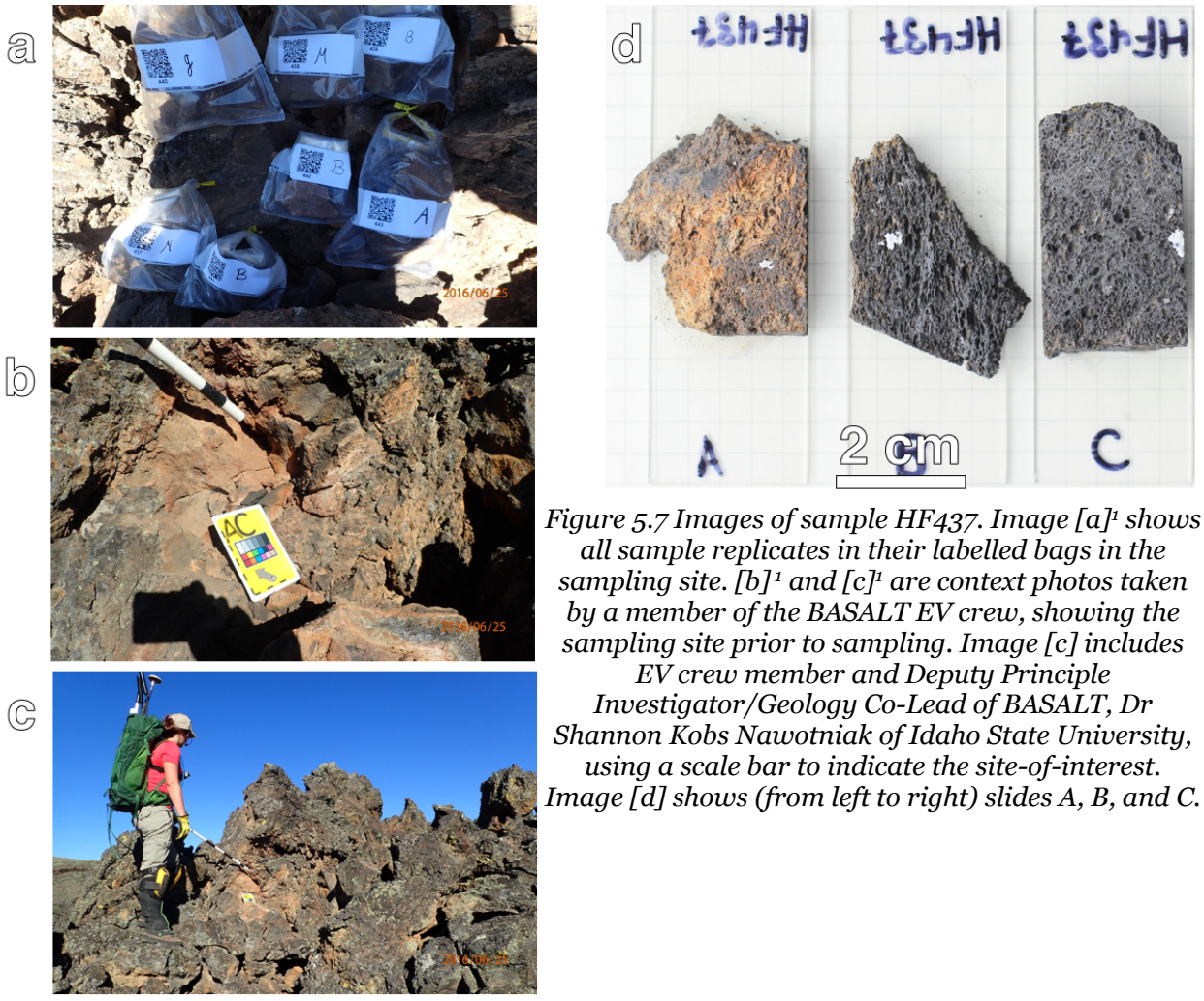

Figure 5.7 Images of sample HF437. Image [a][1] shows all sample replicates in their labelled bags in the sampling site. [b][1] and [c][1] are context photos taken by a member of the BASALT EV crew, showing the sampling site prior to sampling. Image [c] includes EV crew member and Deputy Principle Investigator/Geology Co-Lead of BASALT, Dr Shannon Kobs Nawotniak of Idaho State University, using a scale bar to indicate the site-of-interest. Image [d] shows (from left to right) slides A, B, and C.

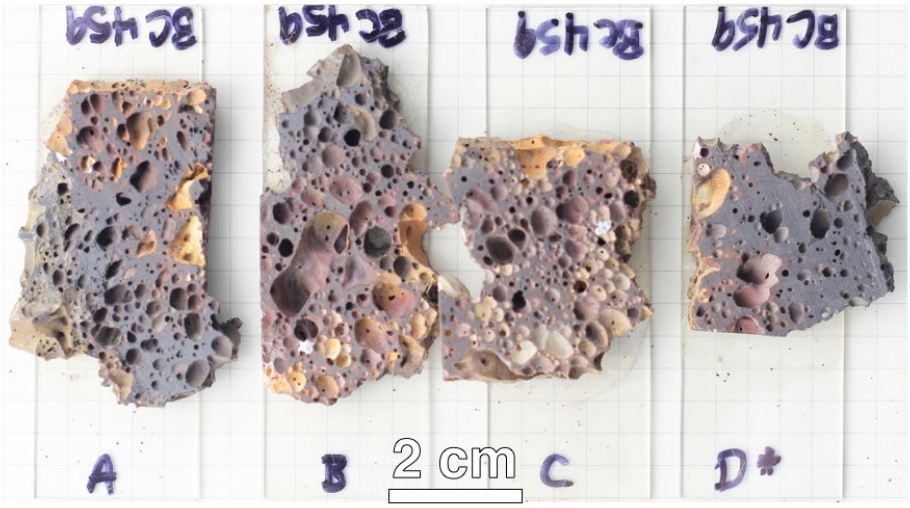

Figure 5.8 Slides A, B, C, and D of sample BC459. The darker colour of the cut surfaces may be due to thermal alteration from the cutting process, despite attempts to mitigate this during sample preparation.

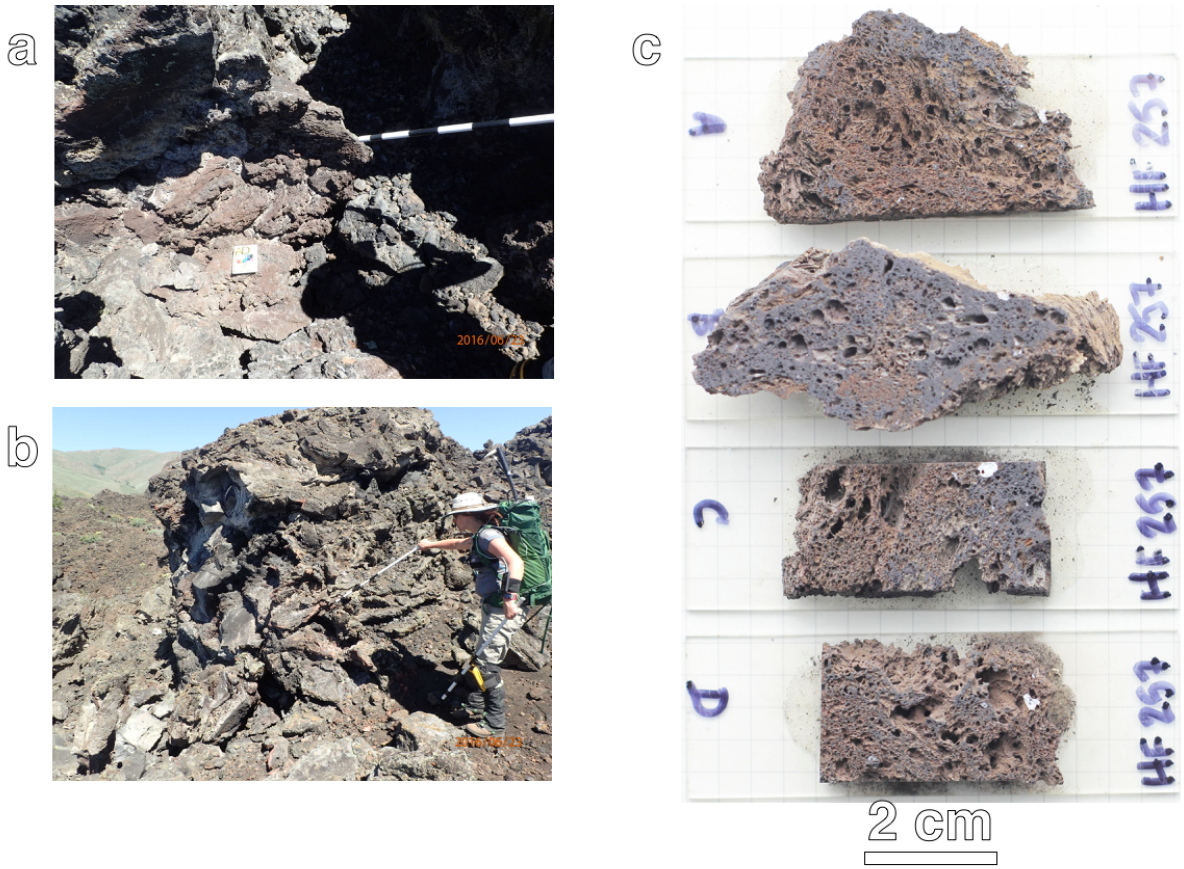

Figure 5.9 Images of sample HF257. Images [a][1] and [b][1] show the sampling site in context, with Dr Kobs Nawotniak pointing to the site-of-interest in [b]. Image [c] is of the sample slides A, B, C, and D.

Figure 5.10 Images of sample HF256. Image [a][1] shows all sample replicates in their labelled bags in the sampling site. [b][1] and [c][1] are context photos taken by a member of the BASALT EV crew,

showing the sampling site prior to sampling. [d] and [e] show the whole sample before cutting. [f] shows (from left to right) slides A, B, C, and D.

Figure 5.11 Images of sample BC317. Images [a] and [b] show the whole sample before cutting. [c] shows (from left to right) slides C, B, and A.

6 Instrumentation and Experimental Design

The procedures developed during this study were designed to satisfy two goals: to identify any organic material present within the selected BASALT samples, and to characterize the distribution of the organic material within the samples with respect to their physical properties. Accordingly, a number of experiments and analyses were undertaken, including work with spectroscopy and microscopy. The experimental design is summarized in figure 6.1, below.

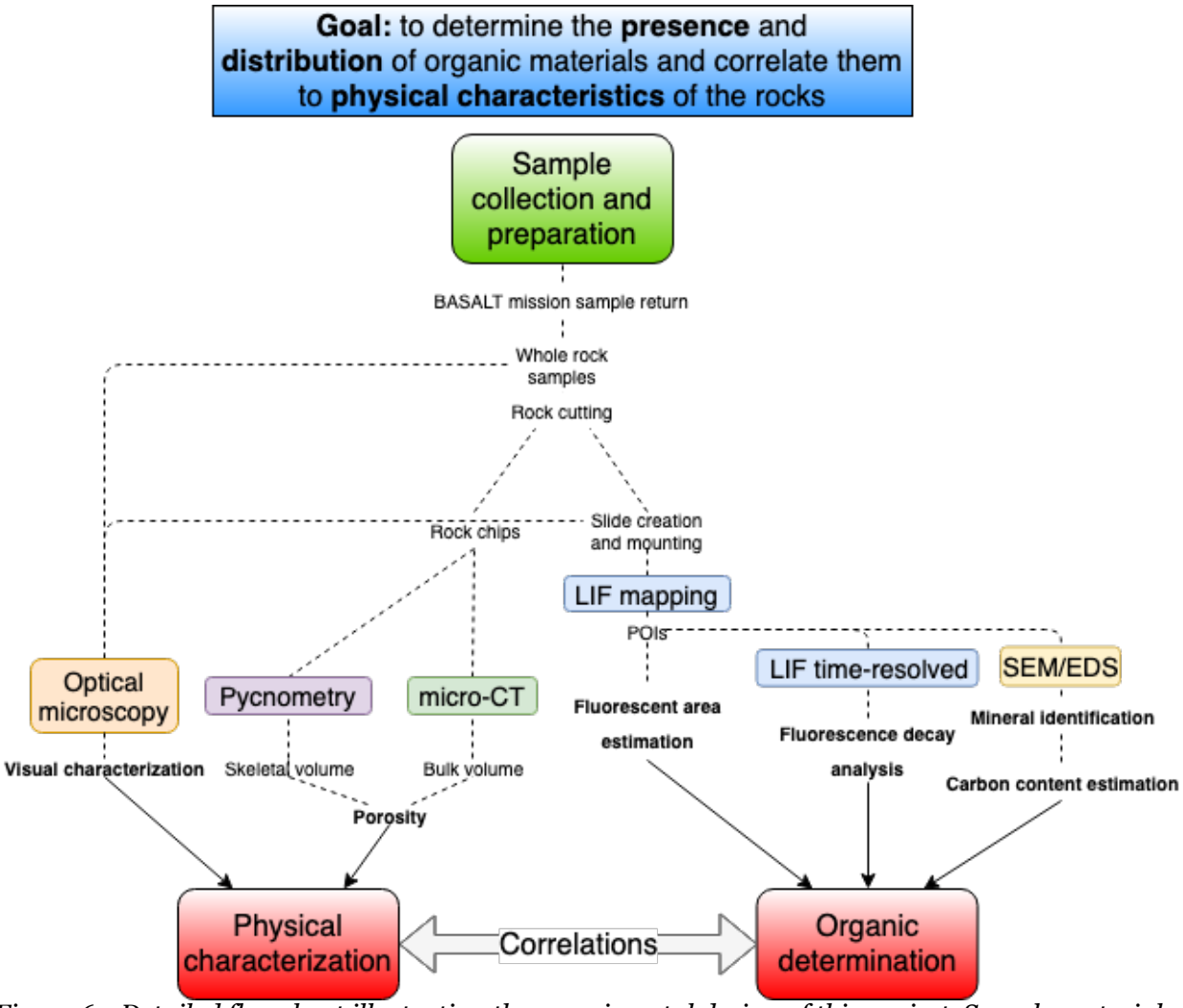

Figure 6.1 Detailed flowchart illustrating the experimental design of this project. Sample materials produced from the "sample collection and preparation" stage (in top green box) are analyzed with various instrumental techniques (multi-coloured boxes), to create results (bolded text). These feed into the high-level project outputs (red boxes). Initialisms used: POI (point[s]-of-interest); micro-CT (micro-computerized tomography); SEM/EDS (scanning electron microscopy/electron-dispersive x-ray spectroscopy).

6.1 Sample Preparation

6.1.1 Collection and processing

During the 2016 BASALT deployments to COTM and Mauna Ulu, after the sample-selection phase of the mission days were complete, the sampling site (approximately 1 m^2 of an outcrop) was evaluated by the EV crew to determine how to best break it up and distribute its pieces. All chunks of rock were broken off with an alcohol- and flame-sterilized rock hammer, and handled while wearing two sets of surgical sterile gloves. The target size for samples to be returned to McMaster University was "grapefruit-sized". During the rock-breaking process, if a chunk was produced that matched that size, it was quickly bagged in a labelled, sterile Whirl-Pak bag.

McMaster received two sample replicates from each site. Other samples of various sizes were similarly collected in Whirl-Paks. All samples were returned each day from the field to Mission Control, and those samples designated for the biology (University of Edinburgh) and organic geochemistry (McMaster and York) teams were immediately placed in a deep freezer, to be left for the mission duration. Upon the conclusion of the missions, our samples were shipped to McMaster in a cooler filled with ice packs. The samples ultimately designated for analysis at York were freeze-dried in 2017 in the Environmental Organic Geochemistry Lab at McMaster University so they could thenceforth be handled at room temperature while maintaining preservation of any organic materials in their original states.

6.1.2 Rock cutting

At York University, each sample was cut into slides approximately 1 cm thick with two parallel, flat surfaces for ease of analysis. A Metkon Geocut rock saw with a diamond blade was used to cut the samples (figure 6.2 [b]). The saw blade was stripped of paint before initial use, and the blade along with any clamps for securing the rock were thoroughly wiped down with methanol or ethanol. Cuts were made slowly, without the use of cooling water to prevent contamination.

The goal with cutting was to produce 2-4 good-quality slices of different orientations per sample (figure 6.2 [a]). This would expose the sample's varying interior environments, revealing the extents of heterogeneity and alteration. For example, if a sample had a visible coating of some alteration material on one side, at least one slice was

cut perpendicular to that side such that the slice could show the depth of penetration of that coating into the sample interior, while another slice was cut parallel to that side.

If the slices were still too big to be useful as slides, a smaller Buehler IsoMet low speed rock saw was used to refine the sizes (figure 6.2 [c]). Additionally, rock chips small enough to fit the 10 cm^3 pycnometer cup were produced with this saw. The saw was similarly sterilized and operated without coolant.

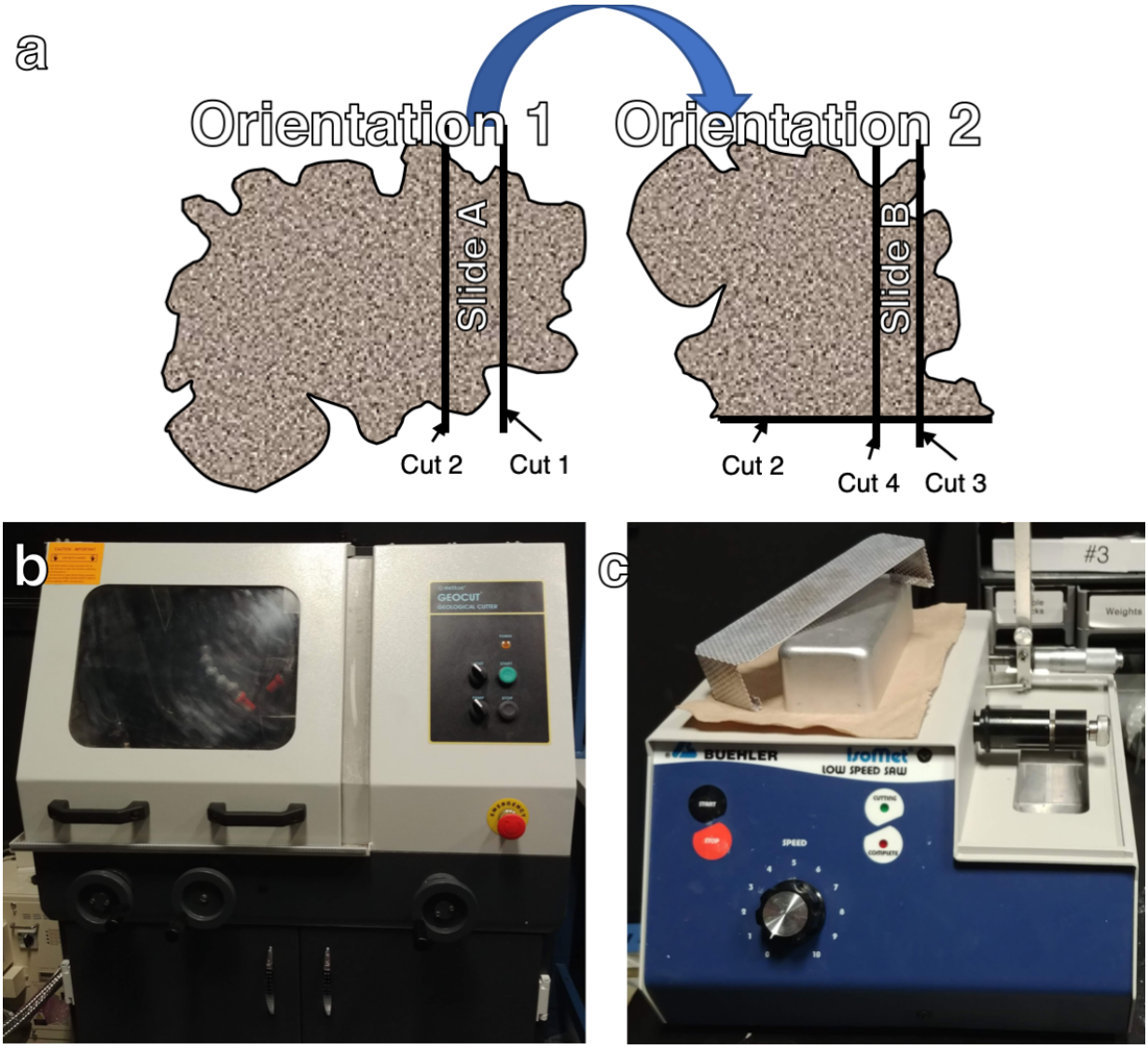

Figure 6.2 [a] Illustration of cutting process: a sample in an initial orientation (Orientation 1) is cut twice to produce Slide A. It is then re-oriented 90° (Orientation 2) and cuts 3 and 4 are applied to create Slide B. [b] Metkon Geocut rock saw, used for initial cuts of samples into slides. [c] Buehler IsoMet low speed saw, for refined cuts of smaller sample pieces.

6.1.3 Slides

Each slice chosen for analysis was adhered to a standard glass slide with Loctite® brand 0151 Hysol Epoxi-Patch adhesive, and left to cure for at least 24 hours. Slides were labelled with the sample bag number – the original Whirl-Pak bag label – and an individual letter, e.g. MU100620 Slide A.

6.2 Visual Characterization

Samples were characterized visually through simple hand-sample examination by eye, and with the aid of a Nikon® SMZ 745T microscope (Figure 6.3). Microscope images were recorded with the attached Infinity 1 camera using the included InfinityAnalyze software. The images, each representing a field-of-view of approximately 6 – 10 mm, were stitched together in Adobe® Photoshop® photo-processing software to create a composite image of the slide surface, including the mapping area. The samples' colours, approximate vesicle size and distribution, and any visible alteration patterns such as in-filled vesicles or discolouration were tabulated in a spreadsheet (see tables 5.1 and 5.2).

Figure 6.3 Nikon® SMZ 745T stereo microscope with Infinity 1 camera, in the Planetary Instrumentation Lab, York University.

6.3 Laser-Induced Fluorescence Spectroscopy

At York University, we have developed an experimental instrument capable of Raman and laser-induced fluorescence (LIF) spectroscopy (Figure 6.4). Designed by Eshelman (2016), with further modifications during this study, the instrument utilizes a TEEM Photonics™ 266 nm Nd:YAG PowerChip™ laser pulsed at 1 kHz for maximum power output at source (approximately 15 mW). The laser line is reflected and collimated through a path of 13 mirrors and 2 lenses (f = 50 mm and f = 250 mm), for a total path length from source to

sample of approximately 10 m. At the collection optics set-up, the laser is reflected off a 266 nm edge filter, through a 15x UV microscope objective (Thorlabs LMM-15x-P01), to the stage with the secured sample. Emitted light from the sample travels up through the objective, through the edge filter, and is focused by a lens (f = 100 mm) to a 3 m fibre-optic cable.

Over its length, the fibre cable collimates the light from a circular input to a vertically-aligned 70 μm slit output. The light is directed into the Andor Shamorck™ 163 spectrograph, which contains a grating with 300 lines/mm and a 300 line blaze for fluorescence detection. This wavelength-separated light is directed to the Andor iStar™ DH334t iCCD camera. It travels through an 18 mm diameter photocathode, converting the light to photoelectrons. Photoelectrons are then amplified and intensified by an intensifier tube and microchannel plate, before being converted back to photons by a phosphore. The supplied iStar software, Andor Solis™, can change the gain, or the voltage across the microchannel plate; with increased voltage, the signal is intensified more and the signal reaching the sensor is amplified. The photons are detected by a 1024 * 1024 pixel charge-coupled device (CCD) with 13 μm pixels. The spectral resolution with this grating and slit size is approximately 8 nm (Lymer, 2017).

A digital gate system is applied by Solis, whereby the photocathode is only switched on when the gate is opened. For TRF function, the software is capable of generating a digital gate delay of 0 to 10 s with a resolution of 10 ps, and a digital gate width of 1.5 ns.

The laser triggers the camera to activate the CCD with each pulse through a Bayonet Neill-Concelman (BNC) cable connection. The lengths of the BNC connector and laser path are optimized such that the camera should receive and act on this trigger signal at the same time as the light arrives at the detector. In reality, there is an approximately 2 ns delay between the camera activating and the arrival of the light, as revealed in TRF data, but this is easily corrected.

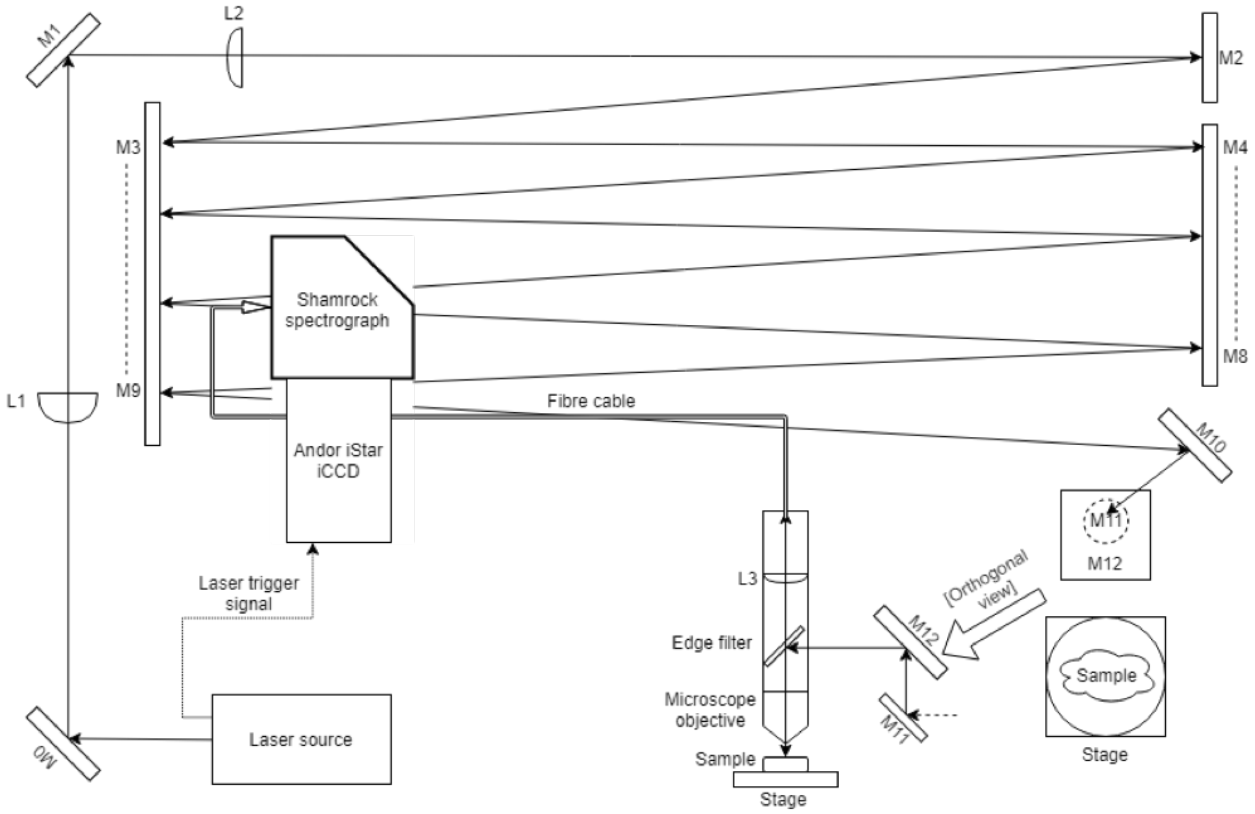

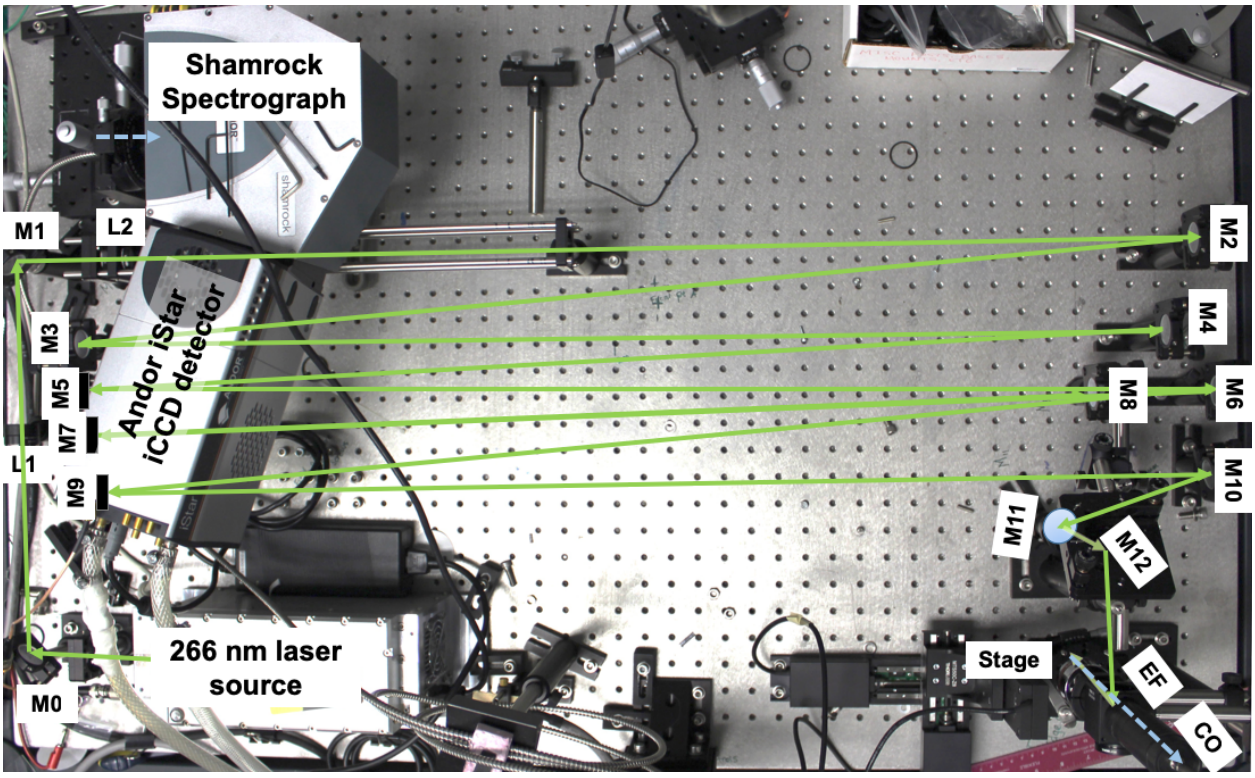

Figure 6.4 Block diagram (top) and labelled photograph (bottom) of the York University Raman/LIF instrument. The laser travels from the source to mirror M0, through L1 to M1, through L2 to M2, then from M3 to M12 where it bounces across to the edge filter and down to the sample

on the stage. From the sample, any light emitted (along with some residual 266 nm light) travels up through the microscope objective, the edge filter to remove excess 266 nm light, and is focused on the fibre cable through L3 within the collection optics tube. The fibre cable takes it to the Shamrock spectrograph to be split into its component wavelengths and the light spectrum is detected and digitized by the iCCD detector.

6.3.1 LIF Mapping

Our LIF instrument is equipped with a tri-axis motorized stage (ThorLabs MTS25/M-Z8), with an attached manual rotating stage mount, enabling easy focusing and positioning of the sample beneath the microscope objective.

Based on the method outlined in Lymer (2017), using a National Instruments LabView application developed by Eshalman (2016), it is possible to create raster maps of a sample surface by combining stage movement with spectral measurements. With a chosen map site, the laser spot would be positioned in the upper right-hand corner. The application would take and record a spectral measurement, then move the stage along one axis by a specified amount, take and record a spectral measurement, and repeat. The application was capable of moving the stage in the X and Y planes by a specified distance and number of steps, to create anything from a two-dimensional line scan to a rectangle or square. Each stop and measurement during the map collection would then be post-processed to create a map, where one pixel represents one measurement.

For this study, a 1 cm * 1 cm area was chosen on each slide as the measurement site. The map site was chosen to represent the heterogeneity of that particular slide, and contribute to the interpretation of the sample as a whole. To that end, the following criteria were set out for map site selection:

- At least one map per sample was taken along an exposed or weathered edge;
- At least one map was taken in the interior of a slide;
- Depending on the sample's heterogeneity or areas of visible alteration, a map would try to include boundaries or transitions between different materials in the rock.

An index card with a 1 cm * 1 cm square window cut out was used to examine the slide and determine the best map site. Once chosen, a dab of Staples® brand Simply™ correction fluid was applied to the upper right corner of the map, to act as a starting point

reference[2]. The slide was secured to the rotating stage with stage clamps, and the angle of rotation was recorded.

Before proceeding with mapping, a few test time-resolved spectra were taken from a suspected point-of-interest (POI) within the map, such as a vesicle filled with white crystalline material, and the sample matrix. These were used to determine the appropriate gate delay for the whole map, to optimize the fluorescent signal intensity. The stage position was then moved to place the correction fluid marker directly beneath the laser, and raised or lowered slightly from the laser focal point to reduce burning of the sample surface.

The following parameters were set in the LabView application for all sample maps:

- Gain: 2500
- Digital gate delay: 4 – 7 ns, depending on initial measurement
- Digital gate width: 10 ns
- Exposure time: 0.05 s
- Number of accumulations: 80
- Stage step size: 0.25 mm
- Number of steps: 40 * 40

Therefore: each map measurement would take 4 s; with each map consisting of 1600 steps, the mapping time was approximately 2 hours.

6.3.2 Map data processing

Data were recorded at each point as a sequentially-numbered .txt file with two columns: wavelength (nm) and fluorescence intensity (arbitrary units). A MatLab code was developed to import all the data files into a single 1024 * 1601 matrix, with each row representing a single wavelength recorded by the detector, the first column showing the wavelength labels in nm, and the remaining 1600 columns are the intensity at each point.

[2] This correction fluid was chosen because it acted as a marker visible both to the naked eye and in the fluorescence map for the upper right corner of the map. With this and the recorded stage angle, the positions of POIs could be accurately re-found for subsequent measurements, and a map image could be precisely overlain on a microscopic photograph of the sample (see Results). The correction fluid fluoresced in both the examined wavelength range, and with a similar intensity to the highest intensities of POIs in the map, making it a highly appropriate marker. Conveniently, the laser's initial position and part of its path were also burned into this marker, making matching the map to the photograph simple.

A second MatLab script produced a figure displaying all spectra on a single graph, showing common peaks shared by multiple points. A separate script, developed by my research assistant Keagan Lee in the summer of 2018, allows one to select and remove any outstanding (extremely high intensity) spectra from this figure. This allows the figures to be scaled to the less-intense spectra for examination of finer details, if necessary.

A MatLab script lets one choose a range of wavelengths (e.g. the minimum and maximum wavelengths of a broad, shared peak) to display in raster form. This script would re-organize the spectral data into a 40 * 40 matrix, with each entry showing the normalized fluorescence intensity of that point measurement within the chosen wavelength range. The matrix would then be converted to a raster image. Using a MatLab-standard colour scheme ("Jet") scaled relative to the intensities of the individual sample, the image would depict a heat map of fluorescence intensity at each measurement point (one pixel per point). This raster map would be overlain on a composite microscopic image of the sample surface, using the correction fluid marker and stage rotation angle as a guide. Pixels or clusters of pixels showing high intensity fluorescence relative to background were chosen as POIs for further investigation, and matched to features visible in the microscope image.

Finally, an absolute scale was developed to measure fluorescence intensity across all maps. The initial relative-scale maps were all created using the "Jet" colour scheme available through MatLab, which ranges from dark blue for low values through green, yellow, orange, and to dark red for high values. Visual estimates of the intensity values at the mid-green and bright red levels were taken from all the maps and averaged to create a low cut-off point ($1.057 * 10^9$) and a high cut-off point ($1.823 * 10^9$). These values were input as thresholds in a new three-colour scale, where blue represents all intensities at or below $1.057 * 10^9$ ("low intensity"), yellow represents all intensities between $1.057 * 10^9$ and $1.823 * 10^9$ ("high intensity"), and red represents intensity values greater than $1.823 * 10^9$ ("very high intensity"). With this three-colour scale applied to each map, the number of pixels of each colour can be quantified and used to estimate the area of fluorescent material. Thus, the intensity and area of fluorescent material can be compared between samples.

6.3.3 LIF time-resolved results

Time-resolved fluorescence measurements made use of Andor Solis' "Kinetic" acquisition mode, which allows one to take "snapshots" of LIF response as it grows and decays with increasing gate delay. TRF measurements were taken from the POIs determined in the previous step. Sometimes, multiple measurements were taken from around a single POI in order to find the best response, with adjustments to the laser spot focus made as necessary.

The following parameters were used for all TRF measurements:

- Gain: 2500
- Digital gate delay: 0 ns + 0.5 ns/step
- Digital gate width: 3 ns
- Exposure time: 0.05 s
- Number of accumulations: 200
- Number of measurements: 20

Hence, these data were recorded with three dimensions: wavelength (nm), time (0 – 9.5 ns), and intensity (arbitrary units).

6.3.4 TRF data processing

Data from Andor Solis are imported into a single matrix of size 1024 * 21 in MatLab, where each row is one wavelength, the first column is the wavelength labels, and each subsequent column is intensity per wavelength per time step. A MatLab script generates a contour image, with the x-axis showing wavelength (nm), y-axis showing time (ns), and an absolute colour scale (using the MatLab "Jet" colour scheme) displaying intensity (arbitrary units). The absolute colour scale allows for quick comparisons of fluorescence intensity between multiple measurements. The spectrum collected that shows maximum intensity from this series is overlain in white, in order to demonstrate the peak positions.

6.4 Scanning Electron Microscopy

To augment the fluorescence investigations of the samples, I chose to use scanning electron microscopy (SEM) with electron-dispersive x-ray spectroscopy (EDS). This method allows for high-resolution micro-scale images of POIs, and elemental analyses of

the materials present. Elemental analyses were especially useful in confirming the presence of organic carbon at the POIs and identifying the surrounding minerals.

At York, we have a Tescan VEGA3 SEM, which was operated under low-vacuum conditions (50 Pa) and medium- to high-voltage (10 – 20 kV) for imaging and analyses (Figure 6.5). Samples were uncoated to prevent contamination. Images of POIs at approximately 400 – 700 x magnification were taken, along with their surroundings. Additional images of the rock matrices outside of the mapping areas were taken for comparison.

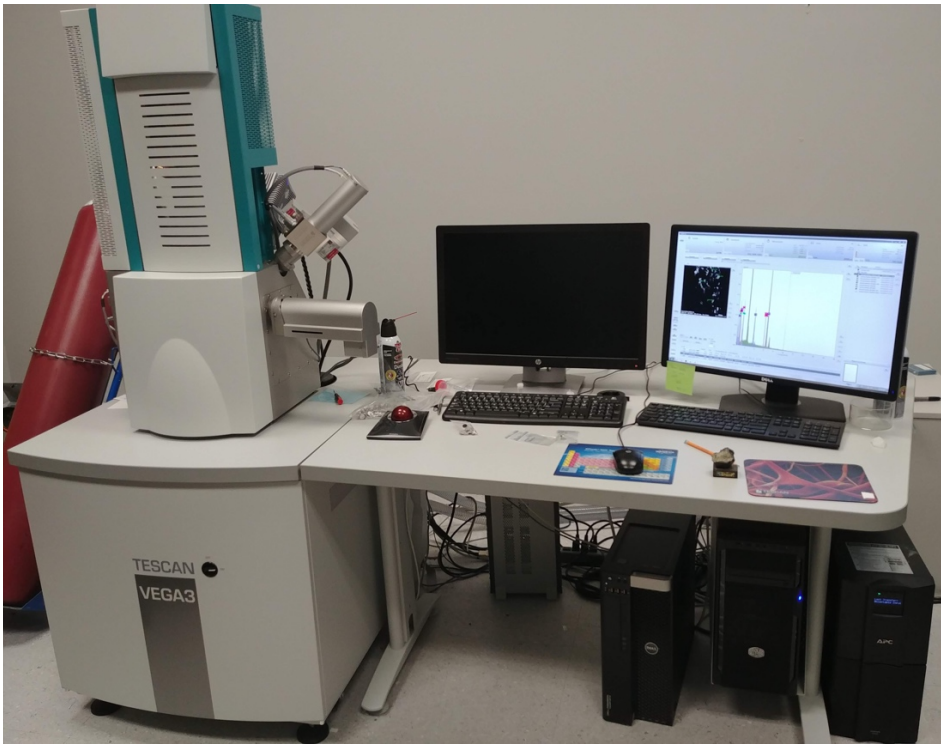

Figure 6.5 TESCAN VEGA3 Scanning Electron Microscope in the Planetary Instrumentation Lab, York University.

The SEM is equipped with a Bruker QUANTAX EDS, capable of taking quantitative measurements of elemental composition. After each SEM image was acquired, the EDS detector was inserted into the chamber and the image re-taken with the EDS. Ten to fifteen analysis points were chosen within the image: at least two points per feature, such as a crystal or globule, to confirm consistent composition.

6.4.1 EDS Data Processing

Each point in the EDS image was automatically quantified within the ESPRIT software twice: one quantification normalized to include only major rock-forming (O, Si, Ti, Al, Fe,

Mn, Mg, Ca, Na, K, P, Cr) and biologically-relevant elements (C, N, S), and one including trace elements such as rare earth elements (REEs) and platinum-group elements (PGEs).

The weight percent value of each element was re-calculated to the appropriate weight percent oxide and normalized to the sum of all weight percent oxides in each point (method from Jackson et al., 1967). The values from the major/bio elemental quantification were compared with expected weight percent oxide values for common igneous and alteration minerals derived from literature data (*e.g.* Deer et al., 1992; Van Olphen & Fripiat, 1979). Although this method is not as accurate as others such as x-ray diffraction for identifying minerals, for the purposes of this research it provides an appropriate estimate of the mineral composition of these POIs, as well as the carbon content.

6.5 Porosity

The porosity of a vesicular sample is the relationship of pore or void spaces to solid volume, expressed as a fraction or percentage. While it cannot directly communicate the relative sizes of vesicles, it can indicate the availability of interior space in a given rock for the deposition of secondary hydrothermal minerals or colonization of microbes. A helium-gas pycnometer was used to measure the skeletal volume of the samples, and a micro-computerized tomography (μCT) scanner was used to measure the bulk volume.

6.5.1 Helium gas pycnometer – skeletal volume

Small rock chips were cut from each sample, with estimated total bulk volumes of 2 – 5 cm^3. These chips were placed in a desiccator and subjected to a low vacuum for at least 24 hours before proceeding with measurements, to remove as much interior water as possible. A Micromeritics AccuPyc II 1340 He-gas pycnometer (Figure 6.6) with a test cup volume of 10 cm^3 was used as directed, with each sample chip being measured 10 times. These data were recorded in an Excel spreadsheet, and the mean average skeletal volume was calculated for each sample ($\boldsymbol{V_{skel.rock}}$).

Figure 6.6 Micromeritics AccuPyc II 1340 pycnometer in the Planetary Instrumentation Lab, York University.

6.5.2 Micro-computerized tomography – bulk volume

The mechanical engineering department of York University's Lassonde School of Engineering has a Bruker SKYSCAN-1272 μCT available for detailed measurements of small samples (Figure 6.7).

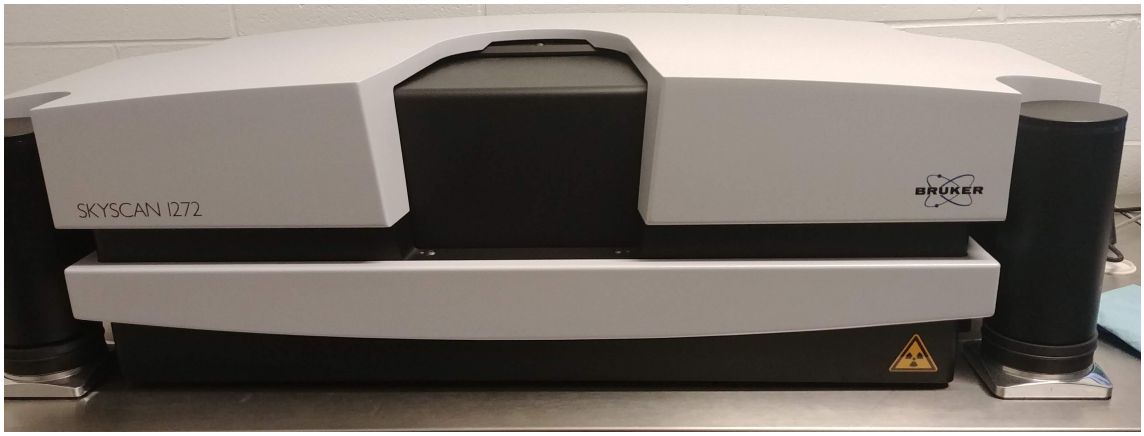

Figure 6.7 Bruker SKYSCAN-1272 μCT scanner in the mechanical engineering department, York University.

Each sample chip was scanned with a source voltage of 90 kV and source current of 111 μA, a pixel size of 21.6 μm, and a rotation step size of 0.3°. The cross-sectional images were compiled in Bruker's CTAn software to create a 3D model. The following post-processing steps were applied in the software to obtain the final bulk volume values:

1. Thresholding: Using an averaged histogram for all cross-sectional μCT scan images, the images were converted to binary (black and white) with white being constrained to rock material and black representing all void and outside space.
2. Despeckling: All isolated white points of 10 pixels or less were removed from each image, to clean up any artefacts.
3. Smoothing: The "closing" function is used to connect objects that are close in proximity but initially distinct, using a round kernel with a radius of 25 pixels, within each image.
4. Pore in-fill: All void spaces contained entirely within the white rock are filled, creating a solid shape.
5. 3D analysis: Various 3D parameters of the solid were measured, including the bulk volume ($\boldsymbol{V_{bulkrock}}$).

Examples of these process steps are illustrated in Figure 6.8, below.

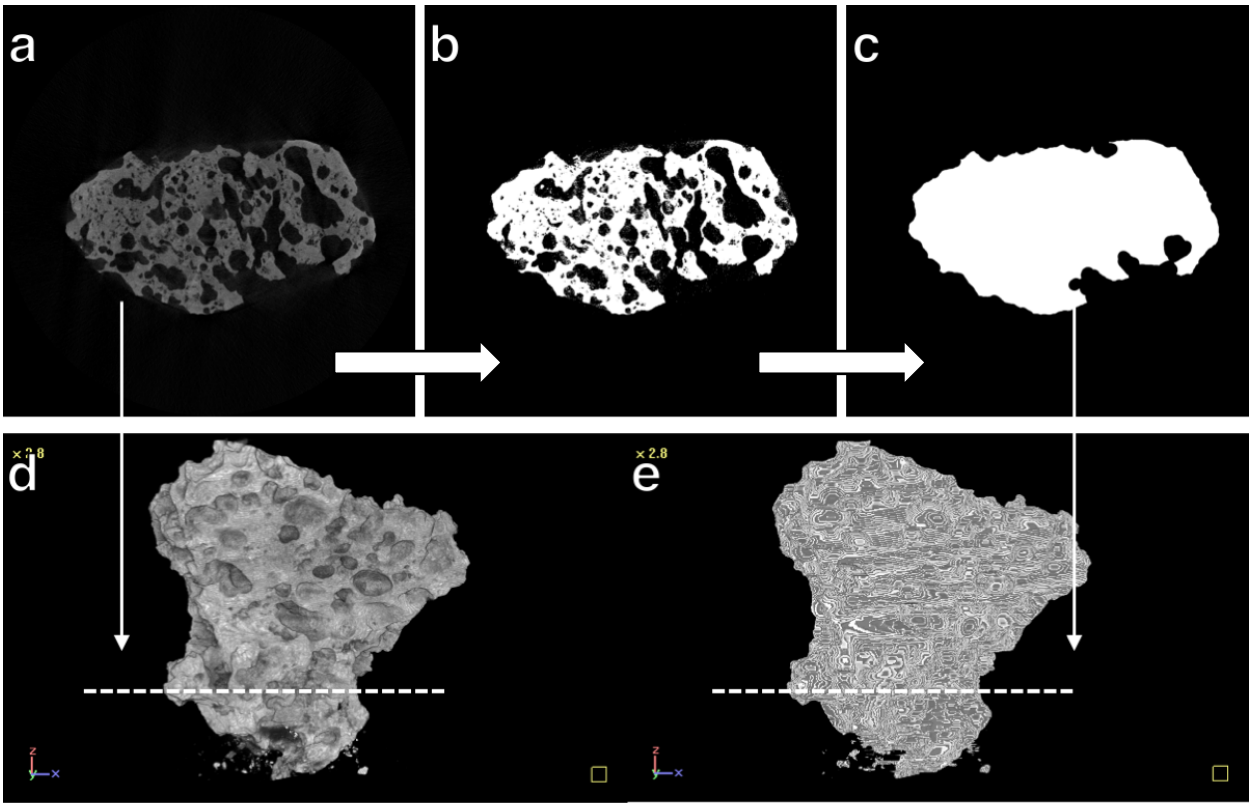

Figure 6.8 [a] Original μCT cross-sectional image of a sample chip. Some interior structures are visible as brighter or darker parts based on their density. The arrow indicates the slice's position in the 3D model [d]. [b] Binary thresholded image based on [a]. [c] The binary image has undergone despeckling, smoothing, and pore in-fill. The arrow indicates the slice's position in the 3D model [e]. [d] Original μCT-generated 3D shape model of a sample chip. [e] 3D shape model of the same rock chip, post-processing.

With $\boldsymbol{V_{bulkrock}}$ and $\boldsymbol{V_{skel.rock}}$ thus obtained, the porosity of the samples were calculated using the equation:

$$\boldsymbol{\varphi_{rock} = (V_{bulkrock} - V_{skel.rock}) / V_{bulkrock}}$$

7 Results

The following chapter is organized on a sample-by-sample basis, with samples grouped together based on their location of origin (Idaho or Hawai'i). For each sample, the results from LIF and SEM-EDS experiments are presented, followed by the porosity measurements from the pycnometer and micro-CT scanner. A table summarizing all of the major findings is included at the end.

Some sources of error unique to these measurements include: the EDS measurements not being ideal, due to sample surface texture and angle of POI with respect to the detector, as well as the resolution of the image; the number of EDS points taken per POI not being consistent across all samples; the locations of EDS points compared to the locations of the fluorescence measurements not being exact; and the sizes of the POIs being inconsistent across samples.

The unevenness of the sample surfaces made LIF and SEM measurements inaccurate to an unknown and irregular degree. As a measurement point such as a laser spot (LIF) or electron beam (SEM) moves over the vesicular surface of a sample, it will be unfocused when it dips into a vesicle, producing a somewhat unreliable result.

7.1 HI2016 – MU 100074 (Active Fumarole)

7.1.1 LIF mapping and LIF time-resolved results

Sample MU100074 was cut into three slides, with three 1 cm * 1 cm maps produced through LIF mapping. The LIF results from these slides are presented in figures 7.1, 7.2, and 7.3. In each figure, image [a] is a photograph of the slide being presented. Image [b] is the absolute intensity scale (see 6.3.2) used to compare maps within and between samples. Image [c] is a composite microscopic photograph (see 6.2) of the mapped area of the slide, with any POIs identified and labelled. Image [d] is the same composite photograph, overlain with the relative-scale LIF map displayed with the MatLab "Jet" colour scheme (see 6.3.2), with the POIs identified and labelled. Images [e] and [f] in figures 7.1 and 7.2 show the absolute-intensity-scaled time-resolved contour plots (see 6.3.4) of the POIs present in those maps. This order of images is similar for all other samples.

Maps A (fig. 7.1) and B (fig. 7.2) were both taken near the exposed edges of the sample, with white crystalline material visible within the map area (fig. 7.1 [a] and 7.2 [a]). Each map showed two highly-fluorescent POIs associated with vesicles filled with WCM (fig. 7.1 [c-d] and fig. 7.2 [c-d]). Their time-resolved spectra had a prominent peak in the 425 – 450 nm range that reached its maximum intensity at 4.5 ns and showed a rapid decay time of approximately 2.5 ns (fig. 7.1 [e-f] and fig. 7.2 [e-f]).

The map A absolute intensity scale map (fig. 7.1 [b]) showed a total of 7 red pixels and 7 yellow pixels (excluding those from the correction fluid mark), with a combined approximate area of 3.5 mm², based on the map step size of 0.25 mm. The Map B absolute intensity scale map (fig. 7.2 [b]) showed 1 red pixel and 3 yellow pixels, with a combined approximate area of 1.6 mm², based on the map step size of 0.4 mm.

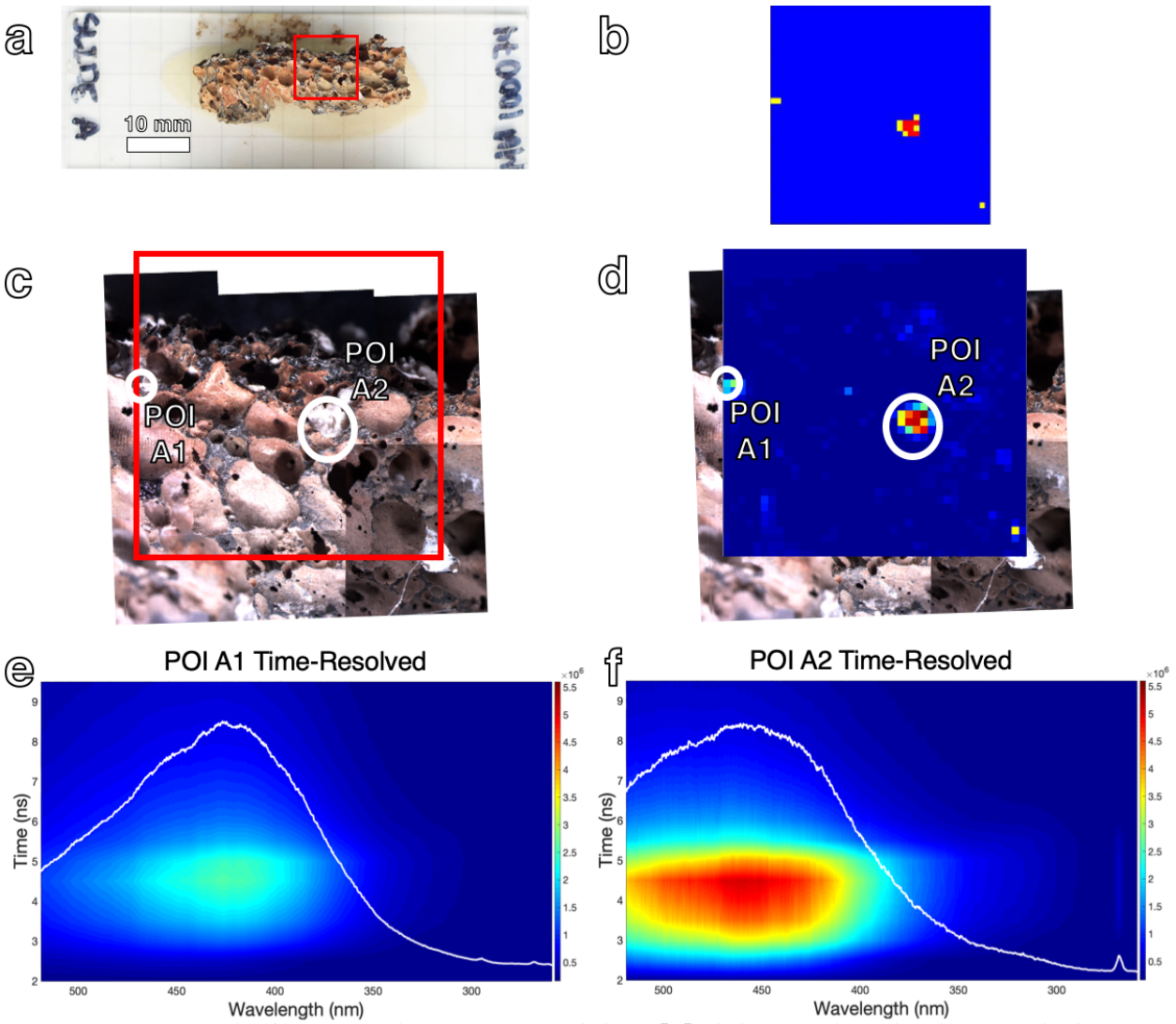

Figure 7.1 LIF results from sample MU100074, slide A. [a] Slide A, with scale, showing the location

of the LIF map (red box). [b] Absolute-scale comparative map. Excluding the yellow pixel in the bottom-right corner (as it is fluorescence from the correction fluid mark), there are two clear POIs, with one showing 7 red (very high) fluorescing pixels. [c] Composite microscopic image of the surface of the sample, with a red outline (one side = 10 mm) of the mapped area and identified POIs A1 and A2 circled in white. [d] Relative-scale 1600-point raster map overlain on composite microscope image, with POIs identified. [e] and [f] Absolute-scale, time-resolved contour plots of POIS A1 and A2, with overlain spectra at the time of maximum intensity, t = 4.5 ns. The small peak visible at wavelength = 266 nm is due to stray laser light entering the detector.

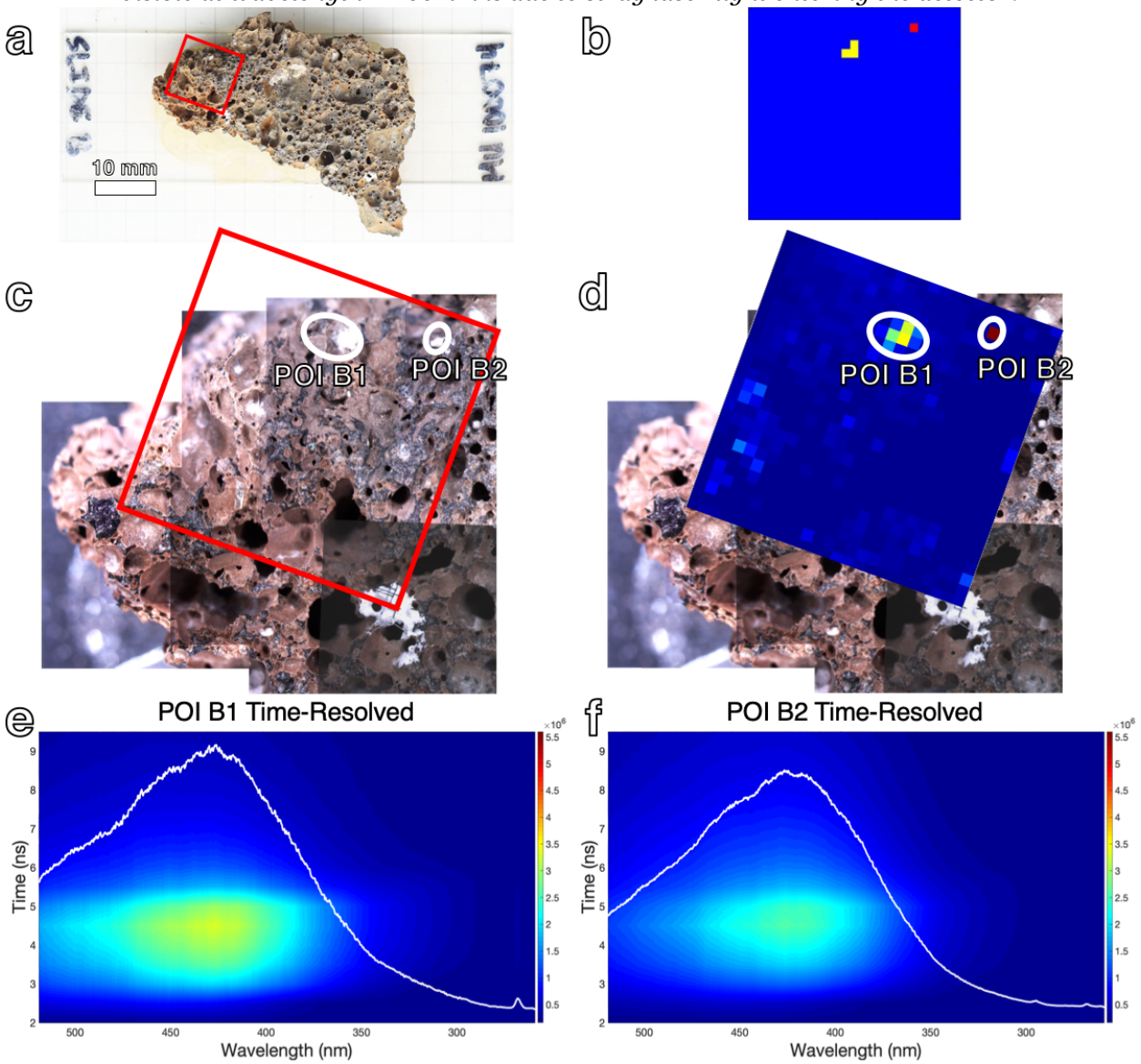

Figure 7.2 LIF results from sample MU100074, slide B. [a] Slide B, with scale, showing the location of the LIF map (red box). [b] Absolute-scale comparative map. There are two clear POIs: one with very high and one with high fluorescence intensity. [c] Composite microscopic image of the surface of the sample, with a red outline (one side = 10 mm) of the mapped area and identified POIs B1 and B2 circled in white. [d] Relative-scale 625-point raster map overlain on composite microscope image, with POIs identified. [e] and [f] Absolute-scale, time-resolved contour plots of POIs B1 and B2, with overlain spectra at the time of maximum intensity, t = 4.5 ns.

Slide E (fig. 7.3), in contrast, was mapped in the deep interior (fig. 7.3 [a]), and showed no vesicles in-filled with WCM (fig. 7.3 [c]). Map E had no POIs meriting further investigation (fig. 7.3 [d]). The absolute intensity scale map E (fig. 7.3 [b]) showed no yellow or red pixels, excluding those from the correction fluid mark.

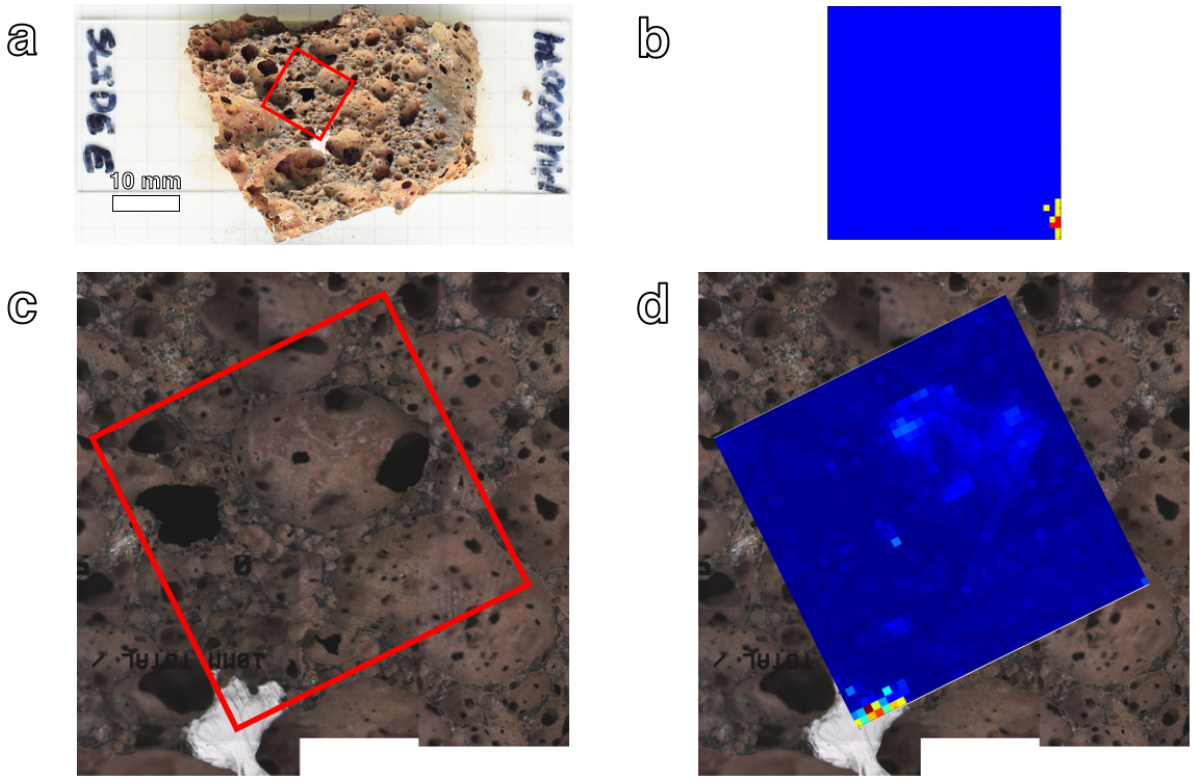

Figure 7.3 LIF results from sample MU100074, slide E. [a] Slide E, with scale, showing the location of the LIF map (red box). [b] Absolute-scale comparative map. There are no visible POIs, excluding the correction fluid fluorescence. [c] Composite microscopic image of the surface of the sample, with a red outline (one side = 10 mm) of the mapped area. [d] Relative-scale 1600-point raster map overlain on composite microscope image.

7.1.2 SEM results

POIs A1, A2, B1, and B2 from this sample were investigated in the SEM, and EDS point analyses were conducted to acquire an approximate elemental quantification, from which minerals could tentatively be identified (table 7.1; fig. 7.4). The minerals orthopyroxene (opx), forsterite (fo), amphibole (am), and pargasite (prg) were identified in the matrices surrounding the WCM in the POIs. The WCM was determined to be some kind of zeolite (zeo), with some possible chlorite (chl) content as well. Many of the EDS analysis points also contained some significant carbon component, with an average of 10 wt% CO_2 in POIs A1 and A2, and values of up to 36 wt% CO_2 in POIs B1 and B2.

Table 7.1 Example EDS point analysis results and the associated mineral identification. Results are reported in weight percent oxides, normalized. All iron is assumed to be present as FeO. If the CO_2 component is greater than 10 wt%, the rest of the elemental data were re-normalized without the CO_2 component for easier mineral identification, and the original CO_2 quantity is bolded.

POI	Mineral	SiO_2	TiO_2	Al_2O_3	FeO	MgO	CaO	Na_2O	K_2O	CO_2
A1	Pargasite	*43*	*2*	*16*	*11*	*9*	*13*	-	-	**16**
A2	Zeolite	*67*	-	*9*	-	*3*	*3*	-	-	**16**
A2	Clay/zeolite	48	3	17	17	2	4	-	-	8
B1	Chlorite	36	2	19	16	5	13	-	-	6
B1	Forsterite	41	-	-	13	39	-	-	-	7
B1	Orthopyroxene	43	-	-	15	40	-	-	-	1

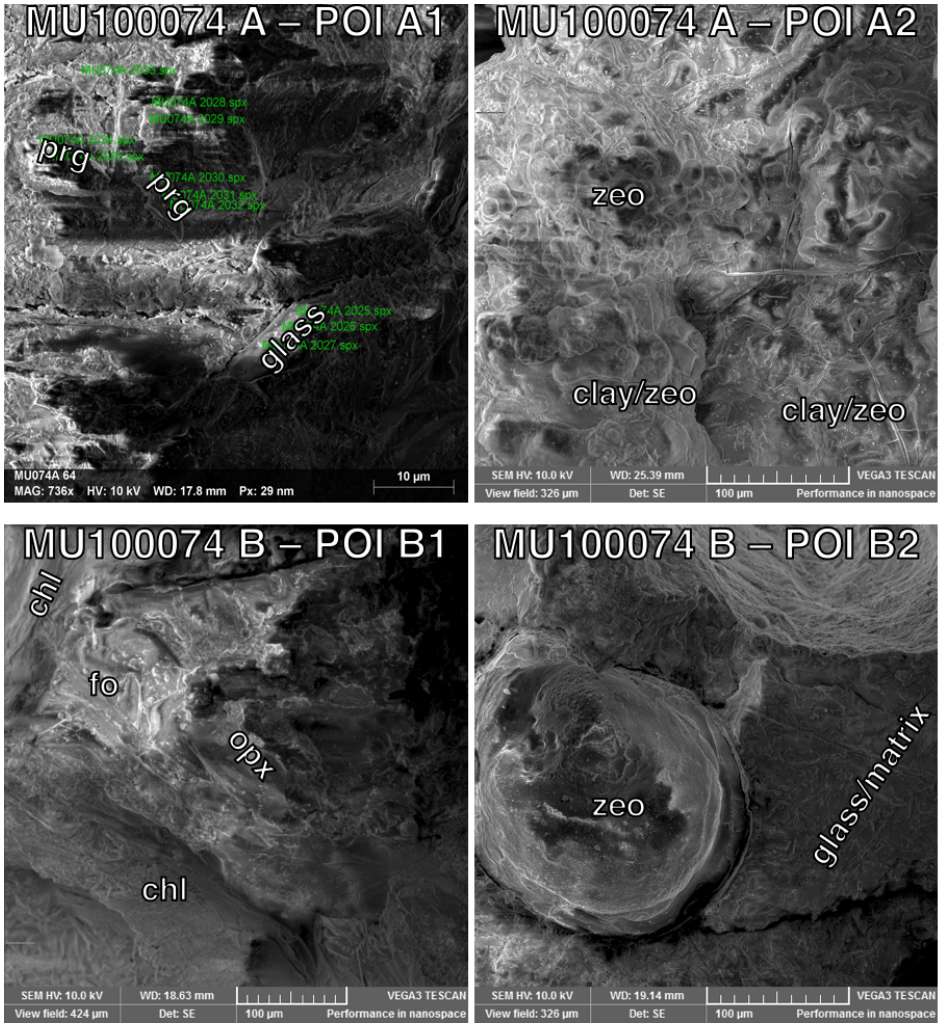

Figure 7.4 SEM images of POIs A1, A2, B1, and B2 from MU100074. Labelled within the images are the minerals identified from EDS point analyses: pargasite, zeolite, chlorite, forsterite, and orthopyroxene, along with a possible clay-zeo mix. The label glass/matrix shows where the

analysis produced inconclusive mineral identification, likely due to the material being too fine-grained compared to the size of the analysis point.

7.1.3 Porosity results

The pycnometer measurements produced mean skeletal volumes, $\boldsymbol{V_{skel.rock}}$ (based on ten trials each of two rock chips) of 0.316 $cm^3 \pm 0.011$ cm^3 and 0.380 $cm^3 \pm 0.011$ cm^3.

The μCT scanner measurements (fig. 7.5) produced bulk volumes, $\boldsymbol{V_{bulkrock}}$ (based on scans of two rock chips) of 0.626 cm^3 and 0.767 cm^3.

Therefore, the mean porosity fraction for this sample, $\boldsymbol{\varphi_{rock}}$, is 0.495 ± 0.022.

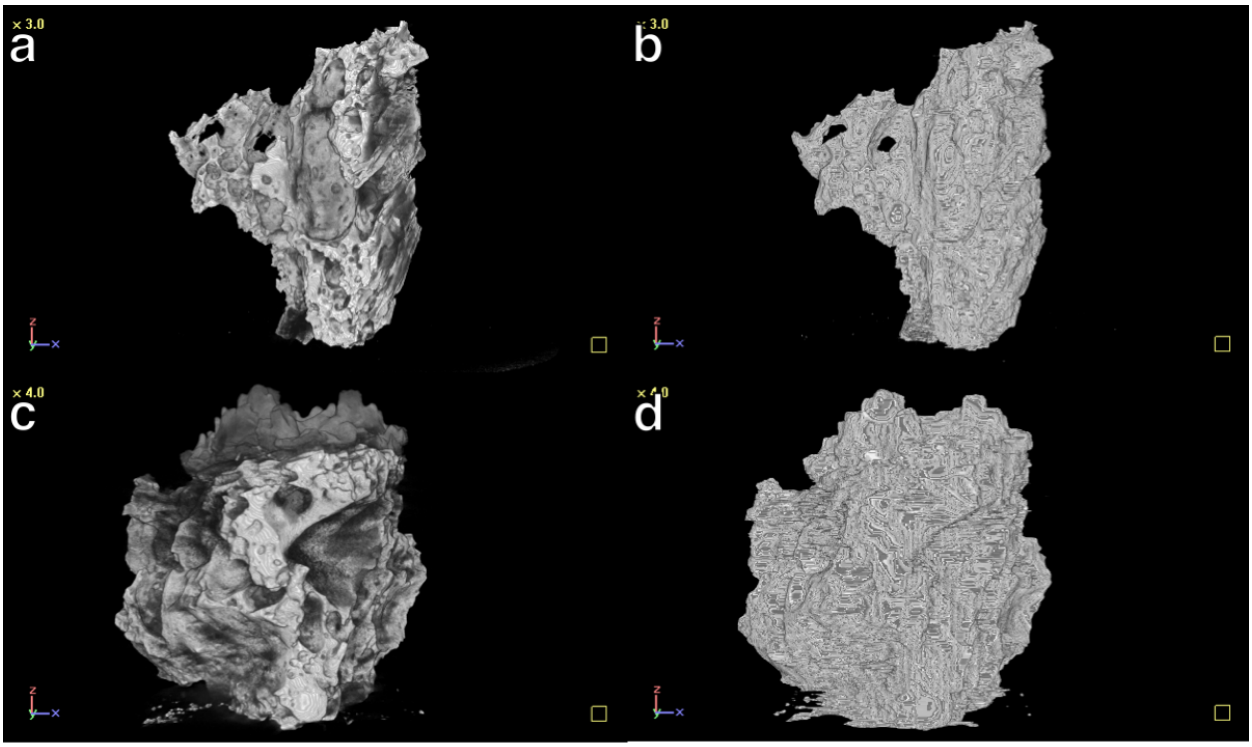

Figure 7.5 [a] The original μCT-generated 3D shape model of one of the MU100074 rock chips. [b] 3D shape model of the same rock chip as [b], post-processing. [c] Original 3D shape model of the second MU100074 rock chip. [d] 3D shape model of the same rock chip as [c], post-processing.

7.2 HI2016 – MU 100089 (Active Fumarole)

7.2.1 LIF mapping and LIF time-resolved results

Sample MU100089 was cut into three slides, with three 1600-point, 1 cm * 1 cm maps produced through LIF mapping. Maps A (fig. 7.6) and C (fig. 7.8) were both taken near the exposed edges of the sample, while map B (fig. 7.7) was taken within the sample interior. All three maps included abundant white crystalline material found within

vesicles. Maps A and C showed a combined three highly-fluorescent POIs, all associated with WCM, although the POI A1 was only associated with a small part of the total WCM visible in the map. The time-resolved spectra for POIs A1, C1, and C2 had a prominent, relatively sharp peak in the 425 – 450 nm range that reached its maximum intensity at 4.5 ns and showed a rapid decay time of approximately 2.5 ns. They also showed a much smaller and narrower peak at approximately 300 nm with a similar decay period.

Map A had a total of 1 red pixel and 5 yellow pixels (excluding those from the correction fluid mark), with a combined approximate area of 1.5 mm^2, based on the map step size of 0.25 mm. Map C contained 1 red pixel and 8 yellow pixels, with a combined approximate area of 2.25 mm^2, based on the map step size of 0.25 mm.

Map B had two POIs. Similarly to Map A, POIs B1 and B2 only represented a small portion of the total WCM visible in the map. The time-resolved spectrum of POI B1 was similar in shape and decay to A1, C1, and C2, although much less intense and with no narrow peak at 300 nm. The time-resolved spectrum of POI B2 had a broad, relatively low-intensity peak at approximately 350 nm, reaching its maximum intensity at 5 ns and with a much more gradual decay time of greater than 8 ns.

Map B had a total of 7 red pixels and 39 yellow pixels (excluding those from the correction fluid mark), with a combined approximate area of 11.5 mm^2, based on the map step size of 0.25 mm.

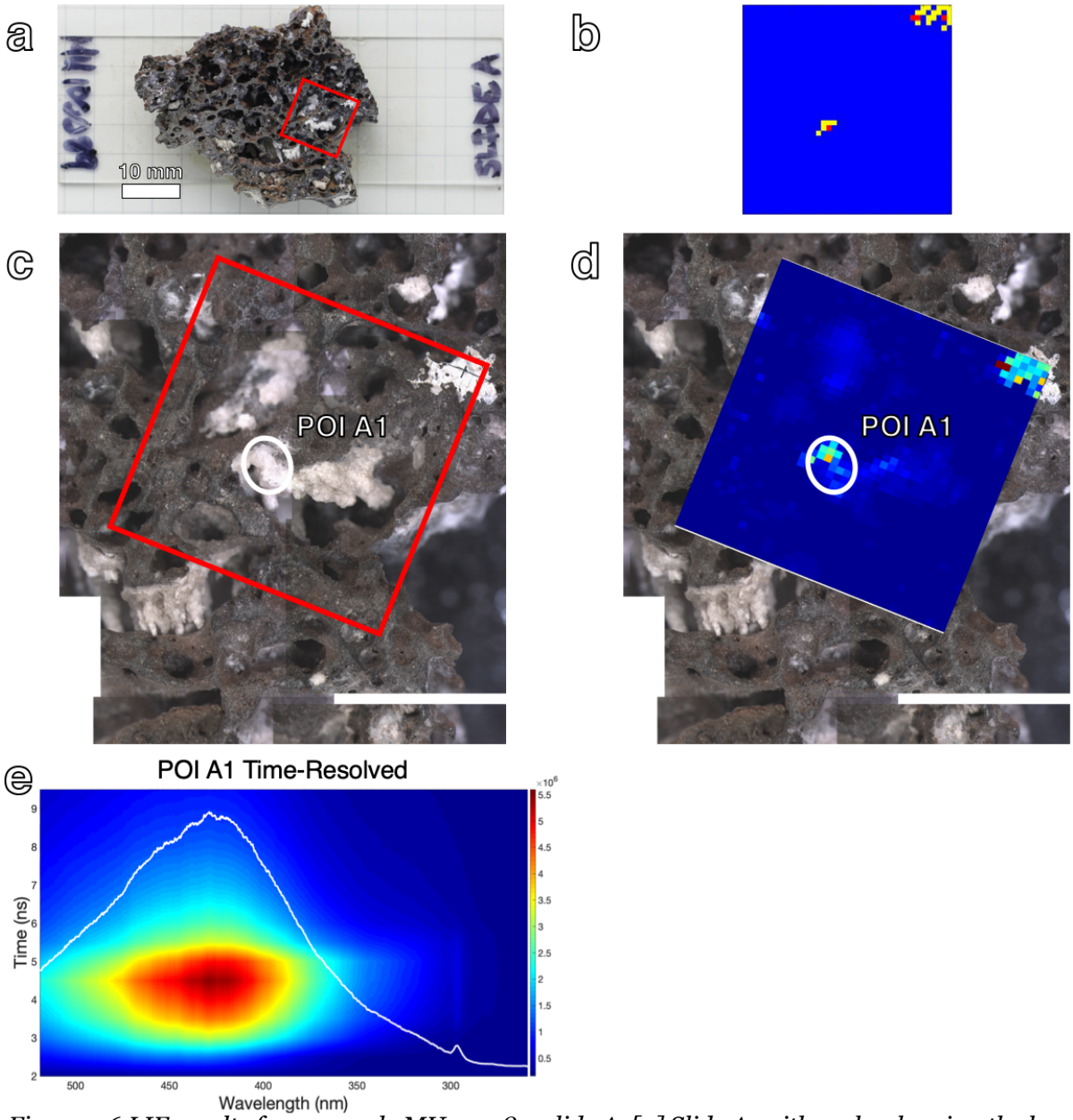

Figure 7.6 LIF results from sample MU100089, slide A. [a] Slide A, with scale, showing the location of the LIF map (red box). [b] Absolute-scale comparative map. There is one clear POI with moderately high and high fluorescence intensity. [c] Composite microscopic image of the surface of the sample, with a red outline (one side = 10 mm) of the mapped area and identified POI A1 circled in white. [d] Relative-scale 1600-point raster map overlain on composite microscope image, with

POI identified. [e] Absolute-scale, time-resolved contour plot of POI A1, with overlain spectrum at the time of maximum intensity, t = 4.5 ns.

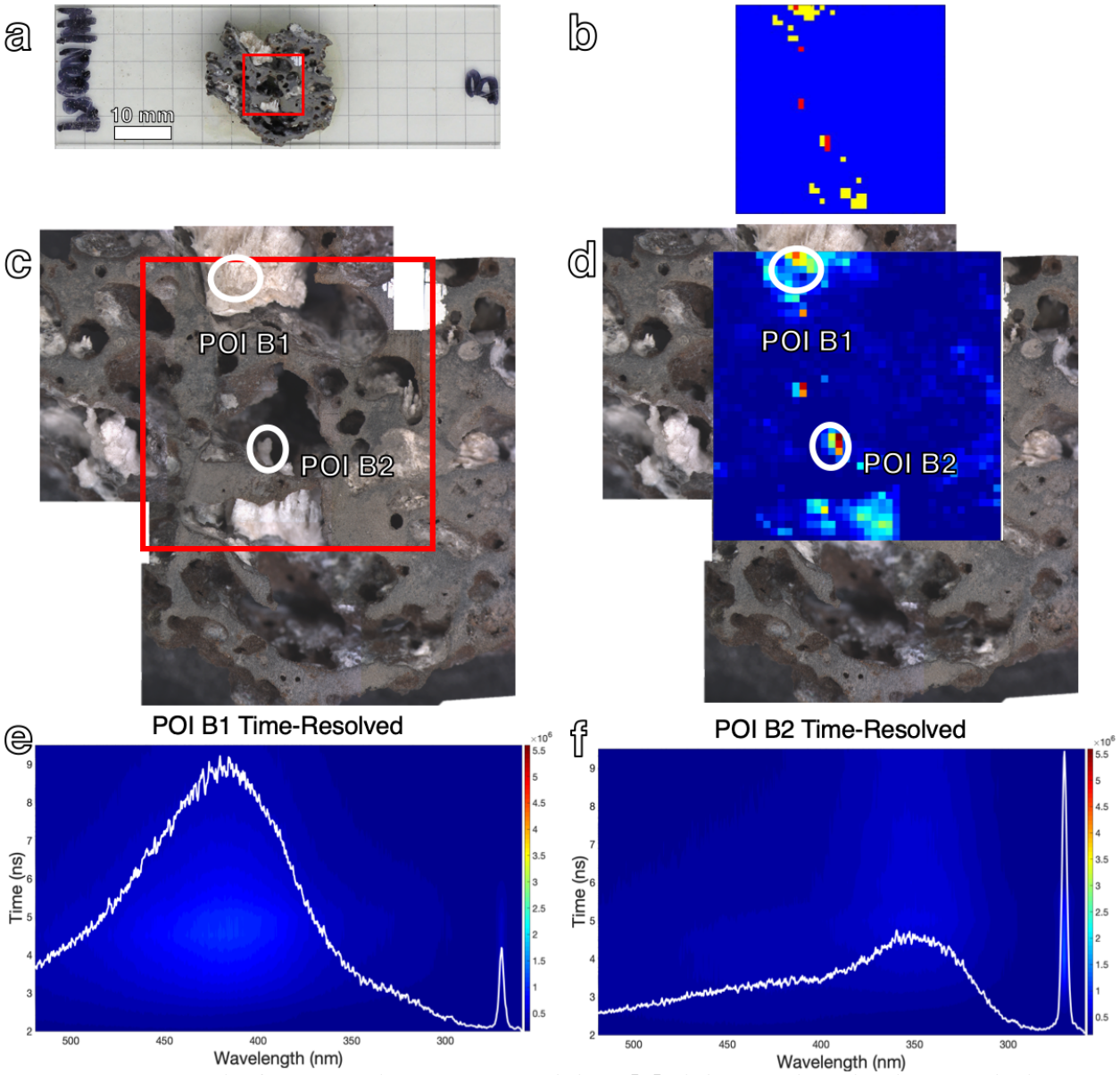

Figure 7.7 LIF results from sample MU100089, slide B. [a] Slide B, with scale, showing the location of the LIF map (red box). [b] Absolute-scale comparative map. There are multiple areas of high fluorescence intensity, although only two POIs were chosen for further analysis. [c] Composite microscopic image of the surface of the sample, with a red outline (one side = 10 mm) of the mapped area and identified POIs B1 and B2 circled in white. [d] Relative-scale 1600-point raster map overlain on composite microscope image, with POIs identified. [e] and [f] Absolute-scale, time-resolved contour plots of POIs B1 and B2, with overlain spectra at the time of maximum intensity, t = 4.5 ns.

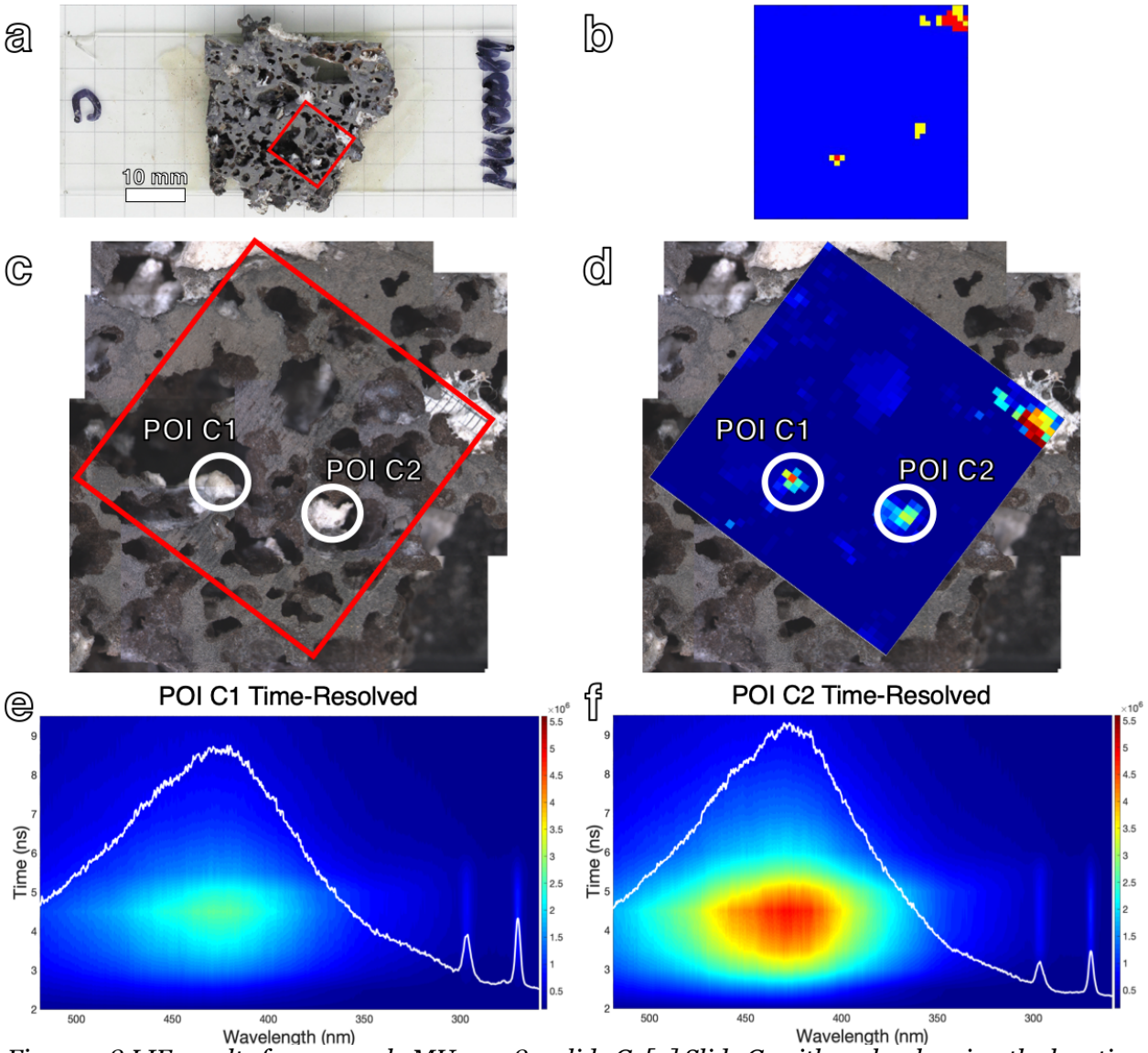

Figure 7.8 LIF results from sample MU100089, slide C. [a] Slide C, with scale, showing the location of the LIF map (red box). [b] Absolute-scale comparative map. There are two clear POIs: one with very high and one with high fluorescence intensity. [c] Composite microscopic image of the surface of the sample, with a red outline (one side = 10 mm) of the mapped area and identified POIs C1 and C2 circled in white. [d] Relative-scale 1600-point raster map overlain on composite microscope image, with POIs identified. [e] and [f] Absolute-scale, time-resolved contour plots of POIs C1 and C2, with overlain spectra at the time of maximum intensity, t = 4.5 ns.

7.2.2 SEM results

POIs A1, B1, C1, and C2 from this sample were investigated in the SEM, and EDS point analyses were conducted to acquire an approximate elemental quantification, from which minerals could tentatively be identified (table 7.2; fig. 7.9). POI B2 was at a difficult angle relative to the EDS detector, and so could not be analysed. The minerals clinopyroxene

(cpx), labradorite-anorthite (lab-an), and amphibole (am), were identified in the matrices surrounding the WCM in the POIs. The WCM was determined to be some kind of zeolite, likely heaulandite or stilbite (hul/stb) with some possible chlorite or other clay content as well. Many of the EDS analysis points also showed some significant carbon component, with an average of between 5 and 13 wt% CO_2 from all POIs. POI A1 had some points with 20 – 35 wt% CO_2 and one measurement with 74 wt% CO_2.

Table 7.2 Example EDS point analysis results and the associated mineral identification. Results are reported in weight percent oxides, normalized. All iron is assumed to be present as FeO. If the CO_2 component is greater than 10 wt%, the rest of the elemental data were re-normalized without the CO_2 component for easier mineral identification, and the original CO_2 quantity is bolded.

POI	Mineral	SiO_2	TiO_2	Al_2O_3	FeO	MgO	CaO	Na_2O	K_2O	CO_2
A1-1	Amphibole	*44*	*1*	*14*	*6*	*22*	*12*	*1*	-	**19**
A1-1	Clinopyroxene	46	1	6	6	18	16	-	-	8
A1-1	Labradorite-anorthite	51	-	29	1	1	13	-	-	8
A1-2	Zeolite	61	-	23	-	1	7	-	-	8
A1-2	Carbon-rich material	12	-	11	-	2	1	-	-	74
B1	Heulandite/stilbite	59	-	20	-	1	10	-	1	8
C1	Clay/zeolite	40	1	27	7	8	9	-	-	7
C1	Clinopyroxene	50	2	7	9	16	15	-	-	2

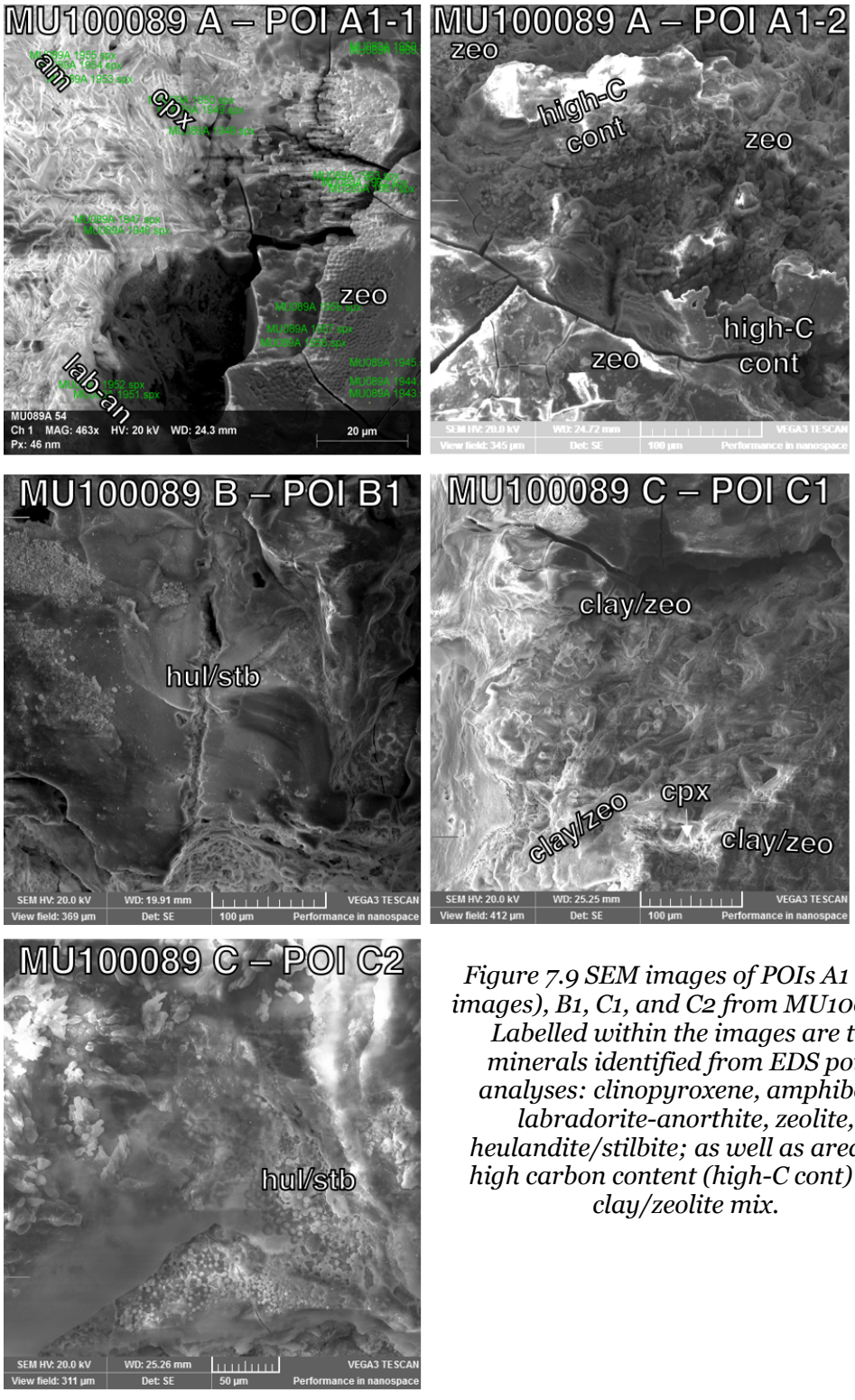

Figure 7.9 SEM images of POIs A1 (two images), B1, C1, and C2 from MU100089. Labelled within the images are the minerals identified from EDS point analyses: clinopyroxene, amphibole, labradorite-anorthite, zeolite, heulandite/stilbite; as well as areas of high carbon content (high-C cont) and clay/zeolite mix.

7.2.3 Porosity results

The pycnometer measurements produced mean skeletal volumes, $V_{skel.rock}$ (based on ten trials each of two rock chips) of 0.451 $cm^3 \pm 0.011$ cm^3 and 0.314 $cm^3 \pm 0.011$ cm^3.

The μCT scanner measurements (fig. 7.10) produced bulk volumes, $V_{bulkrock}$ (based on scans of two rock chips) of 0.702 cm^3 and 0.527 cm^3.

Therefore, the mean porosity fraction for this sample, φ_{rock}, is 0.381 ± 0.015.

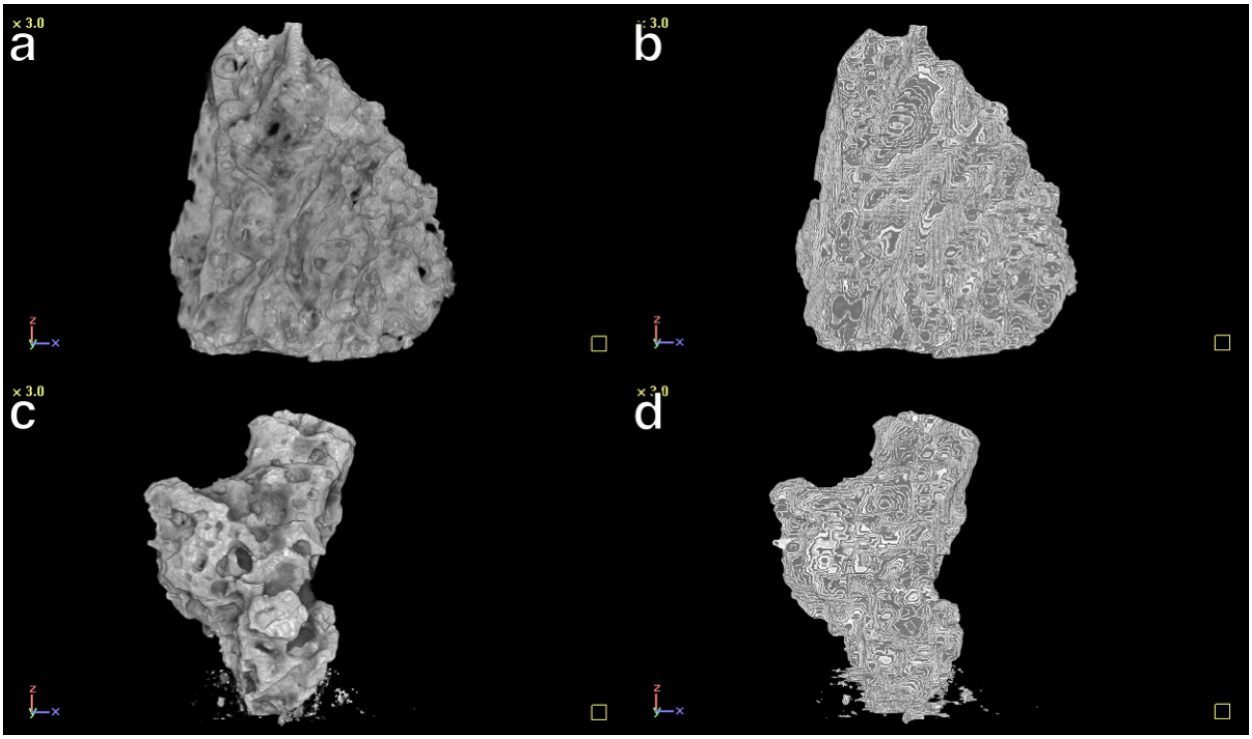

Figure 7.10 [a] The original μCT-generated 3D shape model of one of the MU100089 rock chips.[b] 3D shape model of the same rock chip as [a], post-processing. [c] Original 3D shape model of the second MU100074 rock chip. [d] 3D shape model of the same rock chip as [c], post-processing.

7.3 HI2016 – MU 100620 (Relict Fumarole)

7.3.1 LIF mapping and LIF time-resolved results

Sample MU100620 was cut into three slides, with three 1600-point, 1 cm * 1 cm maps produced through LIF mapping. Map A (fig. 7.11) was taken near an exposed edge, and included many vesicles containing greenish-white crystalline material. Map B (fig. 7.12) was taken tangential to an exposed edge and included smaller amounts of WCM within its vesicles. Map C (fig. 7.13) included more of the interior of the sample, and had less WCM at the mapping surface level.

The map A absolute intensity scale showed a total of 67 red pixels and 103 yellow pixels (excluding those from the correction fluid mark), with a combined approximate area of 42.5 mm^2, based on the map step size of 0.25 mm. The map B intensity scale

contained 2 red pixels and 23 yellow pixels, with a combined approximate area of 6.25 mm^2. The map C intensity scale contained 12 red pixels and 47 yellow pixels, with a combined approximate area of 14.75 mm^2.

POIs A1, A2, A3, C1, and C2 all had very similar spectral signatures, with a main peak located around 440 nm, similar maximum intensities, and similar decay times of approximately 2.5 ns. POIs A4, B1, and B2 had similar shapes at their maximum intensities to POIs A1, A2, A3, C1, and C2, but much lower maximum intensities. A3, A4, B2, C1, and C2 also showed a significant secondary peak at approximately 350 nm with a decay period extending beyond the measured time.

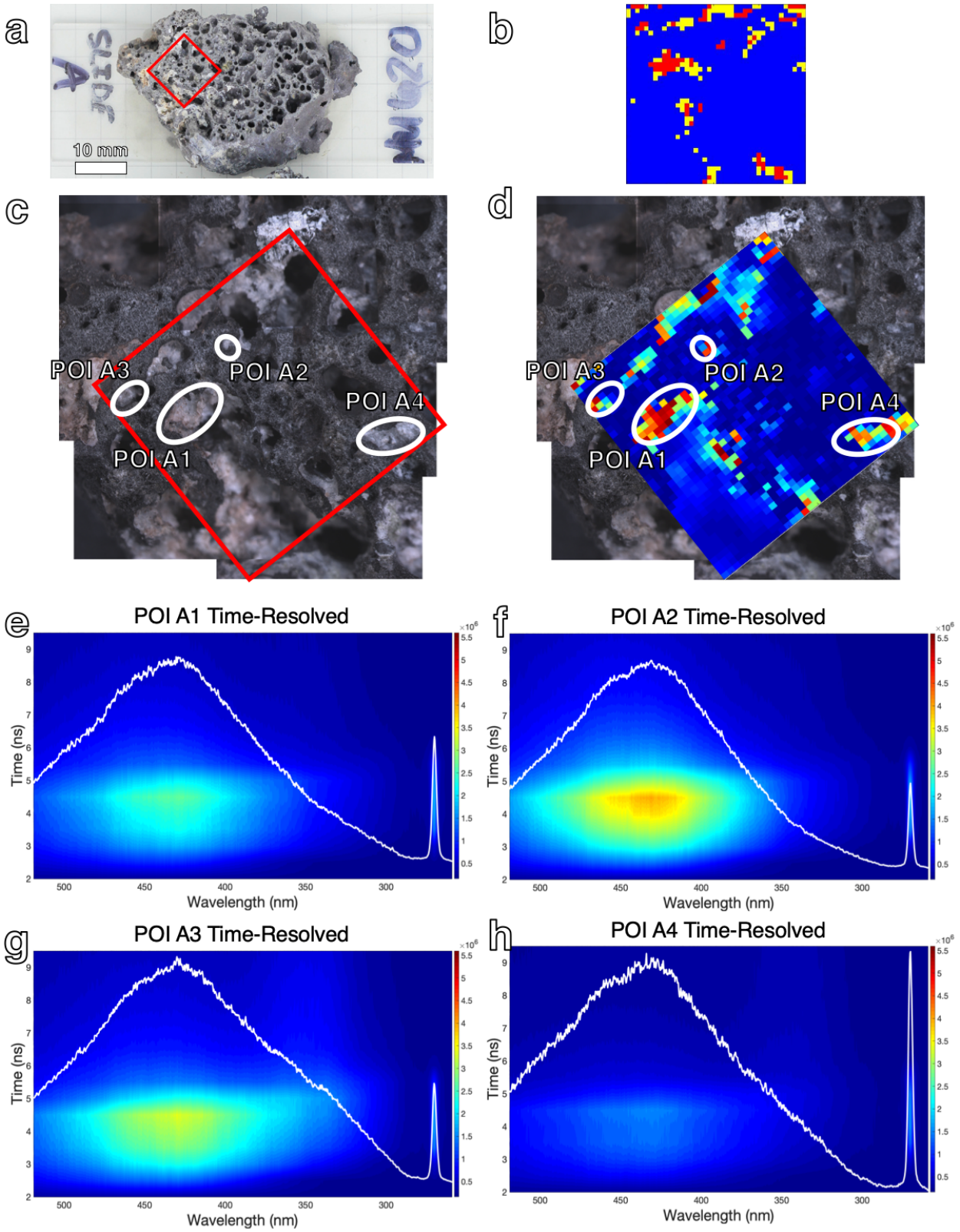

Figure 7.11 LIF results from sample MU100620, slide A. [a] Slide A, with scale, showing the location of the LIF map (red box). [b] Absolute-scale comparative map. There are many areas within the map showing high or very high intensity fluorescence. [c] Composite microscopic image

of the surface of the sample, with a red outline (one side = 10 mm) of the mapped area and identified POIs A1 through A4 circled in white. [d] Relative-scale 1600-point raster map overlain on composite microscope image, with POIs identified. [e] and [f] Absolute-scale, time-resolved contour plots of POIs A1 through A4, with overlain spectra at the time of maximum intensity, t = 4.5 ns.

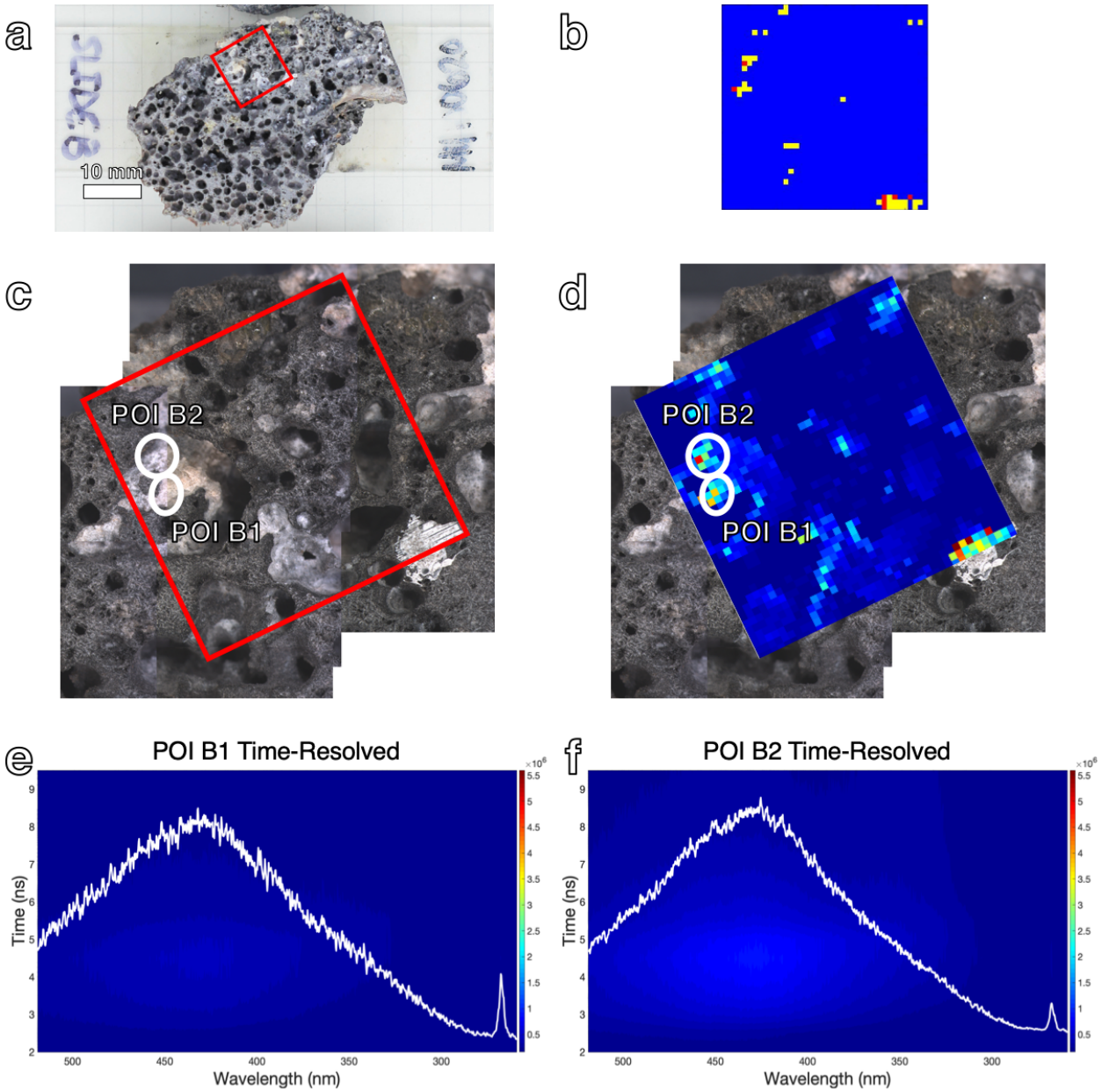

Figure 7.12 LIF results from sample MU100620, slide B. [a] Slide A, with scale, showing the location of the LIF map (red box). [b] Absolute-scale comparative map. There are two red pixels showing high intensity, which were chosen as POIs. [c] Composite microscopic image of the surface of the sample, with a red outline (one side = 10 mm) of the mapped area and identified POIs B1 and B2 circled in white. [d] Relative-scale 1600-point raster map overlain on composite microscope image, with POIs identified. [e] and [f] Absolute-scale, time-resolved contour plots of POIs B1 and B2, with overlain spectra at the time of maximum intensity, t = 4.5 ns.

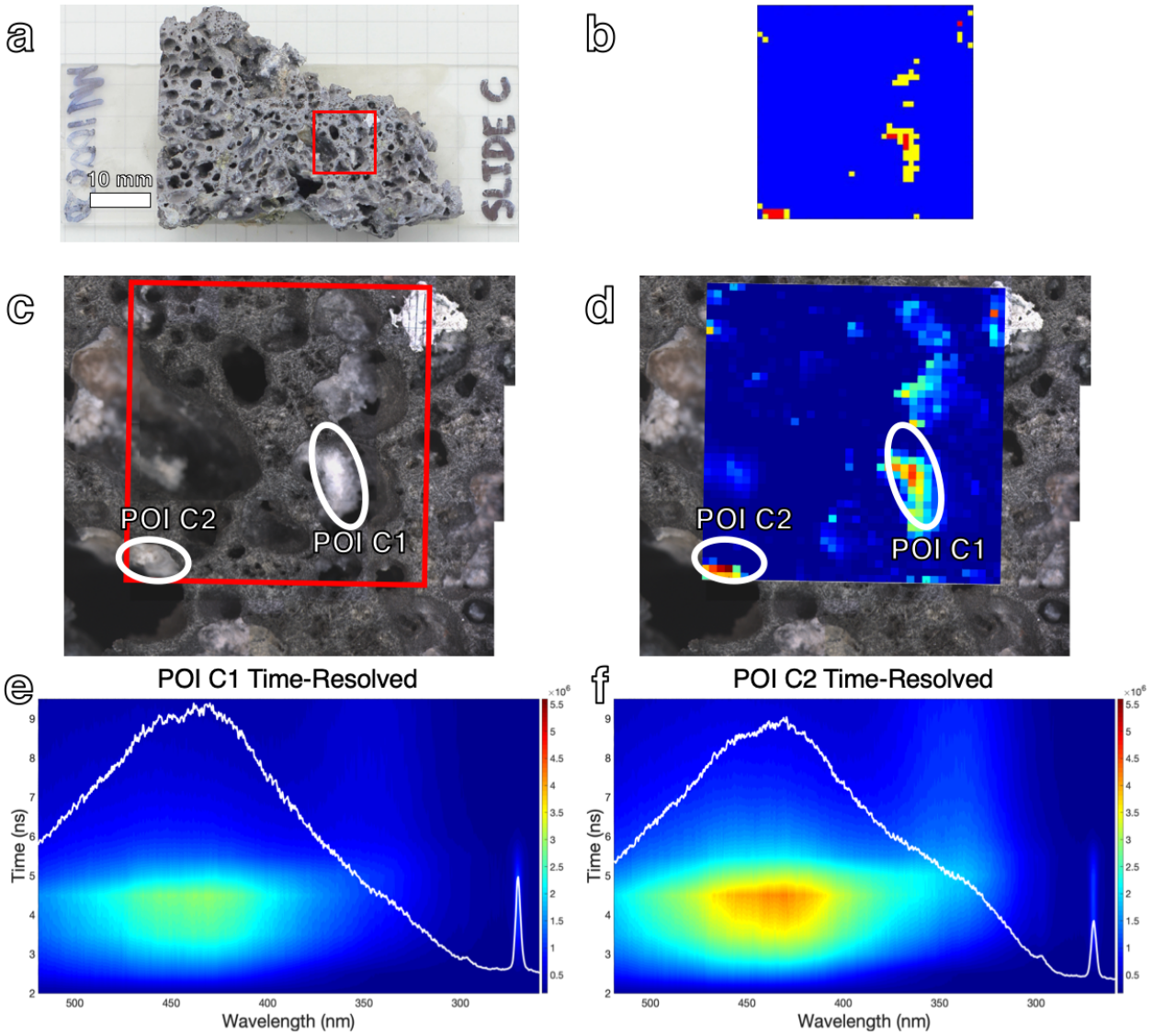

Figure 7.13 LIF results from sample MU100620, slide C. [a] Slide C, with scale, showing the location of the LIF map (red box). [b] Absolute-scale comparative map. The two areas with red pixels (high intensity fluorescence) were chosen as POIs. [c] Composite microscopic image of the surface of the sample, with a red outline (one side = 10 mm) of the mapped area and identified POIs C1 and C2 circled in white. [d] Relative-scale 1600-point raster map overlain on composite microscope image, with POIs identified. [e] and [f] Absolute-scale, time-resolved contour plots of POIs C1 and C2, with overlain spectra at the time of maximum intensity, t = 4.5 ns.

7.3.2 SEM results

All POIs from this sample were investigated in the SEM, and EDS point analyses were conducted to acquire an approximate elemental quantification, from which minerals could tentatively be identified (table 7.3; fig. 7.14). The minerals orthopyroxene, labradorite-anorthite/plagioclase (plg), and amphibole, were identified in the matrices

surrounding the WCM in the POIs. The WCM could not conclusively be identified due to the high carbon content, although some chlorite signatures were found. All POIs except for B1 showed a significant amount of carbon, with average weight percent CO_2 values ranging from 12 to 51 %. POIs A1, A3, A4, B2, and C1 all had point measurements with over 50 wt% CO_2, and POIs A3 and C1 contained multiple points with over 80 wt% CO_2.

Table 7.3 Example EDS point analysis results and the associated mineral identification. Results are reported in weight percent oxides, normalized. All iron is assumed to be present as FeO.

POI	Mineral	SiO_2	TiO_2	Al_2O_3	FeO	MgO	CaO	Na_2O	K_2O	CO_2
A2-1	Labradorite-anorthite	45	-	29	2	-	-	13	4	6
A2-1	Orthopyroxene	43	-	2	14	36	1	-	-	3
A3	Carbon-rich material	21	-	5	1	-	1	1	-	71
A4	Chlorite	21	-	11	41	18	-	-	-	9
B1	Silica glass/mix	79	-	7	2	2	2	-	-	8
C2	Amphibole	48	1	10	10	15	11	1	-	4

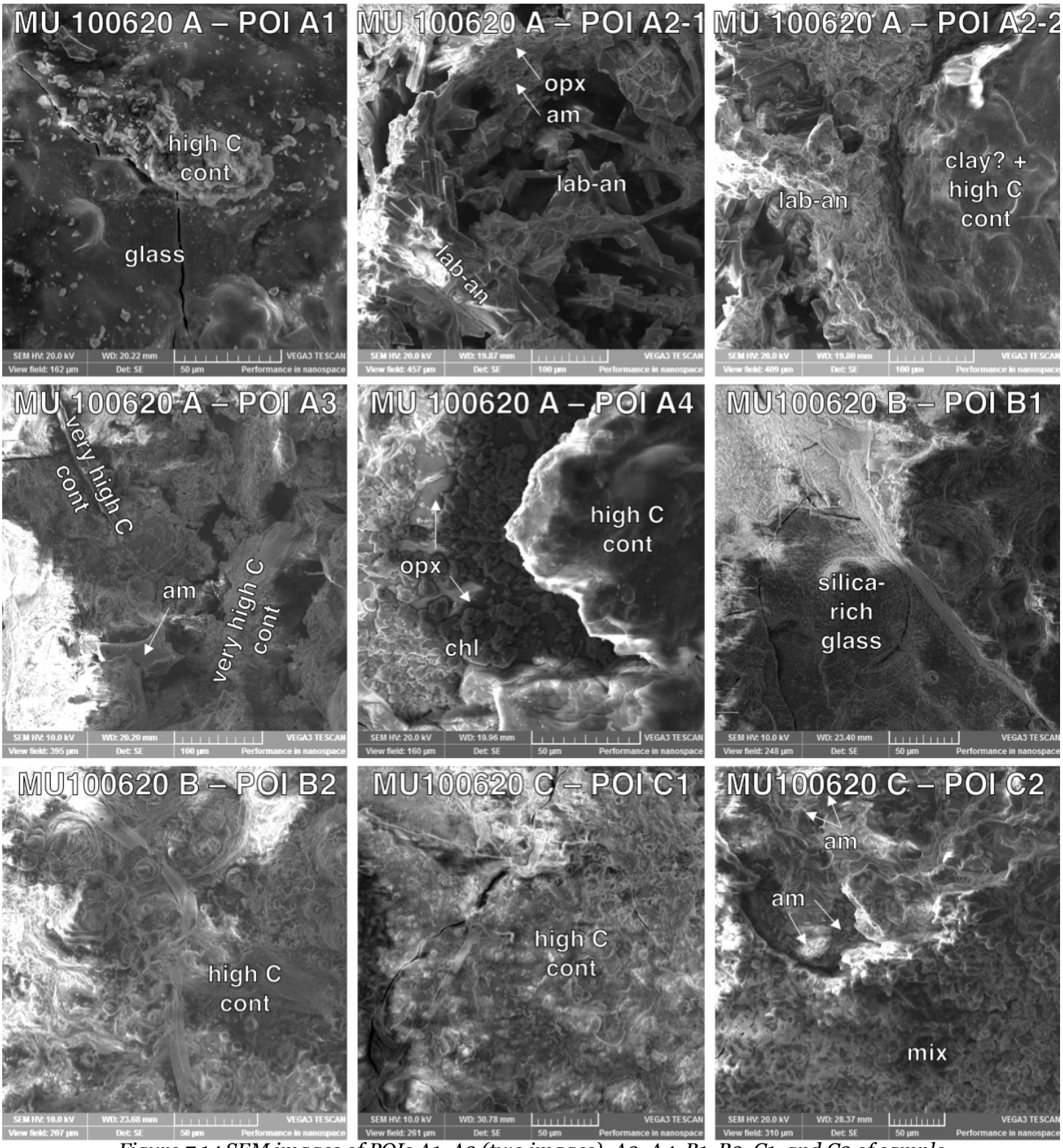

Figure 7.14 SEM images of POIs A1, A2 (two images), A3, A4, B1, B2, C1, and C2 of sample MU100620. Labelled within the images are the minerals identified from EDS point analyses: orthopyroxene, amphibole, labradorite-anorthite, and chlorite; as well as areas of high carbon content (high-C cont) and glass or fine-grained matrix.

7.3.3 Porosity results

The pycnometer measurements produced mean skeletal volumes, $V_{skel.rock}$ (based on ten trials each of two rock chips) of 1.035 cm^3 ± 0.012 cm^3 and 0.643 cm^3 ± 0.011 cm^3.

The μCT scanner measurements (fig. 7.15) produced bulk volumes, $V_{bulkrock}$ (based on scans of two rock chips) of 1.675 cm^3 and 0.987 cm^3.

Therefore, the mean porosity fraction for this sample, φ_{rock}, is 0.365 ± 0.007 .

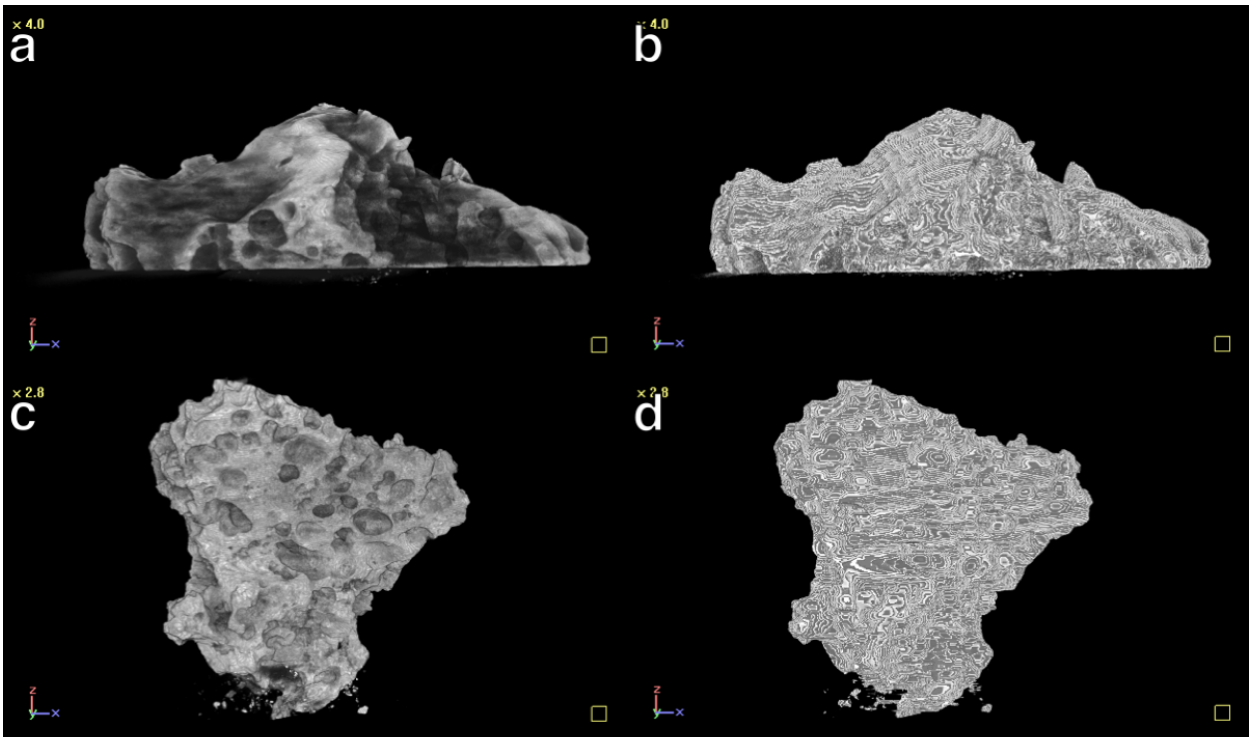

Figure 7.15 [a] The original μCT-generated 3D shape model of one of the MU100620 rock chips. [b] 3D shape model of the same rock chip as [a], post-processing. [c] Original 3D shape model of the second MU100074 rock chip. [d] 3D shape model of the same rock chip as [c], post-processing.

7.4 HI2016 – MU 100110 (Unaltered)

7.4.1 LIF mapping and LIF time-resolved results

Sample MU100110 was cut into one slide, with one 400-point, 1 cm * 1 cm map produced through LIF mapping. Map A (fig. 7.16) was taken near an exposed edge, and included some vesicles containing a thin coating of WCM, as well as visible olivine phenocrysts.

POIs A1 and A2 had somewhat similar spectra, both with prominent broad peaks at approximately 440 nm and 360 nm, with a smaller, narrow peak at 300 nm, and both showed maximum intensity at 4.0 ns. The 440 nm peak in both spectra was relatively low-

intensity compared to other samples, but showed the same quick decay time of 2 – 2.5 ns. The 360 nm peak in both spectra showed a much longer decay time of greater than 8 ns. In POI A1, the two peaks were almost equal in intensity, with the 440 nm peak being slightly higher. In POI A2, the 360 nm peak was prominently higher than the 440 nm peak.

The map A absolute intensity scale showed a total of 3 red pixels and 5 yellow pixels, with a combined approximate area of 4 mm^2, based on the map step size of 0.5 mm.

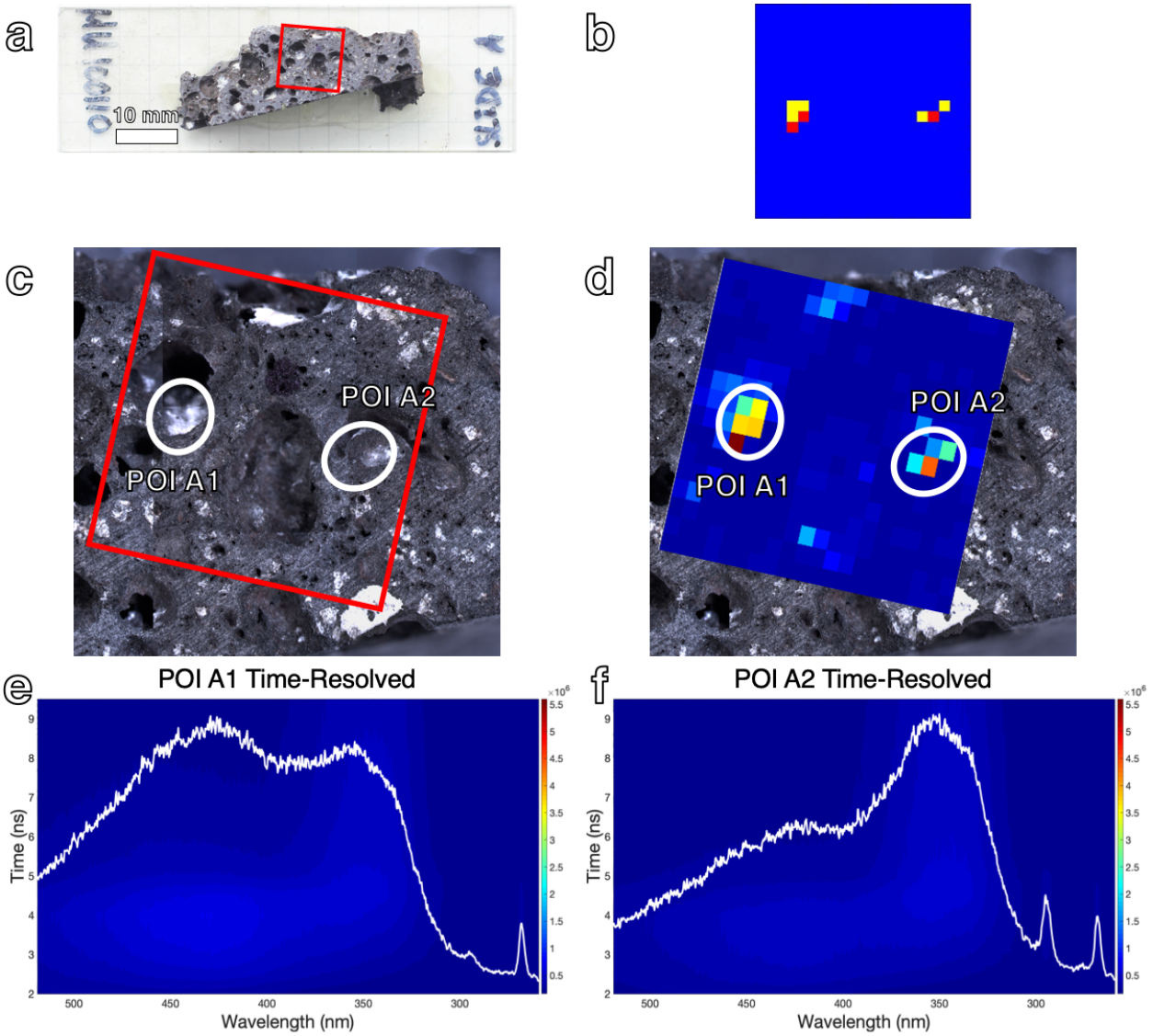

Figure 7.16 LIF results from sample MU100110, slide A. [a] Slide A, with scale, showing the location of the LIF map (red box). [b] Absolute-scale comparative map. The two areas with red pixels (high intensity fluorescence) were chosen as POIs. [c] Composite microscopic image of the surface of the sample, with a red outline (one side = 10 mm) of the mapped area and identified POIs A1 and A2

circled in white. [d] Relative-scale 400-point raster map overlain on composite microscope image, with POIs identified. [e] and [f] Absolute-scale, time-resolved contour plots of POIs A1 and A2, with overlain spectra at the time of maximum intensity, t = 4.0 ns.

7.4.2 SEM results

Both POIs from this sample were investigated in the SEM, and EDS point analyses were conducted to acquire an approximate elemental quantification, from which minerals could tentatively be identified (table 7.4; fig. 7.17). Acquiring accurate EDS readings was difficult, due to the position of the WCM against the sub-vertical walls of the vesicles.

The mineral amphibole, along with silica-rich material were identified in the matrices surrounding the WCM in the POIs. The WCM could not conclusively be identified due to the EDS detector angle, but some readings suggested a clay signature. Moderate amounts of carbon were measured in both POIs, with an average of 11 wt% CO_2 detected in A1 and 14 wt% CO_2 detected in A2.

Table 7.4 Example EDS point analysis results and the associated mineral identification. Results are reported in weight percent oxides, normalized. All iron is assumed to be present as FeO.

POI	Mineral	SiO_2	TiO_2	Al_2O_3	FeO	MgO	CaO	Na_2O	K_2O	CO_2
A1	Clay	48	3	16	9	7	9	2	1	5
A1	Silica glass/matrix	77	-	7	-	1	-	-	-	15
A2	Amphibole	50	2	16	7	4	9	3	1	8

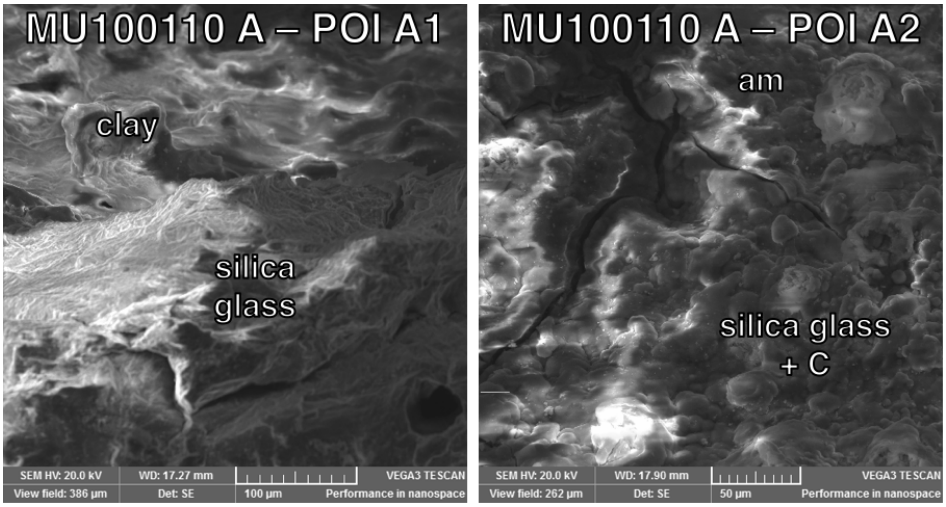

Figure 7.17 SEM images of POIs A1 and A2 of sample MU100110. Labelled within the images are the minerals and materials identified from EDS point analyses: amphibole, silica glass or fine-grained matrix, clay, and carbon.

7.4.3 Porosity results

The pycnometer measurements produced a mean skeletal volume, $V_{skel.rock}$ (based on ten trials of one rock chip) of 2.194 $cm^3 \pm 0.013$ cm^3.

The μCT scanner measurements (fig. 7.18) produced a bulk volume, $V_{bulkrock}$ of 3.064 cm^3.

Therefore, the mean porosity fraction for this sample, φ_{rock}, is 0.284 ± 0.002.

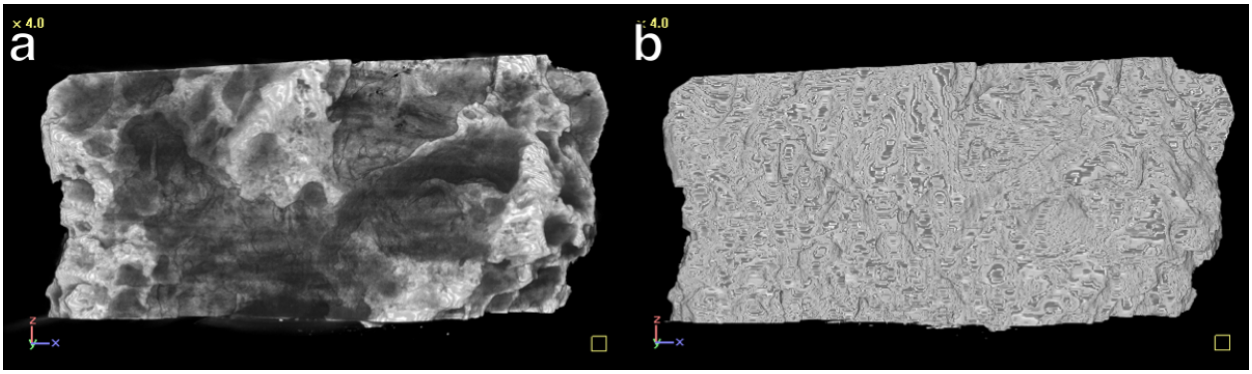

Figure 7.18 [a] The original μCT-generated 3D shape model of the MU100110 rock chip. [b] 3D shape model of the same rock chip as [a], post-processing.

7.5 ID2016 – HF437 (High-Temperature Alteration)

7.5.1 LIF mapping and LIF time-resolved results

Sample HF437 was cut into four slides, with four 1600-point, 1 cm * 1 cm maps produced through LIF mapping. Map A (fig. 7.19) was taken in the rock's interior, and contains the transition zone between dark brown-black material to a streak of bright orange-brown altered rock. Map B (fig. 7.20) is also an interior map, although the entire slide surface is homogeneous and black. Map C (fig. 7.21) was taken with one edge tangential to an exposed edge, and contains similar homogeneous black material to map B. Map D (fig. 7.22) has one edge tangential to an exposed edge, and contains dark black to brown rock. None of the sample slides show any vesicle infills.

Map A was the only map to contain POIs. POIs A1 and A2 had similar spectra, both with prominent broad peaks at approximately 440 nm (higher intensity) and 360 nm (lower intensity), and both showed maximum intensity at 4.5 ns. The 440 nm peak in both spectra was relatively low-intensity compared to other samples, but showed the

same quick decay time of 2 – 2.5 ns. In POI A2, the 360 nm peak was more prominent than in POI A1, but still lower than the 440 nm peak.

The map A absolute intensity scale showed a total of 2 red pixels, with a combined approximate area of 0.5 mm^2, based on the map step size of 0.25 mm. Maps B, C, and D contained no red or yellow pixels outside of those from the correction fluid spot.

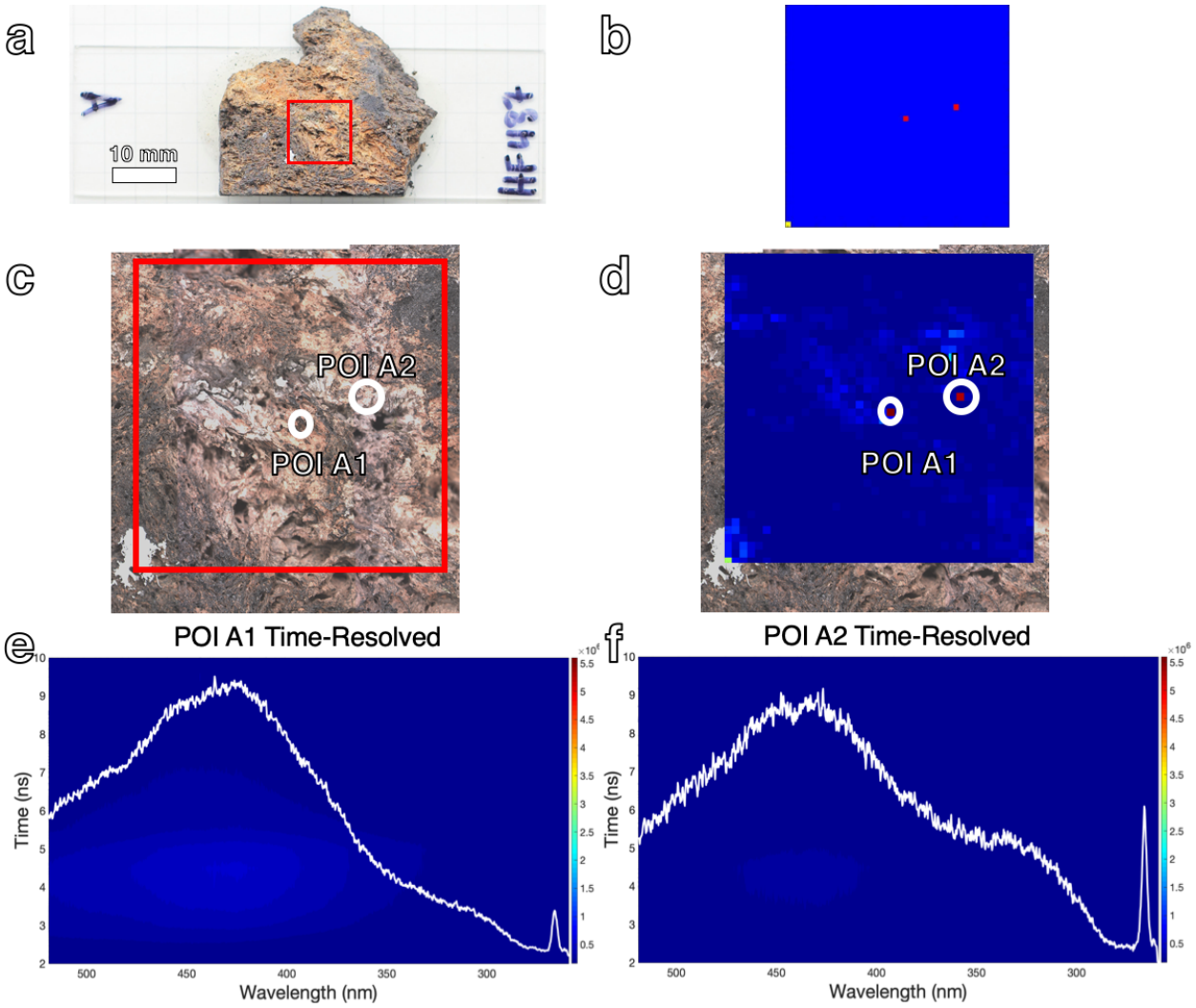

Figure 7.19 LIF results from sample HF437, slide A. [a] Slide A, with scale, showing the location of the LIF map (red box). [b] Absolute-scale comparative map. The two red pixels were chosen as POIs. [c] Composite microscopic image of the surface of the sample, with a red outline (one side = 10 mm) of the mapped area and identified POIs A1 and A2 circled in white. [d] Relative-scale 1600-point raster map overlain on composite microscope image, with POIs identified. [e] and [f] Absolute-scale, time-resolved contour plots of POIs A1 and A2, with overlain spectra at the time of maximum intensity, t = 4.5 ns.

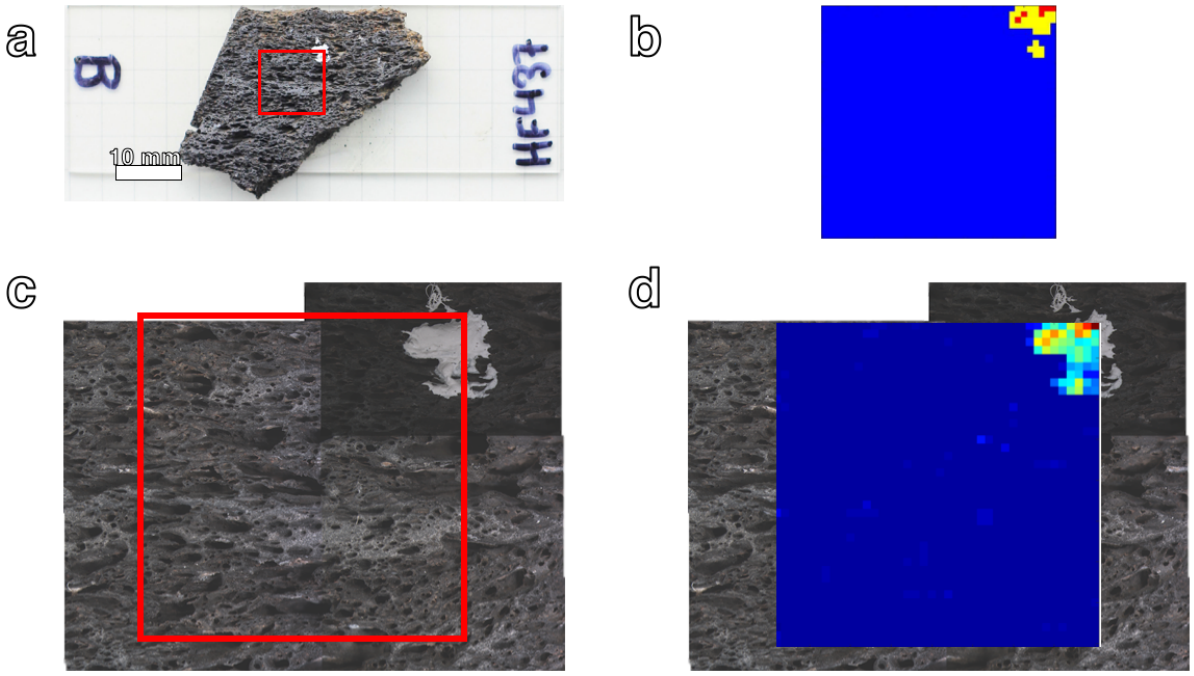

Figure 7.20 LIF results from sample HF437, slide B. [a] Slide B, with scale, showing the location of the LIF map (red box). [b] Absolute-scale comparative map. [c] Composite microscopic image of the surface of the sample, with a red outline (one side = 10 mm) of the mapped area. [d] Relative-scale 1600-point raster map overlain on composite microscope image.

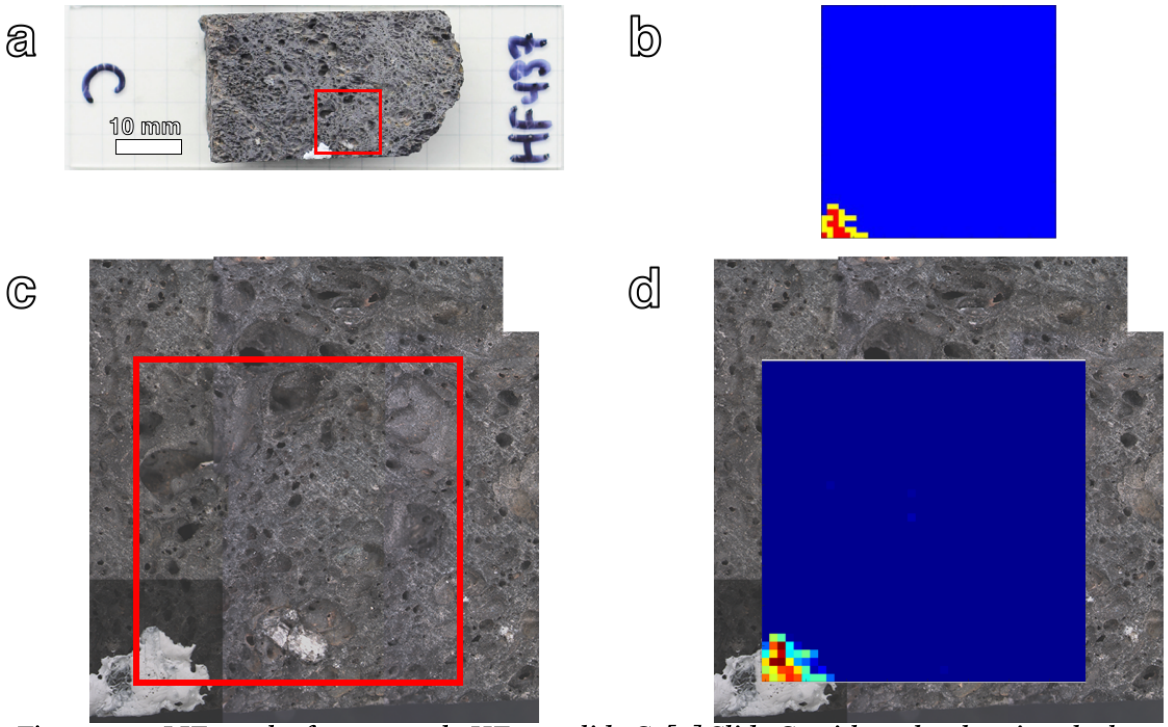

Figure 7.21 LIF results from sample HF437, slide C. [a] Slide C, with scale, showing the location of the LIF map (red box). [b] Absolute-scale comparative map. [c] Composite microscopic image of

the surface of the sample, with a red outline (one side = 10 mm) of the mapped area. [d] Relative-scale 1600-point raster map overlain on composite microscope image.

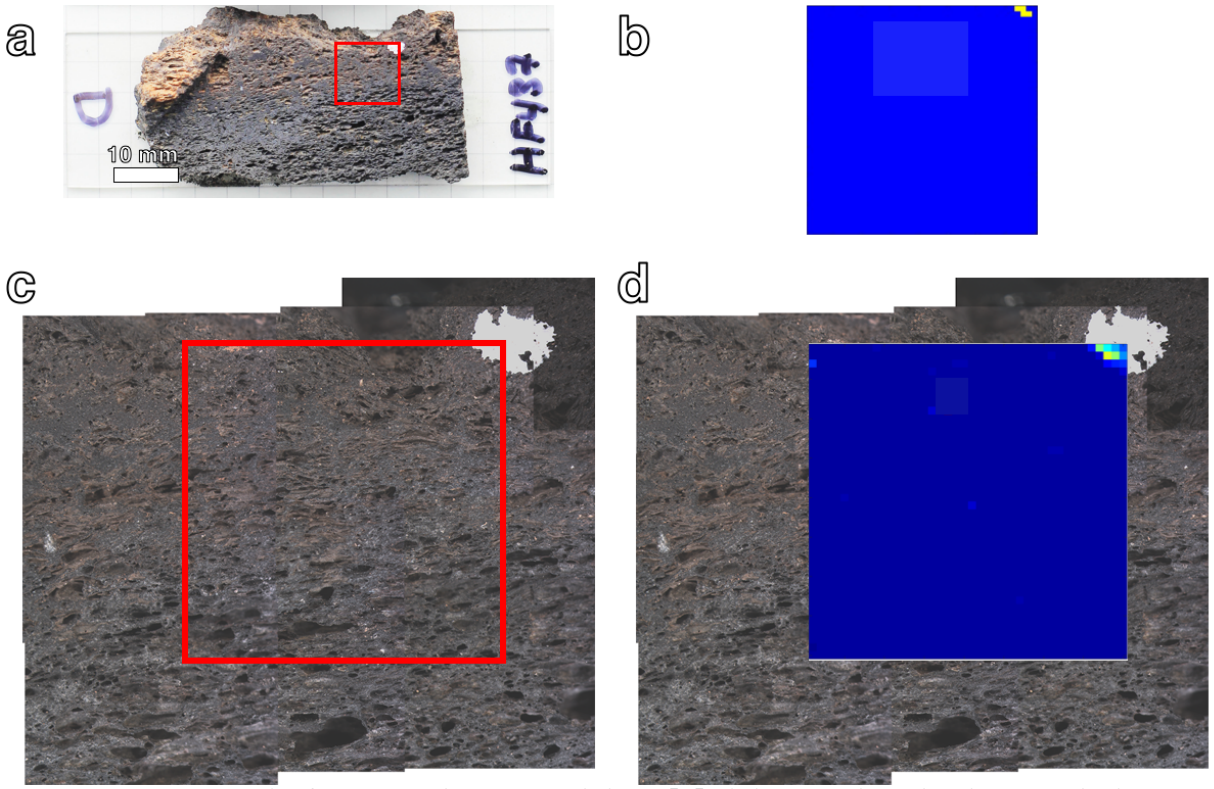

Figure 7.22 LIF results from sample HF437, slide D. [a] Slide D, with scale, showing the location of the LIF map (red box). [b] Absolute-scale comparative map. [c] Composite microscopic image of the surface of the sample, with a red outline (one side = 10 mm) of the mapped area. [d] Relative-scale 1600-point raster map overlain on composite microscope image.

7.5.2 SEM results

Both POIs from this sample were investigated in the SEM, and EDS point analyses were conducted to acquire an approximate elemental quantification, from which minerals could tentatively be identified (table 7.5; fig. 7.23)

The minerals amphibole, fayalite (fa) clay minerals illite (ill) and motmorillonite (mnt), along with silica-rich material were identified in the POIs. Moderate to high amounts of carbon were measured in both POIs, with an average of 41 wt% CO_2 detected in A1 and 28 wt% CO_2 detected in A2. A1 had some points with 80 – 90 wt% CO_2 and A2 had points with 50 – 67 wt% CO_2.

Table 7.5 Example EDS point analysis results and the associated mineral identification. Results are reported in weight percent oxides, normalized. All iron is assumed to be present as FeO. If the CO_2

component is greater than 10 wt%, the rest of the elemental data were re-normalized without the CO_2 component for easier mineral identification, and the original CO_2 quantity is bolded.

POI	Mineral	SiO_2	TiO_2	Al_2O_3	FeO	MgO	CaO	Na_2O	K_2O	CO_2
A1	Carbon-rich material	19	-	5	1	1	1	1	1	71
A1	Silica glass/matrix	71	-	12	1	1	1	-	1	13
A2	Fayalite	35	-	5	52	1	-	-	1	6
A2	Amphibole	49	1	8	7	7	17	-	1	10
A2	Montmorillonite	*64*	-	*23*	*4*	*2*	*1*	*1*	*4*	**24**
A2	Illite	*60*	*1*	*17*	*9*	*3*	*3*	*1*	*6*	**34**

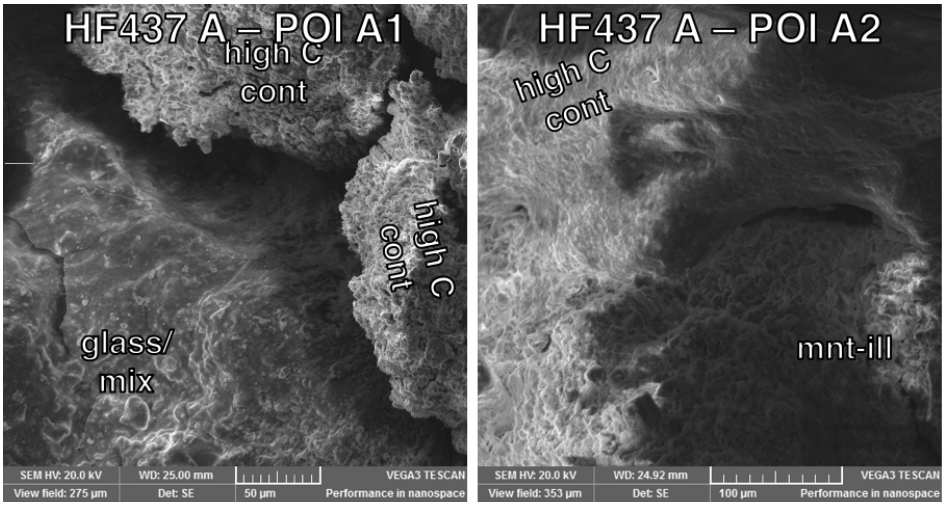

Figure 7.23 SEM images of POIs A1 and A2 of sample HF437. Labelled within the images are the minerals and materials identified from EDS point analyses: glass/matrix, montmorillonite and illite, and material with high carbon content.

7.5.3 Porosity results

The pycnometer measurements produced a mean skeletal volume, $V_{skel.rock}$ (based on ten trials of one rock chip) of 0.862 $cm^3 \pm 0.011$ cm^3.

The μCT scanner measurements (fig. 7.24) produced a bulk volume, $V_{bulkrock}$ of 2.011 cm^3.

Therefore, the mean porosity fraction for this sample, φ_{rock}, is 0.571 ± 0.007.

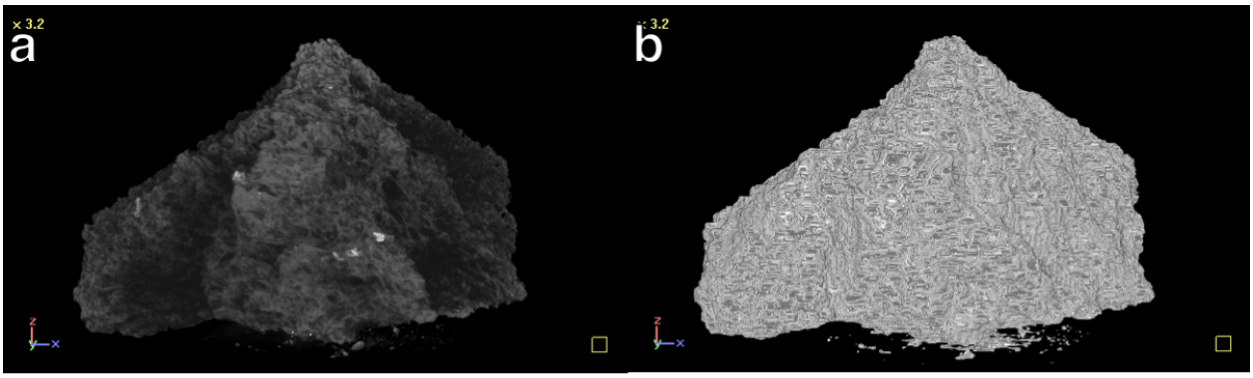

Figure 7.24 [a] The original μCT-generated 3D shape model of the HF437 rock chip. [b] 3D shape model of the same rock chip as [a], post-processing.

7.6 ID2016 – BC459 (Moderate- to High-Temperature Alteration)

7.6.1 LIF mapping and LIF time-resolved results

Sample BC459 was cut into four slides, although slide B became contaminated during processing and was removed from the suite. Three 1600-point, 1 cm * 1 cm maps were produced through LIF mapping. Map A (fig. 7.25) was taken near an exposed surface. Map C (fig. 7.26) was taken in the interior of the slide, and contains vesicles with both light yellow surfaces and darker brown surfaces. Map D (fig. 7.27) has one edge tangential to an exposed edge, and contains a yellow-surfaced vesicle. None of the sample slides show any vesicle infills; the colours described above are the colours of the actual rock surface, not some secondary deposit.

None of the maps had POIs that were investigated further. While some showed one or two single pixels that were very high intensity, the extremely low-intensity immediate surroundings and lack of any distinct visual features at these pixels' locations indicate the likelihood of these pixels being cosmic ray measurements or noise. These spurious detections were investigated with time-resolved fluorescence, but showed consistent response with other background measurements. The red pixels in the absolute-scale intensity maps were therefore excluded from my analysis.

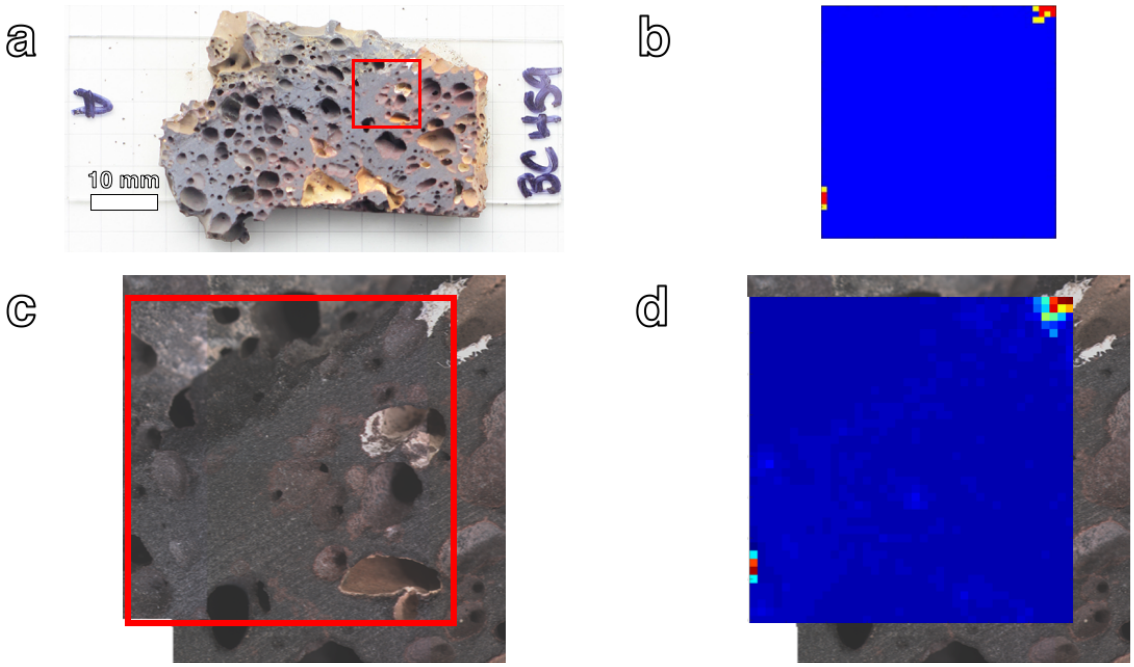

Figure 7.25 LIF results from sample BC459, slide A. [a] Slide A, with scale, showing the location of the LIF map (red box). [b] Absolute-scale comparative map. [c] Composite microscopic image of the surface of the sample, with a red outline (one side = 10 mm) of the mapped area. [d] Relative-scale 1600-point raster map overlain on composite microscope image.

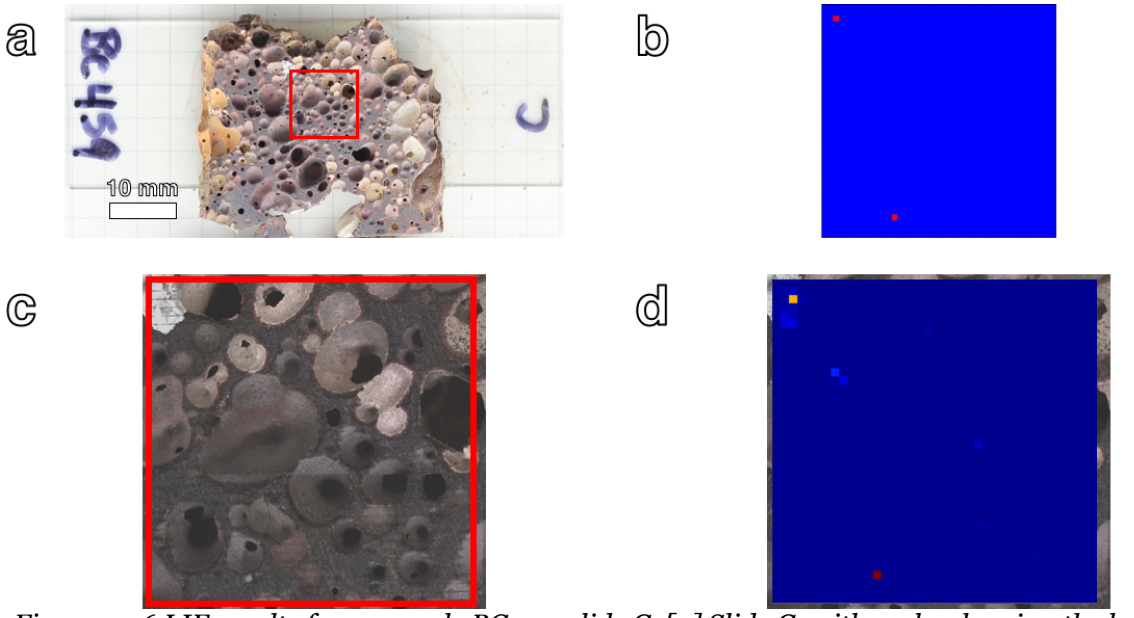

Figure 7.26 LIF results from sample BC459, slide C. [a] Slide C, with scale, showing the location of the LIF map (red box). [b] Absolute-scale comparative map. [c] Composite microscopic image of

the surface of the sample, with a red outline (one side = 10 mm) of the mapped area. [d] Relative-scale 1600-point raster map overlain on composite microscope image.

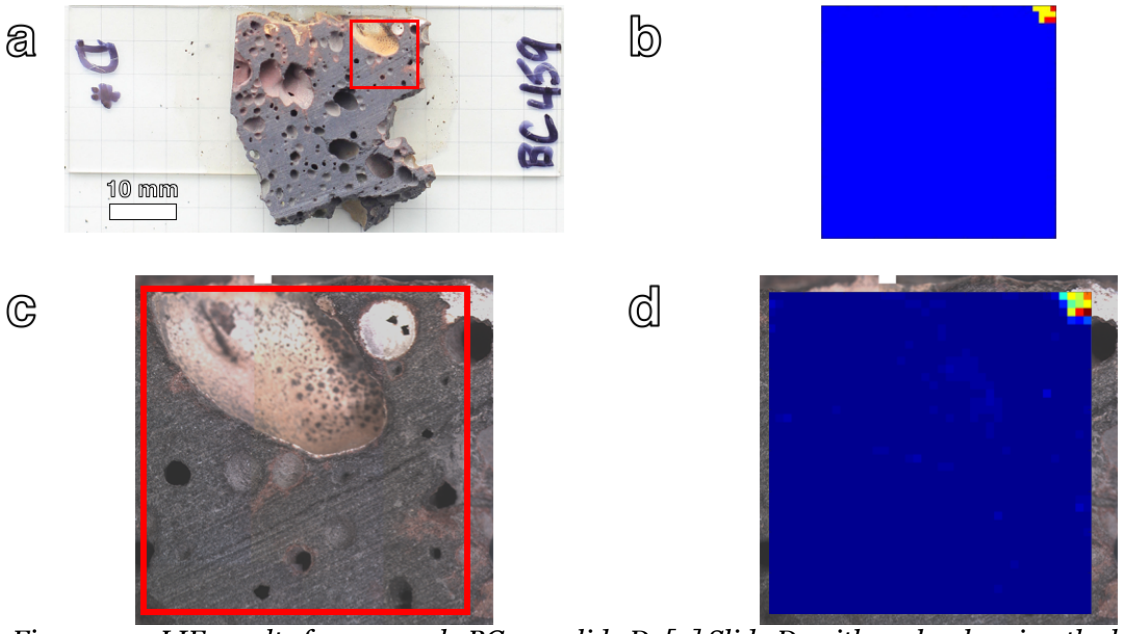

Figure 7.27 LIF results from sample BC459, slide D. [a] Slide D, with scale, showing the location of the LIF map (red box). [b] Absolute-scale comparative map. [c] Composite microscopic image of the surface of the sample, with a red outline (one side = 10 mm) of the mapped area. [d] Relative-scale 1600-point raster map overlain on composite microscope image.

Due to the lack of POIs present in this sample, no SEM analyses were performed.

7.6.2 Porosity results

The pycnometer measurements produced a mean skeletal volume, $V_{skel.rock}$ (based on ten trials of one rock chip) of 1.640 $cm^3 \pm 0.012$ cm^3.

The μCT scanner measurements (fig. 7.28) produced a bulk volume, $V_{bulkrock}$ of 2.610 cm^3.

Therefore, the mean porosity fraction for this sample, φ_{rock}, is 0.372 ± 0.003.

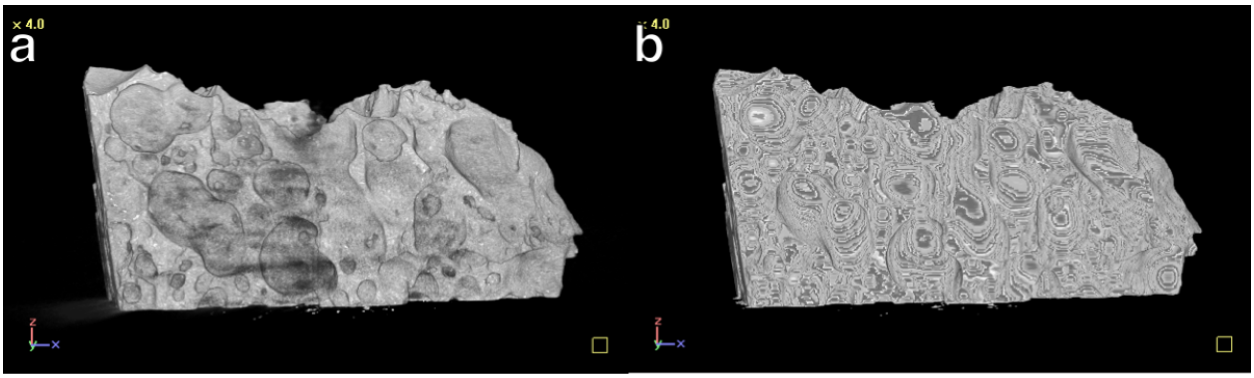

Figure 7.28 [a] The original 3D μCT-generated shape model of the BC459 rock chip. [b] 3D shape model of the same rock chip as [a], post-processing.

7.7 ID2016 – HF257 (Low-Temperature Alteration)

7.7.1 LIF mapping and LIF time-resolved results

Sample HF257 was cut into four slides, with four 1600-point, 1 cm * 1 cm maps produced through LIF mapping. Map A (fig. 7.29) was taken near an exposed edge of the sample. Map B (fig. 7.30) is a mostly interior map with one corner near an exposed edge. Map C (fig. 7.31) is an interior map (one side is tangential to a cut edge). Map D (fig. 7.32) overlaps an angled exposed edge of the sample. All maps show a similar homogeneous black-brown colour and size/size distribution of vesicles. None of the sample slides show any vesicle infills. None of the maps had POIs that were investigated further.

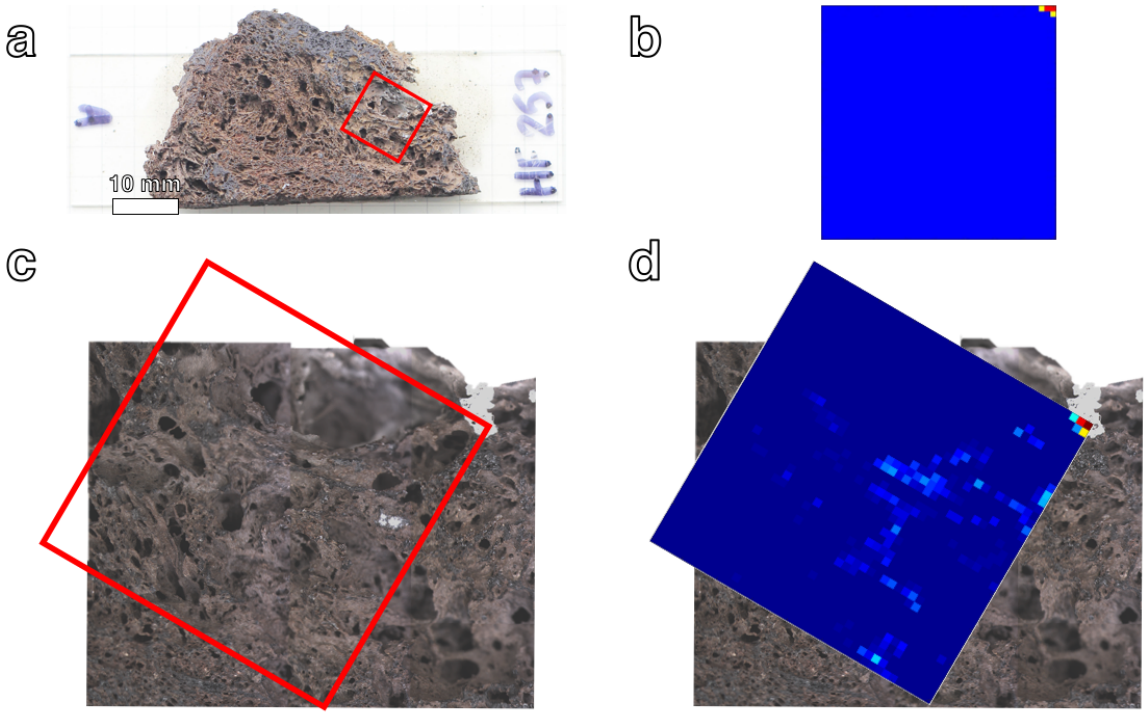

Figure 7.29 LIF results from sample HF257, slide A. [a] Slide A, with scale, showing the location of the LIF map (red box). [b] Absolute-scale comparative map. [c] Composite microscopic image of the surface of the sample, with a red outline (one side = 10 mm) of the mapped area. [d] Relative-scale 1600-point raster map overlain on composite microscope image.

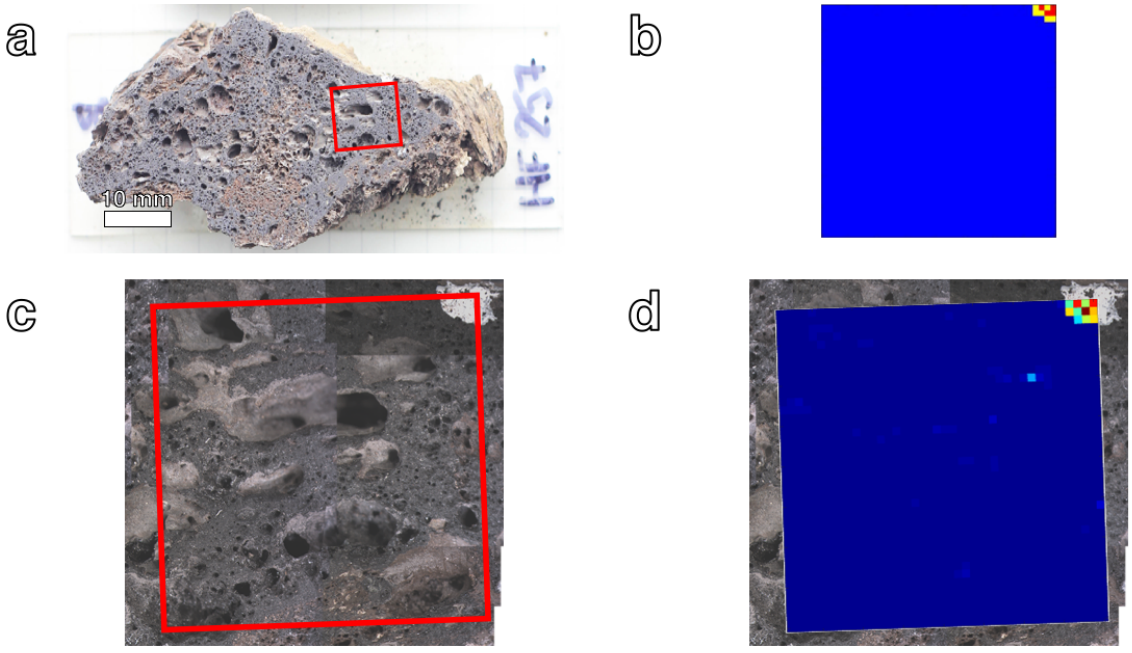

Figure 7.30 LIF results from sample HF257, slide B. [a] Slide B, with scale, showing the location of the LIF map (red box). [b] Absolute-scale comparative map. [c] Composite microscopic image of

the surface of the sample, with a red outline (one side = 10 mm) of the mapped area. [d] Relative-scale 1600-point raster map overlain on composite microscope image.

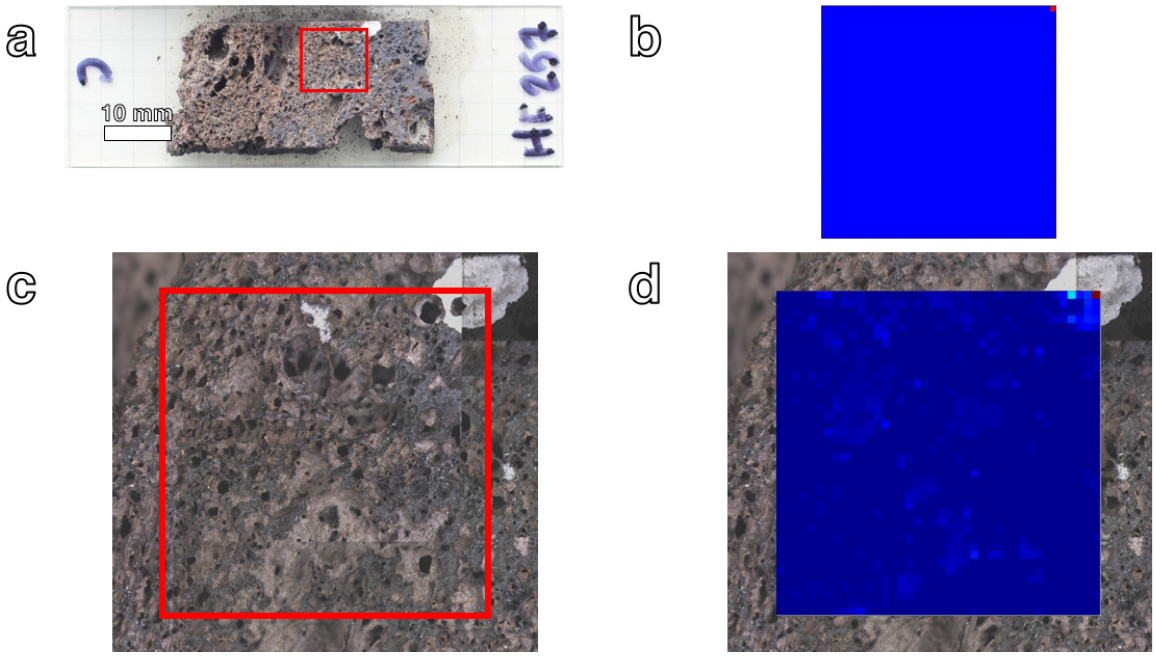

Figure 7.31 LIF results from sample HF257, slide C. [a] Slide C, with scale, showing the location of the LIF map (red box). [b] Absolute-scale comparative map. [c] Composite microscopic image of the surface of the sample, with a red outline (one side = 10 mm) of the mapped area. [d] Relative-scale 1600-point raster map overlain on composite microscope image.

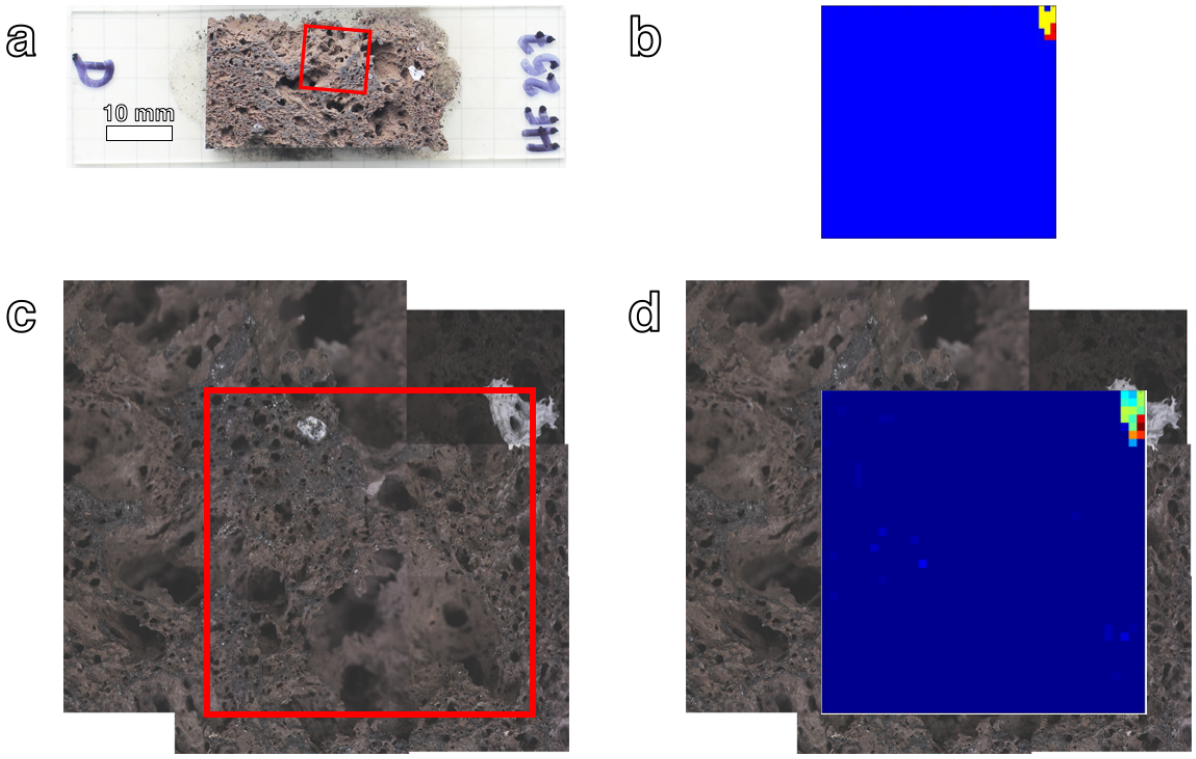

Figure 7.32 LIF results from sample HF257, slide D. [a] Slide D, with scale, showing the location of the LIF map (red box). [b] Absolute-scale comparative map. [c] Composite microscopic image of the surface of the sample, with a red outline (one side = 10 mm) of the mapped area. [d] Relative-scale 1600-point raster map overlain on composite microscope image.

Due to the lack of POIs present in this sample, no SEM analyses were performed.

7.7.2 Porosity results

The pycnometer measurements produced a mean skeletal volume, $V_{skel.rock}$ (based on ten trials of one rock chip) of 0.683 $cm^3 \pm 0.011$ cm^3.

The μCT scanner measurements (fig. 7.33) produced a bulk volume, $V_{bulkrock}$ of 1.353 cm^3.

Therefore, the mean porosity fraction for this sample, φ_{rock}, is 0.495 ± 0.008.

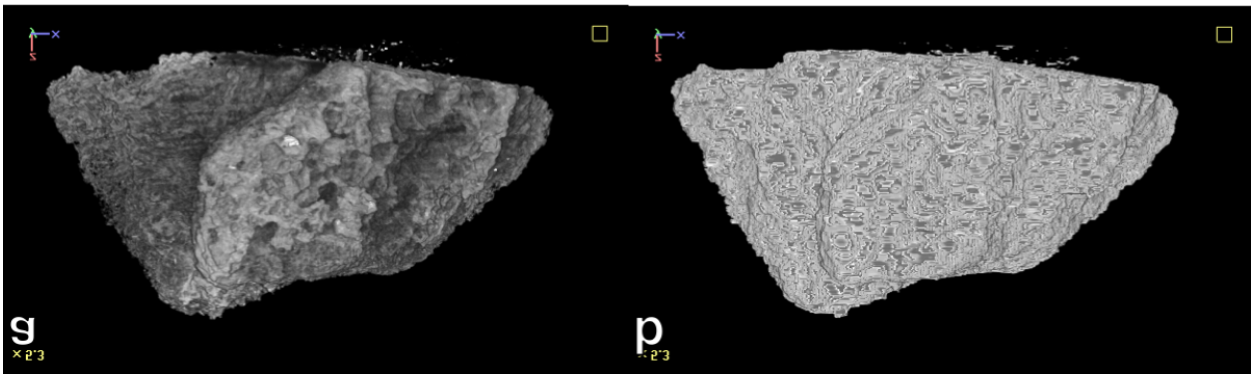

Figure 7.33 [a] The original μCT-generated 3D shape model of the HF257 rock chip.[b] 3D shape model of the same rock chip as [a], post-processing.

7.8 ID2016 – HF256 (Unaltered)

7.8.1 LIF mapping and LIF time-resolved results

Sample HF257 was cut into four slides, with four 1600-point, 1 cm * 1 cm maps produced through LIF mapping. Maps A (fig. 7.34), B (fig. 7.35), and C (fig. 7.36) are all interior maps. Map D (fig. 7.37) was taken near an exposed edge, with one large edge-connected vesicle showing a thin, white surface coating. All maps show a similar homogeneous black colour and size/size distribution of vesicles. None of the sample slides show any vesicle infills. None of the maps had POIs that were investigated further.

While map C showed one pixel that was high intensity, the extremely low-intensity immediate surroundings and lack of any distinct visual features at this pixel's location indicate the likelihood of this pixel being a cosmic ray measurements or noise. The yellow pixel in this absolute-scale intensity map was therefore discounted.

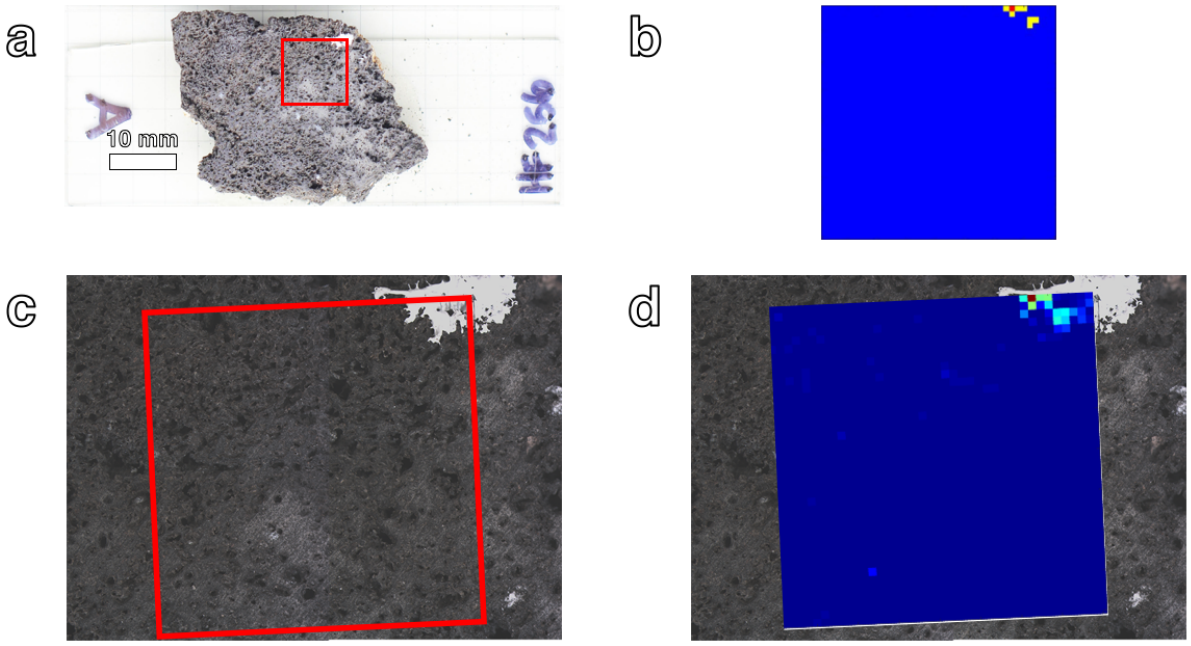

Figure 7.34 LIF results from sample HF256, slide A. [a] Slide A, with scale, showing the location of the LIF map (red box). [b] Absolute-scale comparative map. [c] Composite microscopic image of the surface of the sample, with a red outline (one side = 10 mm) of the mapped area. [d] Relative-scale 1600-point raster map overlain on composite microscope image.

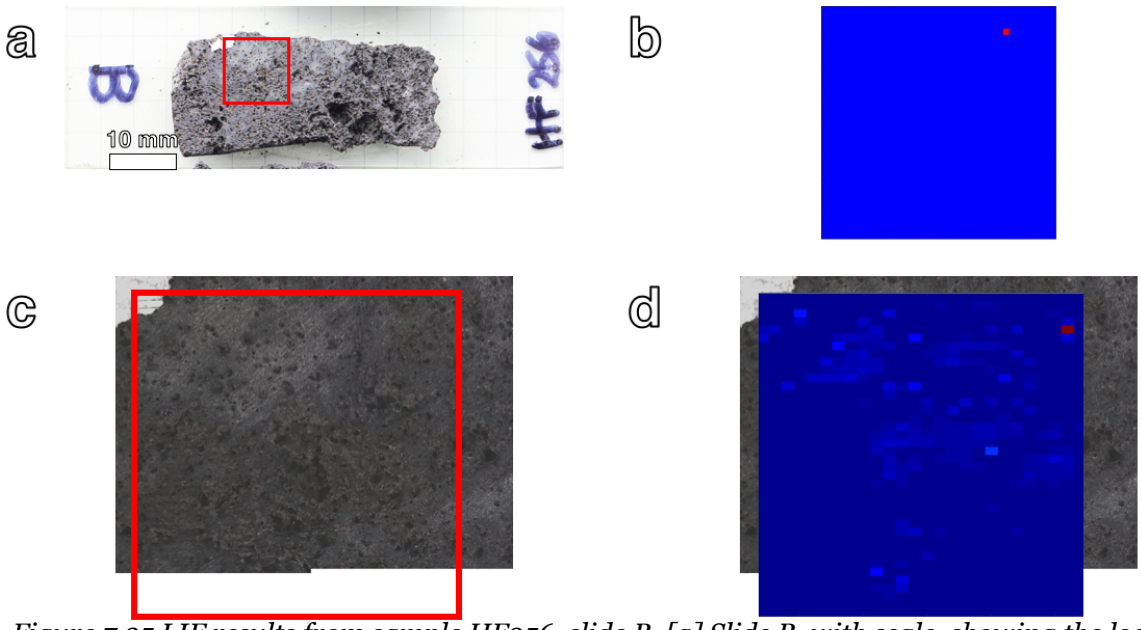

Figure 7.35 LIF results from sample HF256, slide B. [a] Slide B, with scale, showing the location of the LIF map (red box). [b] Absolute-scale comparative map. [c] Composite microscopic image of the surface of the sample, with a red outline (one side = 10 mm) of the mapped area. [d] Relative-scale 1600-point raster map overlain on composite microscope image.

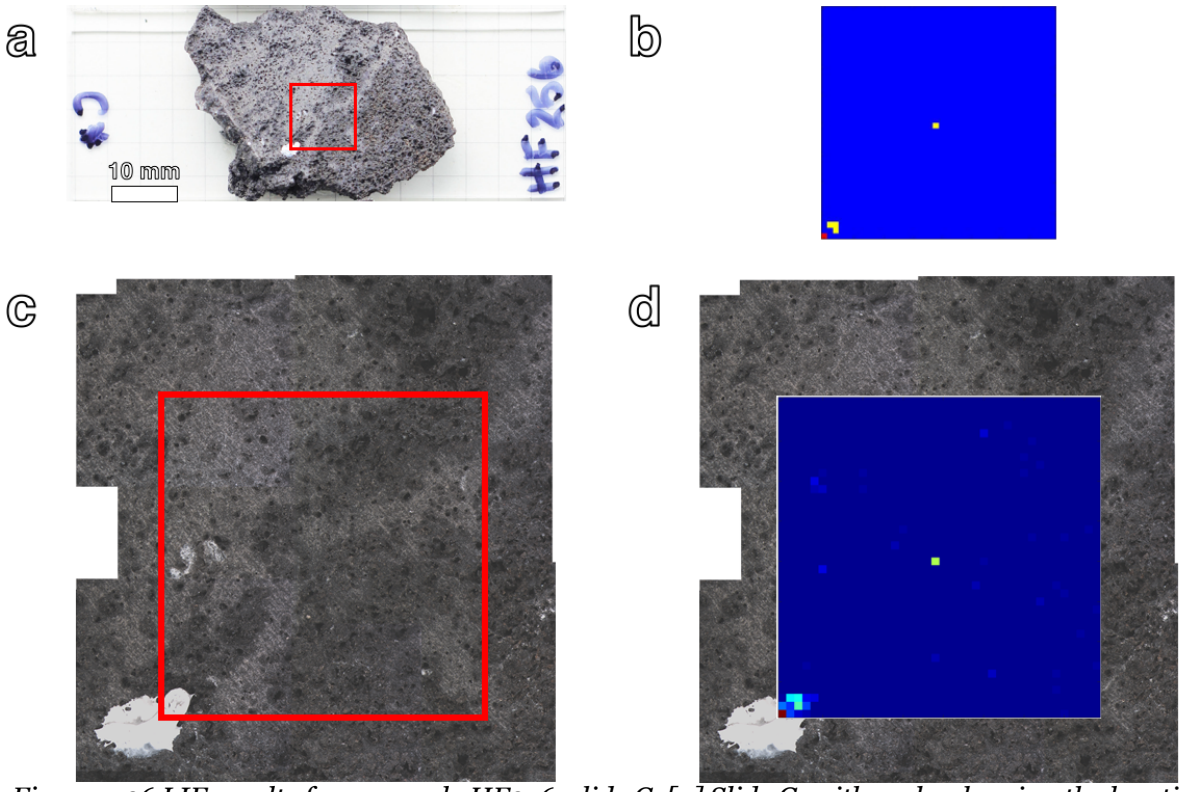

Figure 7.36 LIF results from sample HF256, slide C. [a] Slide C, with scale, showing the location of the LIF map (red box). [b] Absolute-scale comparative map. [c] Composite microscopic image of the surface of the sample, with a red outline (one side = 10 mm) of the mapped area. [d] Relative-scale 1600-point raster map overlain on composite microscope image.

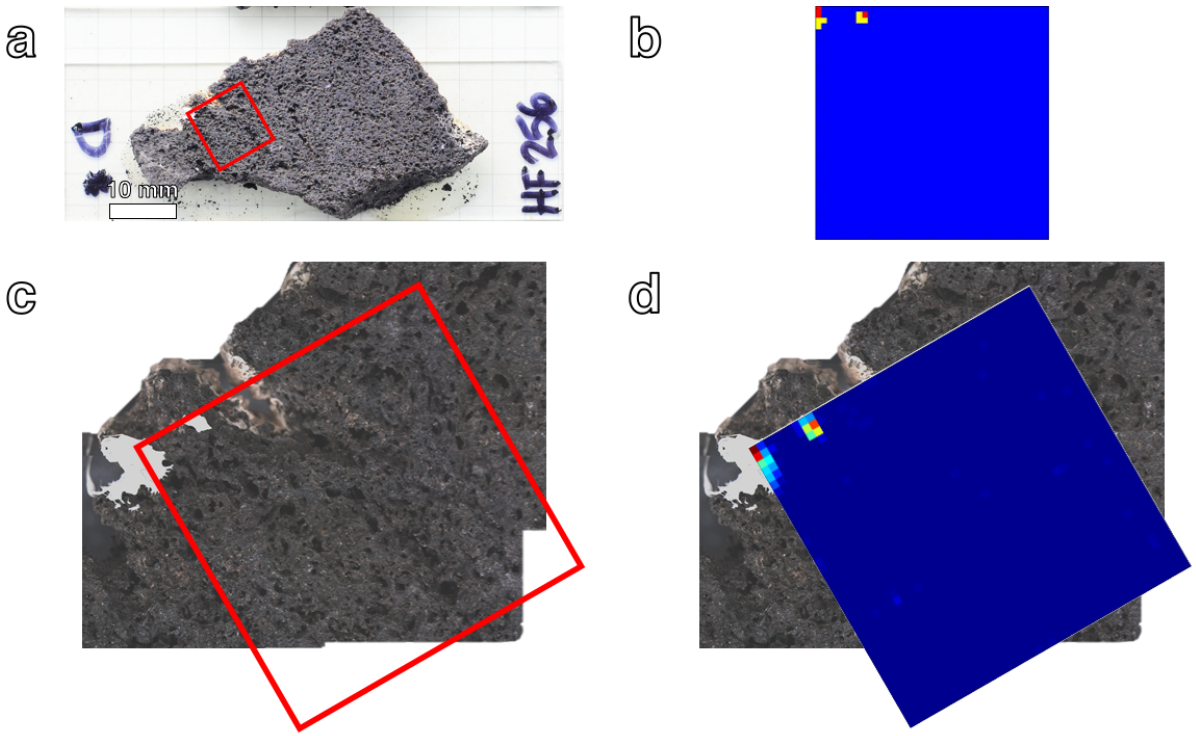

Figure 7.37 LIF results from sample HF256, slide D. [a] Slide D, with scale, showing the location of the LIF map (red box). [b] Absolute-scale comparative map. [c] Composite microscopic image of

the surface of the sample, with a red outline (one side = 10 mm) of the mapped area. [d] Relative-scale 1600-point raster map overlain on composite microscope image.

Due to the lack of POIs present in this sample, no SEM analyses were performed.

7.8.2 Porosity results

The pycnometer measurements produced a mean skeletal volume, $V_{skel.rock}$ (based on ten trials of one rock chip) of 1.502 cm^3 ± 0.012 cm^3.

The μCT scanner measurements (fig. 7.38) produced a bulk volume, $V_{bulkrock}$ of 2.002 cm^3.

Therefore, the mean porosity fraction for this sample, φ_{rock}, is 0.250 ± 0.002.

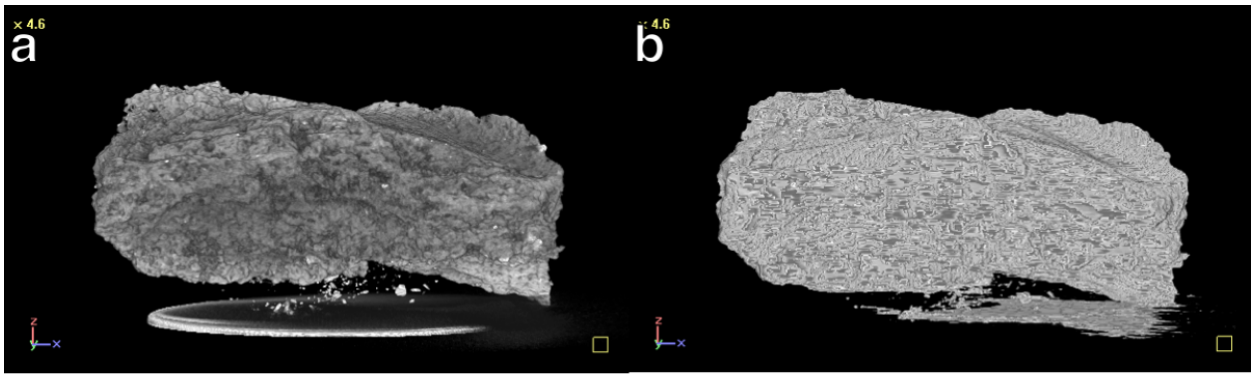

Figure 7.38 [a] The original μCT-generated 3D shape model of the HF256 rock chip. [b] 3D shape model of the same rock chip as [a], post-processing.

7.9 ID2016 – BC317 (Unaltered)

7.9.1 LIF mapping and LIF time-resolved results

Sample BC317 was cut into three slides, with three 1600-point, 1 cm * 1 cm maps produced through LIF mapping. Maps A (fig. 7.39) and B (fig. 7.40) were taken in the sample's interior (tangential to a cut edge), and included a dense, black matrix with some vesicles containing a very thin coating of WCM. Map C (fig. 7.41) was taken near an exposed edge, and included the same dense, black matrix and vesicle sizes/distributions as maps A and B, although more vesicles contained WCM.

POI C1 showed a strong spectral signature with a single broad peak located at approximately 440 nm. This peak reached its maximum intensity at 4.5 ns and decayed within 2.5-3 ns.

While map A showed one pixel that was high intensity, the extremely low-intensity immediate surroundings and lack of any distinct visual features at this pixel's location

indicate the likelihood of this pixel being a cosmic ray measurements or noise. The yellow pixel in this absolute-scale intensity map was therefore discounted. The map B absolute intensity scale showed a total of 2 red pixels and 2 yellow pixels, with a combined approximate area of 1 mm^2, based on the map step size of 0.25 mm. The map C absolute intensity scale showed a total of 15 red pixels and 27 yellow pixels, with a combined approximate area of 10.5 mm^2, based on the map step size of 0.25 mm.

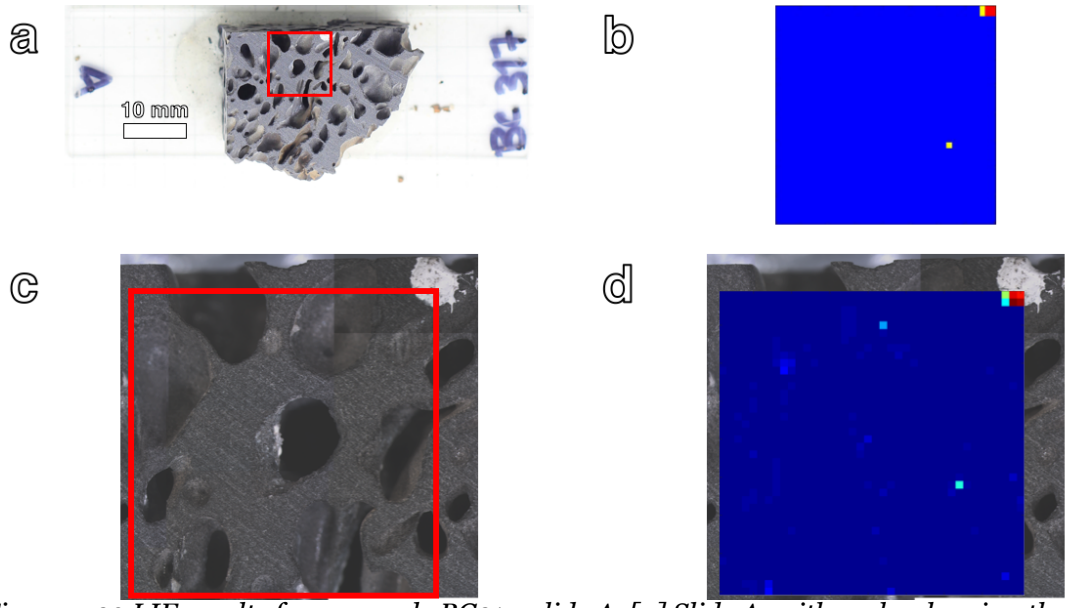

Figure 7.39 LIF results from sample BC317, slide A. [a] Slide A, with scale, showing the location of the LIF map (red box). [b] Absolute-scale comparative map. [c] Composite microscopic image of the surface of the sample, with a red outline (one side = 10 mm) of the mapped area. [d] Relative-scale 1600-point raster map overlain on composite microscope image.

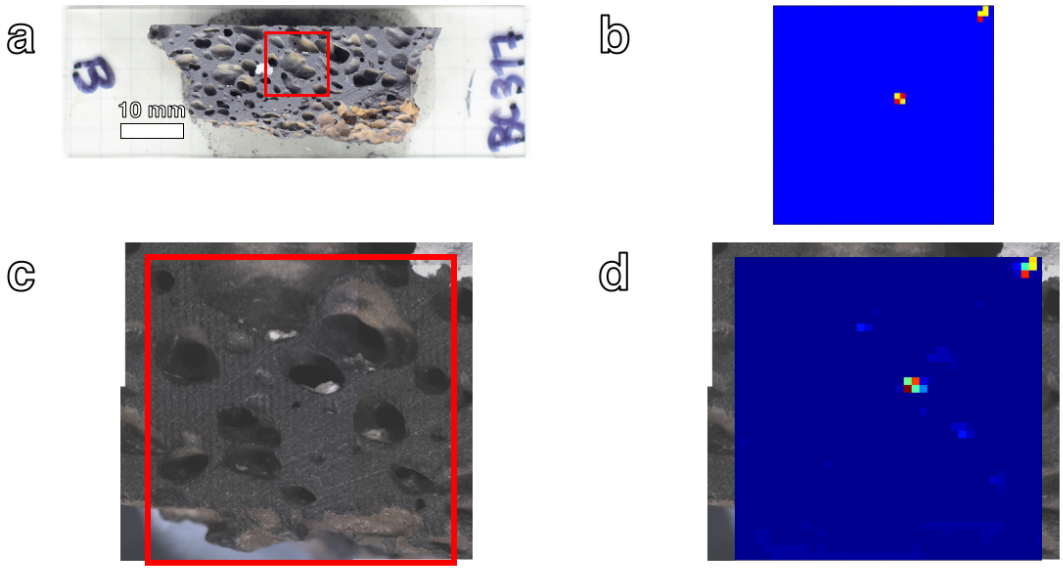

Figure 7.40 LIF results from sample BC317, slide B. [a] Slide B, with scale, showing the location of the LIF map (red box). [b] Absolute-scale comparative map. [c] Composite microscopic image of

the surface of the sample, with a red outline (one side = 10 mm) of the mapped area. [d] Relative-scale 1600-point raster map overlain on composite microscope image.

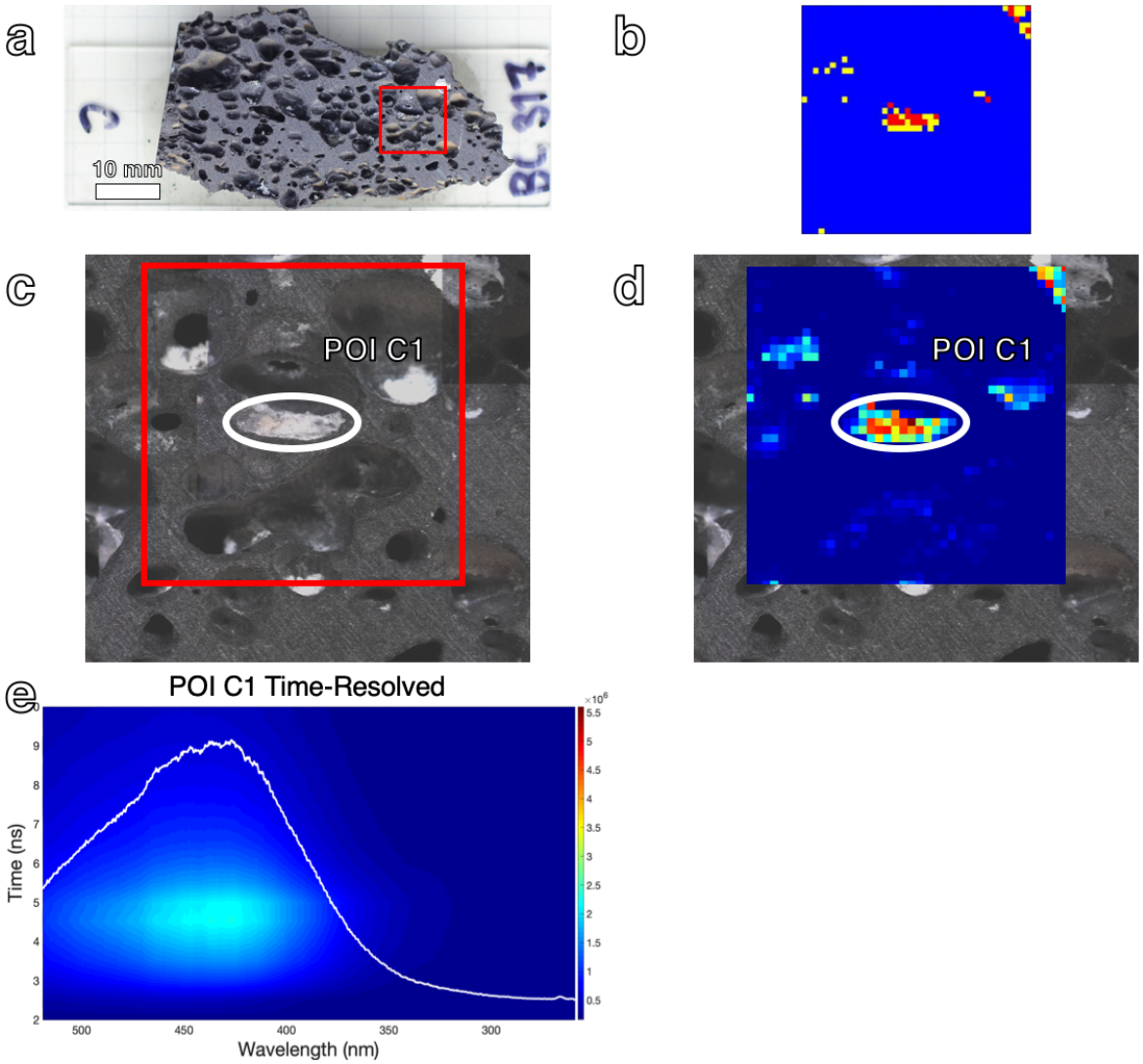

Figure 7.41 LIF results from sample BC317, slide C. [a] Slide C, with scale, showing the location of the LIF map (red box). [b] Absolute-scale comparative map. The large area of red and yellow pixels in the centre were chosen as a POI. [c] Composite microscopic image of the surface of the sample, with a red outline (one side = 10 mm) of the mapped area and identified POI A1 circled in white. [d] Relative-scale 1600-point raster map overlain on composite microscope image, with POI identified. [e] Absolute-scale, time-resolved contour plot of POI A1 with overlain spectra at the time of maximum intensity, t = 4.5 ns.

7.9.2 SEM results

The single POI from this sample was investigated in the SEM, and EDS point analyses were conducted to acquire an approximate elemental quantification, from which minerals could tentatively be identified (table 7.6; fig. 7.42). The minerals calcite (cal), amphibole, olivine (ol), and albite-andesite (ab-and), along with carbon-rich material were identified

in the point analyses. Moderate to high amounts of carbon were measured through multiple points in the large POI, with an average of 15 wt% CO_2 detected in C1-1, 37 wt% CO_2 detected in C1-2, and 30 wt% CO_2 detected in C1-3. C1-2 had some points with 50 - 90 wt% CO_2 and C1-3 had points with 60 – 80 wt% CO_2.

Table 7.6 Example EDS point analysis results and the associated mineral identification. Results are reported in weight percent oxides, normalized. All iron is assumed to be present as FeO.

POI	Mineral	SiO_2	TiO_2	Al_2O_3	FeO	MgO	CaO	Na_2O	K_2O	CO_2
C1-1	Amphibole	52	1	11	15	3	4	2	4	6
C1-1	Olivine	39	1	-	20	29	-	-	-	11
C1-1	Albite-andesine	51	1	19	3	-	8	4	2	12
C1-2	Calcite	2	-	-	-	2	56	-	-	40
C1-2	Carbon-rich material	2	-	1	-	3	14	1	-	19

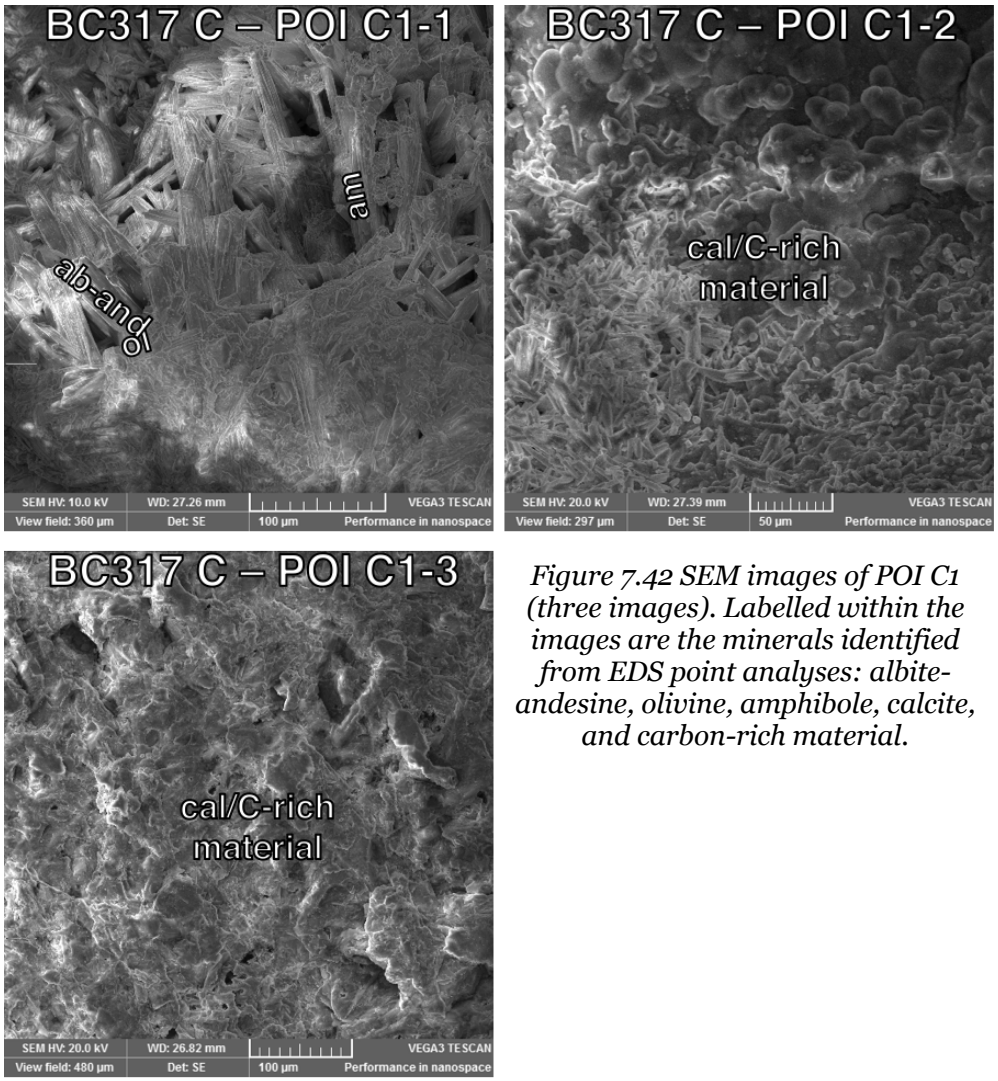

Figure 7.42 SEM images of POI C1 (three images). Labelled within the images are the minerals identified from EDS point analyses: albite-andesine, olivine, amphibole, calcite, and carbon-rich material.

7.9.3 Porosity results

The pycnometer measurements produced a mean skeletal volume, $V_{skel.rock}$ (based on ten trials of one rock chip) of 0.737 cm^3 ± 0.011 cm^3.

The μCT scanner measurements (fig. 7.43) produced a bulk volume, $V_{bulkrock}$ of 0.988 cm^3.

Therefore, the mean porosity fraction for this sample, φ_{rock}, is 0.254 ± 0.004.

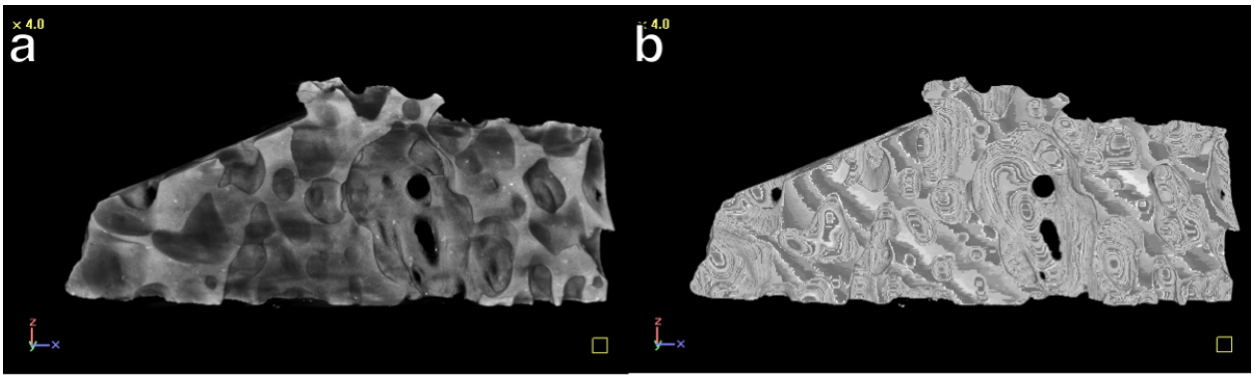

Figure 7.43 [a] The original μCT-generated 3D shape model of the BC317 rock chip. [b] 3D shape model of the same rock chip as [a], post-processing.

7.10 Summary of Results

Table 7.7 Physical and geological properties from all samples analyzed.

					Physical and Geological Properties						
Sample	**Map**	**Map location**	**POI**	**POI location**	**Alteration Style**	**Colour**	**Approx. median vesicle diameter**	**Approx. vesicle size range (min/max) (mm)**	**Porosity fraction**	**EDS minerals**	**EDS average C component (wt% CO_2)**
MU100074	A	Edge	A1	WCM-filled vesicle	Active fumarole	Orange, red-brown, with some black mx	2.5	0.5/4	0.4952	px, prg, chl, glass, am	9.93
			A2	WCM-filled vesicle						zeo, clay, glass	10.13
	B	Edge	B1	WCM-filled vesicle						fo, opx, clay, zeo, chl	10.00
			B2	WCM-filled vesicle						clay, zeo, ab-and, am	12.66
	E	Interior	-	-						-	-
MU100089	A	Edge	A1	Part of WCM-filled vesicle	Active fumarole	Black-grey	2.5	0.5/4.5	0.3807	lab-an, cpx, am, hul/stb, high-C material	12.83
	B	Interior	B1	Part of WCM-filled vesicle						hul/stb, zeo, clay	6.88
			B2	On WCM, edge of vesicle							
	C	Edge	C1	On WCM, edge of vesicle						chl, cpx, clay, prg, lab-an	5.83
			C2	On WCM, edge of vesicle						hul/stb	13.23
MU100620	A	Edge	A1	WCM-filled vesicle	Relict fumarole	Black-grey	3	1/7.5	0.3655	glass, high-C material	40.00
			A2	WCM-filled vesicle						lab-an, opx, am, clay?, high-C material	16.48
			A3	WCM-filled vesicle						am, glass, high-C material	57.82
			A4	WCM-filled vesicle						opx, chl, high-C material	17.21
	B	Edge	B1	Part of WCM-filled vesicle						glass/mix	7.65

MU100110	C	Interior	B2	Part of WCM-filled vesicle	Unaltered	Black	2.5	2/3	0.2840	high-C material, glass, am	34.45
			C1	On WCM, edge of vesicle						glass, high-C material	39.82
			C2	On WCM, edge of vesicle						glass/mix, am, chl, plg	14.01
	A	Edge	A1	On WCM, edge of vesicle						clay, glass/mix, am, chl	10.40
			A2	On WCM, edge of vesicle						glass/mix, am	14.26
HF437	A	Interior	A1	Within streak of orange mx	High-T alteration	Brown, black, red, orange	1	0.5/3	0.5715	glass/mix, zeo, high-C material	43.12
			A2	Within streak of orange mx						mnt, ill, clay, high-C material, fa, am	28.22
	B	Interior	-	-						-	-
	C	Edge	-	-						-	-
	D	Edge	-	-						-	-
BC459	A	Edge	-	-	Mod.- high-T alteration	Tan, yellow, brown, red, black	2	1/7	0.3715	-	-
	C	Interior	-	-						-	-
	D	Edge	-	-						-	-
HF257	A	Edge	-	-	Low-T alteration	Brown, black	1	0.5/5	0.4950	-	-
	B	Interior	-	-						-	-
	C	Interior	-	-						-	-
	D	Edge	-	-						-	-
HF256	A	Interior	-	-	Unaltered	Black	0.5	0/1	0.2496	-	-
	B	Interior	-	-						-	-
	C	Interior	-	-						-	-
	D	Edge	-	-						-	-
BC317	A	Interior	-	-	Unaltered	Black, dark brown	3	1/5	0.2543	-	-
	B	Interior	-	-						-	-
	C	Edge	C1	WCM-filled vesicle						cal, am, ab-and, ol, high-C material	27.34

Table 7.8 Fluorescence properties from all samples analyzed.

					Fluorescence properties							
Sample	**Map**	**Map location**	**POI**	**POI location**	**No. of red pixels**	**Area of red pixels (mm²)**	**No. of yellow pixels**	**Area of yellow pixels (mm²)**	**Total area of red and yellow pixels (mm²)**	**TR max int. (AU *10⁶)**	**TR short wl (nm)**	**TR long wl (nm)**
MU100074	A	Edge	A1	WCM-filled vesicle	7	1.75	7	1.75	3.50	2.6028	425	-
			A2	WCM-filled vesicle						5.1404	455	-
	B	Edge	B1	WCM-filled vesicle	1	0.40	3	1.20	1.60	3.3431	425	-
			B2	WCM-filled vesicle						2.2123	425	-
	E	Interior	-	-	-	-	-	-	-	-	-	-
MU100089	A	Edge	A1	Part of WCM-filled vesicle	1	0.25	5	1.25	1.50	5.5294	430, 300	-
	B	Interior	B1	Part of WCM-filled vesicle	7	1.75	39	9.75	11.50	1.0658	420	-
			B2	On WCM, edge of vesicle						1.256	-	350
	C	Edge	C1	On WCM, edge of vesicle	1	0.25	8	2.00	2.25	2.6984	425, 300	-
			C2	On WCM, edge of vesicle						4.8677	425, 300	-
MU100620	A	Edge	A1	WCM-filled vesicle	67	16.75	103	25.75	42.50	2.7081	440	-
			A2	WCM-filled vesicle						4.0095	430	-
			A3	WCM-filled vesicle						3.4166	430	350
			A4	WCM-filled vesicle						1.5694	440	340
	B	Edge	B1	Part of WCM-filled vesicle	2	0.50	23	5.75	6.25	0.4529	440	-
			B2	Part of WCM-filled vesicle						0.9129	440	350
	C	Interior	C1	On WCM, edge of vesicle	12	3.00	47	11.75	14.75	2.9554	455, 445	350
			C2	On WCM, edge of vesicle						4.2240	430	-
MU100110	A	Edge	A1	On WCM, edge of vesicle	3	1.50	5	2.50	4.00	0.6874	430	350
			A2	On WCM, edge of vesicle						0.5770	430	350
HF437	A	Interior	A1	Within streak of orange mx	2	0.50	-	-	0.50	0.5255	430	-
			A2	Within streak of orange mx						0.2675	440	-
	B	Interior	-	-	-	-	-	-	-	-	-	-
	C	Edge	-	-	-	-	-	-	-	-	-	-
	D	Edge	-	-	-	-	-	-	-	-	-	-
BC459	A	Edge	-	-	-	-	-	-	-	-	-	-
	C	Interior	-	-	-	-	-	-	-	-	-	-
	D	Edge	-	-	-	-	-	-	-	-	-	-
HF257	A	Edge	-	-	-	-	-	-	-	-	-	-
	B	Interior	-	-	-	-	-	-	-	-	-	-
	C	Interior	-	-	-	-	-	-	-	-	-	-
	D	Edge	-	-	-	-	-	-	-	-	-	-

HF256	A	Interior	-	-	-	-	-	-	-	-	-	-
	B	Interior	-	-	-	-	-	-	-	-	-	-
	C	Interior	-	-	-	-	-	-	-	-	-	-
	D	Edge	-	-	-	-	-	-	-	-	-	-
BC317	A	Interior	-	-	-	-	-	-	-	-	-	-
	B	Interior	-	-	2	0.50	2	0.50	1.00	-	-	-
	C	Edge	C1	WCM-filled vesicle	15	3.75	27	6.75	10.50	2.2350	430	-

8 Discussion

There are many challenges inherent in analyzing these data, as so many of the properties measured are qualitative, rather than quantitative. However, some basic comparisons can be drawn and conclusions made. Although the following observations do not pass statistical scrutiny due to the small sample sizes present, they can provide important insights about the relationships between fluorescent properties and geological/physical properties of the samples.

During the analyses of the results of this research, the following hypotheses were established to be accepted or rejected:

1. Fumarole-derived samples would be the most likely to show evidence of organic material, due to the ready availability of chemical energy for microbial metabolism in these rocks. This would be followed by high- to low-temperature altered rocks, with unaltered rocks providing the least evidence.
2. High fluorescence activity in a sample would correlate to higher concentrations of carbon-rich material, due to the fluorescent characteristics of organic molecules.
3. There is some relationship between the presence of fluorescing material in a sample and its position within the sample.
4. There is some relationship between the porosity of a sample and the presence of carbonaceous and/or fluorescent material, as a more porous sample would provide greater surface area for organics to adhere to.

8.1 Hypothesis 1: Relationships between Alteration Style and Fluorescent/Organic Properties

A note about the sample type groupings: although both HI2016 and ID2016 had "unaltered" as a sample type, I chose to separate these two types in the overall comparative analyses. This is due to the dramatically different environments the Idaho and Hawai'i samples have been subjected to, and also accounts for the different lava geochemistries of the two locations.

8.1.1 *Alteration style and carbon component*

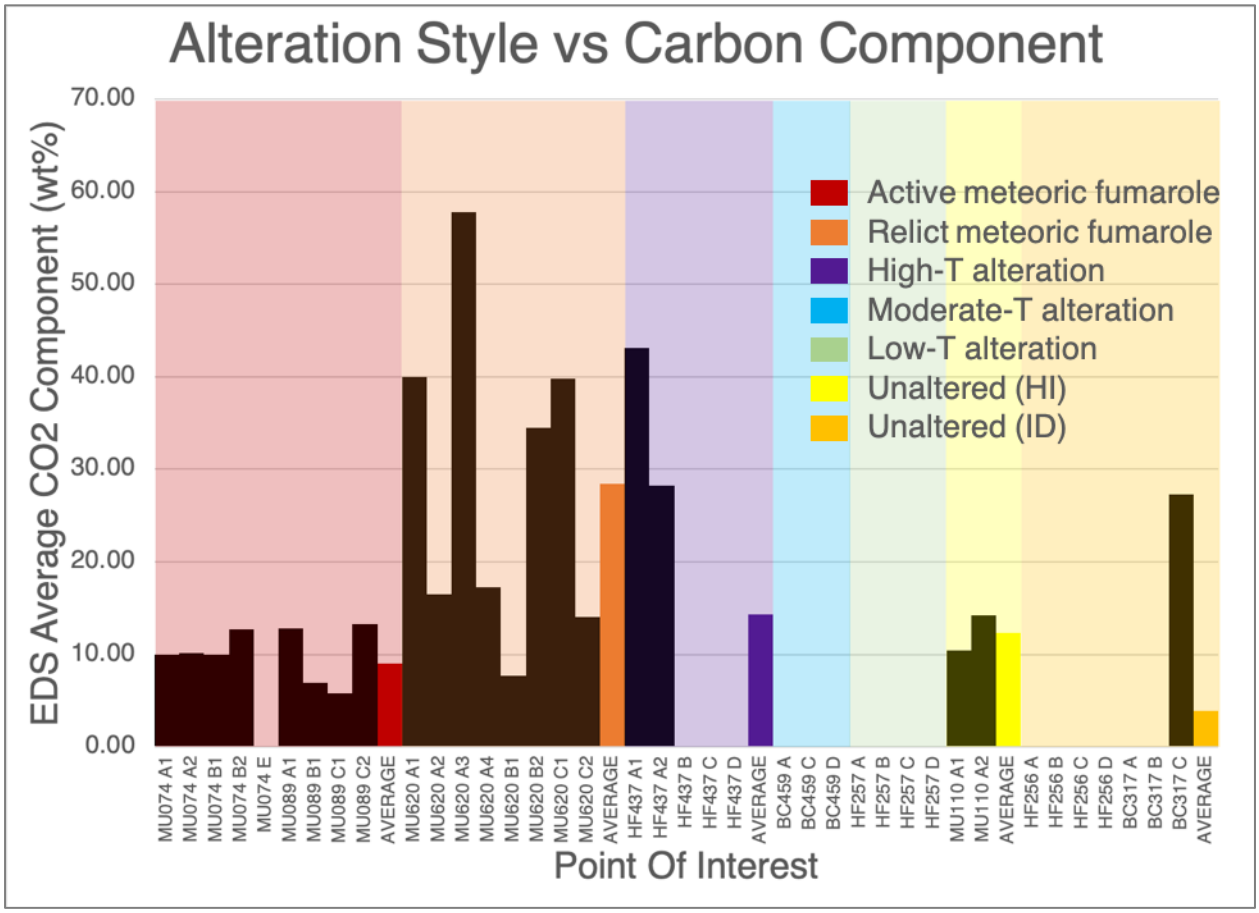

Figure 8.1 Chart comparing the alteration style (as described in Tables 5.1 and 5.2) of a sample and the average (mean) weight percent of carbon dioxide measured in each POI by the EDS. Black bars represent the average measurement from each individual POI, while coloured bars represent the overall average for that sample type. Moderate-T alteration and Low-T alteration, from the ID2016 suite, both had no POIs measured, so are not represented in the EDS measurements.

Figure 8.1 shows the alteration style of a sample compared to the carbon dioxide component of its POIs as measured by the EDS. The single relict fumarole sample from HI2016, sample MU100620, had the highest measured carbon component overall, at 28.43 wt% CO_2 from eight POIs. The lowest average carbon component of those measured came from the ID2016 unaltered samples, with an overall mean of 3.91 wt% CO_2 from seven POIs; although the single POI measured in this group, BC317 C1, had a relatively high CO_2 value of 27.34 wt% on average.

8.1.2 *Alteration style and fluorescent pixel counts*

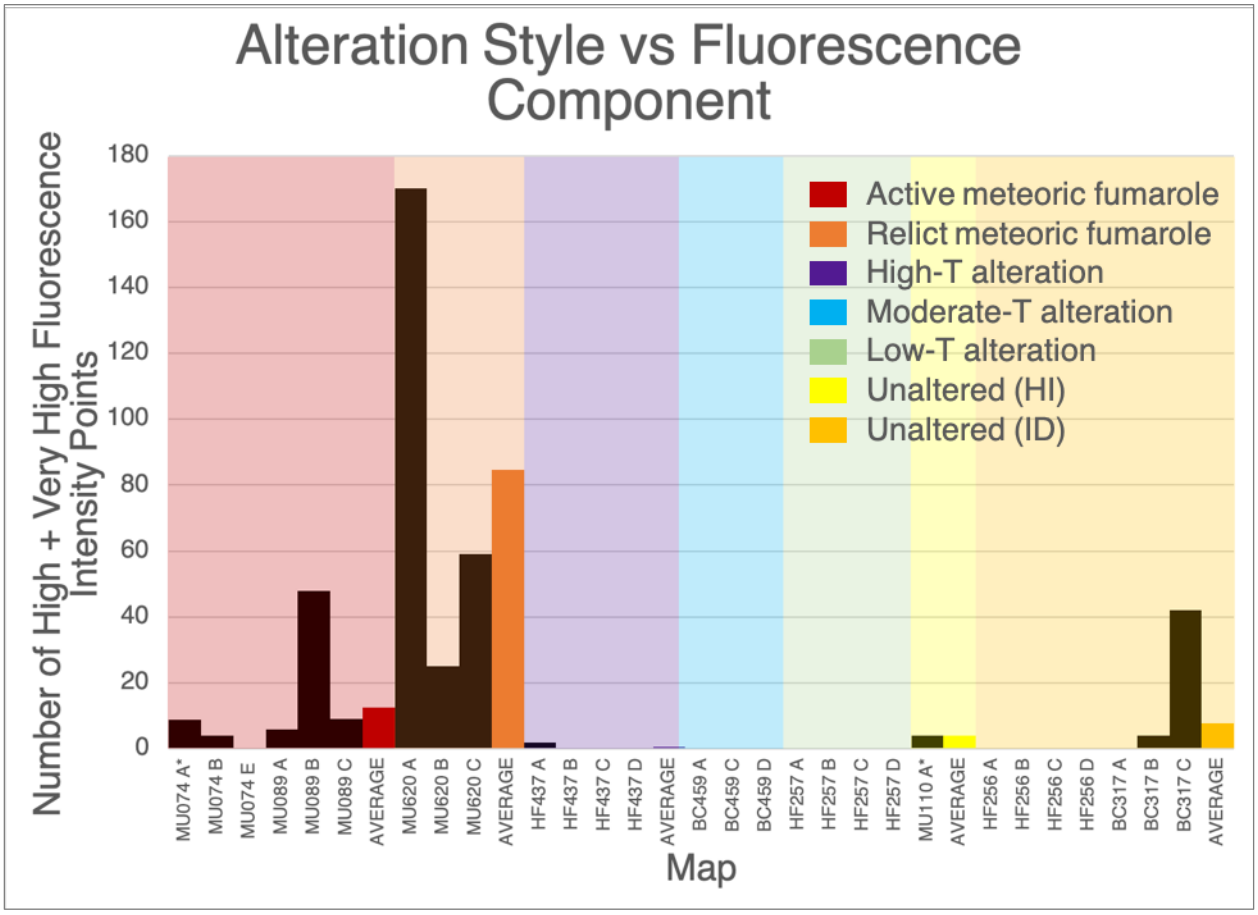

Figure 8.2 Chart comparing the alteration style of a sample and the number of high or very high fluorescence intensity points measured in each map. Black bars represent the number of red and yellow pixels measured in each map, while coloured bars represent the overall average for that sample type.

In Figure 8.2, the average number of high and very high fluorescence pixels in each LIF map is compared to the alteration style of the sample. The relict fumarole sample MU100620 again had the highest mean number of pixels at 84.7, by a large margin compared to the second- and third-highest (active fumarole and unaltered Idaho samples, respectively).

The combining together of high and very high fluorescence pixels into one number reduces the resolution of this dataset, which accounts for one unique source of error. Another source is the pixel/step size for two of the maps: MU100074 A, and MU100110 A. MU100074 A had a step size of 0.4 mm (compared to 0.25 mm for the rest of the maps), so the total number of fluorescent pixels in the map was divided by 1.6 to represent this size difference. Similarly, MU100110 A's pixel size of 0.5 mm necessitated its total pixel

count being divided by 2. While it is possible that a 1600-point map on each of these slides would reveal an equivalent fluorescent area to the lower-resolution maps presented here, it is impossible to know for certain.

8.1.3 Alteration style and maximum fluorescence intensity

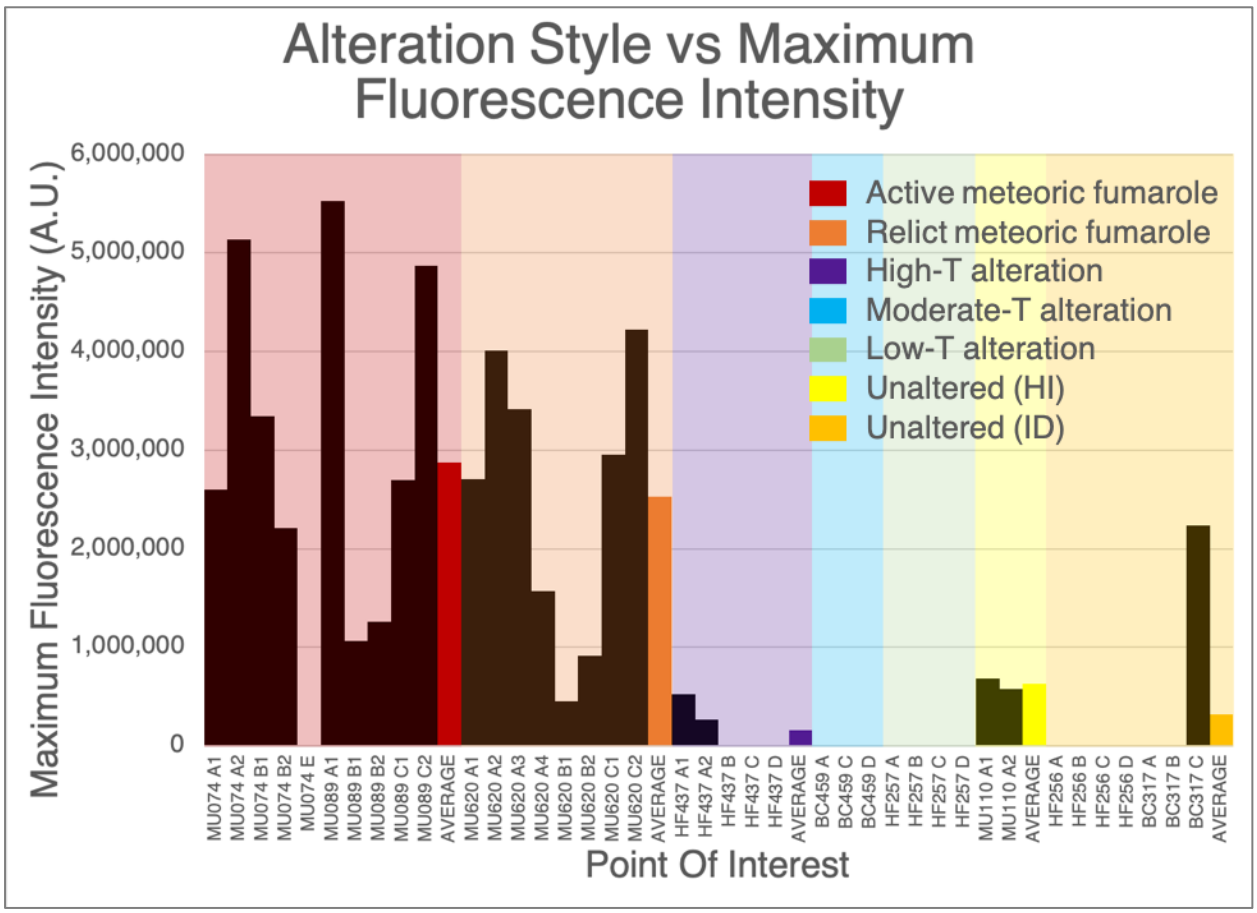

Figure 8.3 Chart comparing the alteration style of a sample and the average maximum fluorescence intensity measured in each POI during time-resolved measurements (in arbitrary units). Black bars represent the maximum measurement from each individual POI, while coloured bars represent the overall average (mean) for that sample type.

Figure 8.3 illustrates the maximum fluorescence intensity of each POI measured during time-resolved analyses. The active meteoric fumarole samples from HI2016, MU100074 and MU100089, showed on average the highest maximum intensity value of 3.19×10^6. Again, with no POIs to measure, the moderate- and low-T alteration samples from ID2016 automatically had the lowest values. Of those POIs actually measured, the high-T alteration ID2016 sample HF437 showed the lowest maximum intensity. A source of error may be that a single TR measurement is not fully representative of the POI as a whole, especially if the POI covers a larger area (e.g. POI BC317 C1).

8.1.4 Alteration style conclusions

Table 8.1 Rankings of alteration styles compared to the organo-fluorescent measurements illustrated above: weight percent carbon dioxide in each POI, fluorescent pixel counts per map, and maximum TR fluorescence intensity per POI. An additional column provides a comparison of the average biomass of each HI2016 sample type (Cockell et al., 2019) to the properties measured in this research.

Alteration Style	**Rank: wt% CO_2 per POI**	**Rank: red/ yellow pixel counts per map**	**Rank: max TR intensity per POI**	***Overall ranking***	***Comparison to biomass data from Cockell et al. (2019)***
Active meteoric fumarole	4	2	1	*2*	*3*
Relict meteoric fumarole	1	1	2	*1*	*1*
High-T alteration	2	5	5	*5*	*N/D*
Moderate-T alteration	6	6	6	*6*	*N/D*
Low-T alteration	6	6	6	*6*	*N/D*
Unaltered (HI)	3	4	3	*4*	*2*
Unaltered (ID)	5	3	4	*3*	*N/D*

Based on the comparison of all of the organo-fluorescent measurements and alteration styles demonstrated in Table 8.1, we can see that the relict meteoric fumarole and active meteoric fumarole samples, both from the HI2016 suite, are most likely to contain some organic species. This would support my first hypothesis: that fumaroles, as sites of hydrothermal activity and sources of chemical energy, would be more likely to host microbial communities than unaltered rocks.

However, this support does not extend to the ID2016 samples. Whilst the high-temperature altered ID2016 sample did show some fluorescent and carbon markers, it was ranked last out of those measured, and the other two altered ID2016 samples showed no fluorescent or carbon markers at all. Instead, the unaltered ID2016 sample BC317 showed the third-highest evidence of organic species overall, followed by the unaltered HI2016 sample MU100110.

The study conducted by Cockell et al. (2019) examining the biodiversity of the BASALT samples included in its supplementary data the estimated biomass of these samples, in cells per gram of dry weight. The data for their replicates of my HI2016

samples MU100074, MU100089, MU100620, and MU100110 were averaged based on sample alteration type, and the rankings from highest to lowest biomass were included in Table 8.1. The relict fumarole sample replicates showed the highest estimated biomass, which agrees with the results gathered here for MU100620.

Interestingly, the estimated biomass from the MU100110 replicate was almost twice as high as the amount in the active fumarole samples, and very close to the amount in the relict fumarole sample. Compared to the relatively low carbon and fluorescent components measured in MU100110, this would indicate that the biomass of this rock is distributed differently than it may be in the other sample types. Considering the relative homogeneity of MU100110 in terms of vesicle size and distribution of WCM, it is possible that biological material is homogeneously distributed through the rock, rather than concentrated in smaller areas as could be indicated by the data from the active and relict fumarole samples.

The samples given a biomass estimate in Cockell et al. did not include replicates of my ID2016 samples, so no direct comparisons can be made.

8.2 Hypothesis 2: Relationship between Organic and Fluorescent Properties

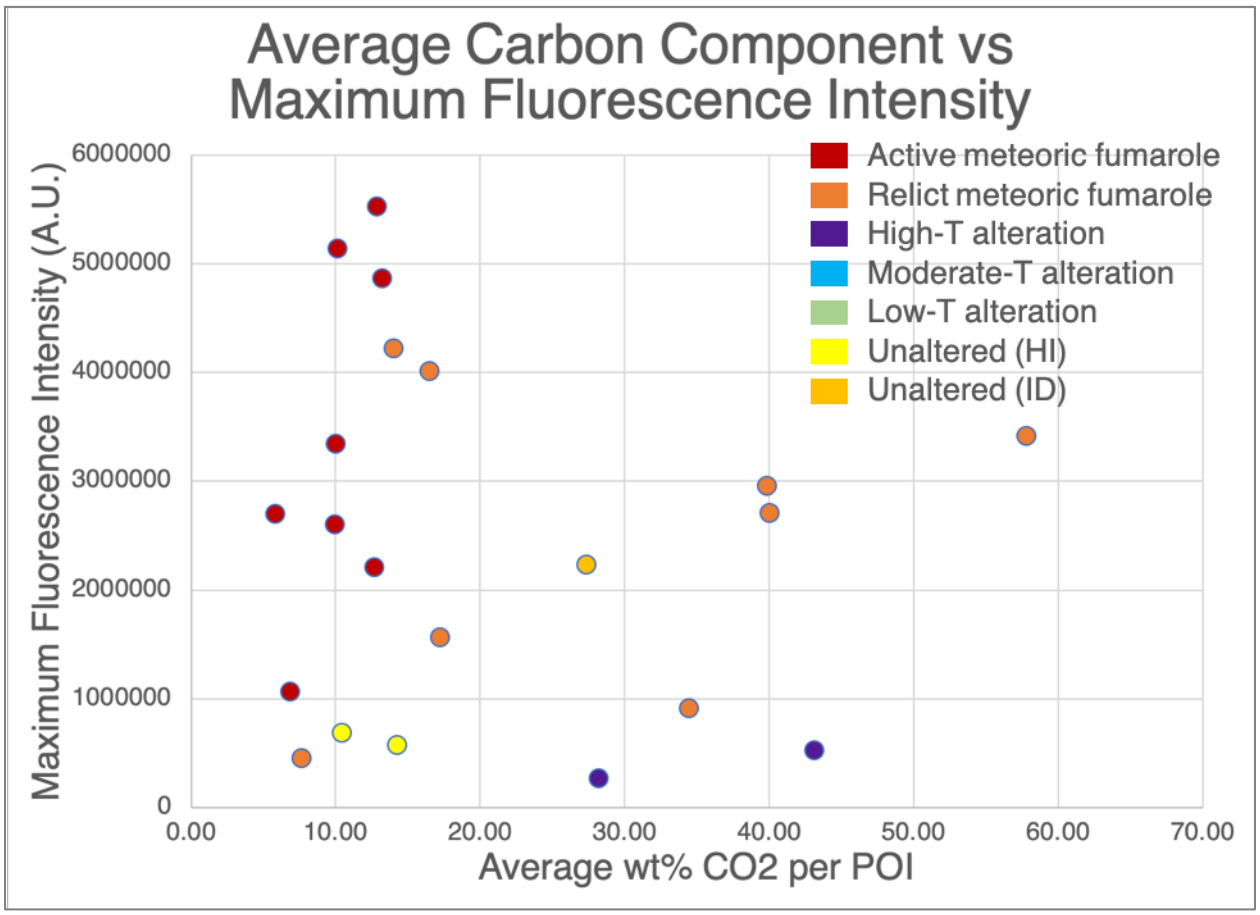

Figure 8.4 Plot of average (mean) weight percent of carbon dioxide measured by the EDS in each POI, against the maximum TR fluorescence intensity measured at each POI.

In Figure 8.4, the carbon component of each POI is compared with the maximum time-resolved fluorescence intensity of that POI. This figure clearly shows that there is basically no relationship between the average amount of carbon in a POI and the maximum fluorescence intensity it exhibits, with the exception of one sample (MU100620). Even a second analysis, comparing the maximum wt% CO_2 detected at each POI to the maximum fluorescence (fig. 8.5) shows a similar lack of correlation. Therefore, my second hypothesis is not supported.

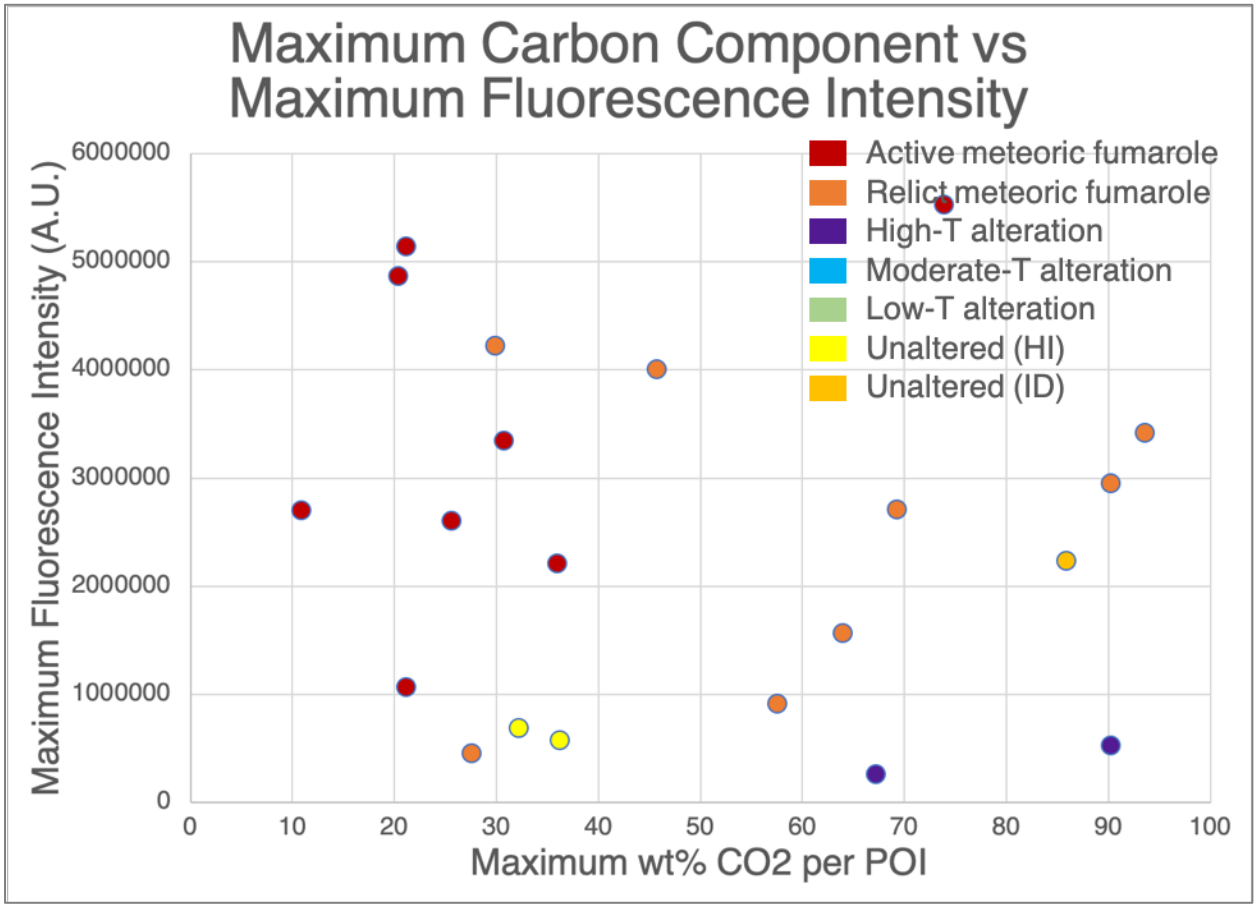

Figure 8.5 Plot of maximum weight percent of carbon dioxide measured by the EDS in each POI, against the maximum TR fluorescence intensity measured at each POI.

More analyses of the POIs, including taking multiple time-resolved measurements within each POI to get a larger point sample size similar to EDS analyses, could potentially reconcile these data to support the second hypothesis. Furthermore, it is important to consider the reliability of EDS to measure light elements such as carbon (Newbury, 2009), as well as the previously-mentioned errors associated with EDS analyses of my samples.

8.3 Hypothesis 3: Relationship between Fluorescing Material and Location

Based on the data in Table 7.8 comparing the location of a LIF map (edge or interior) with the amount of fluorescing pixels in the map, there is no relationship between these two properties. Nonetheless, Table 7.8 does show that POIs are almost always associated with the presence of WCM either coating or completely filling a vesicle (the exception is HF437), although not all WCM is fluorescent enough to be a POI.

8.4 Hypothesis 4: Relationships between Porosity and Fluorescent/Organic Properties

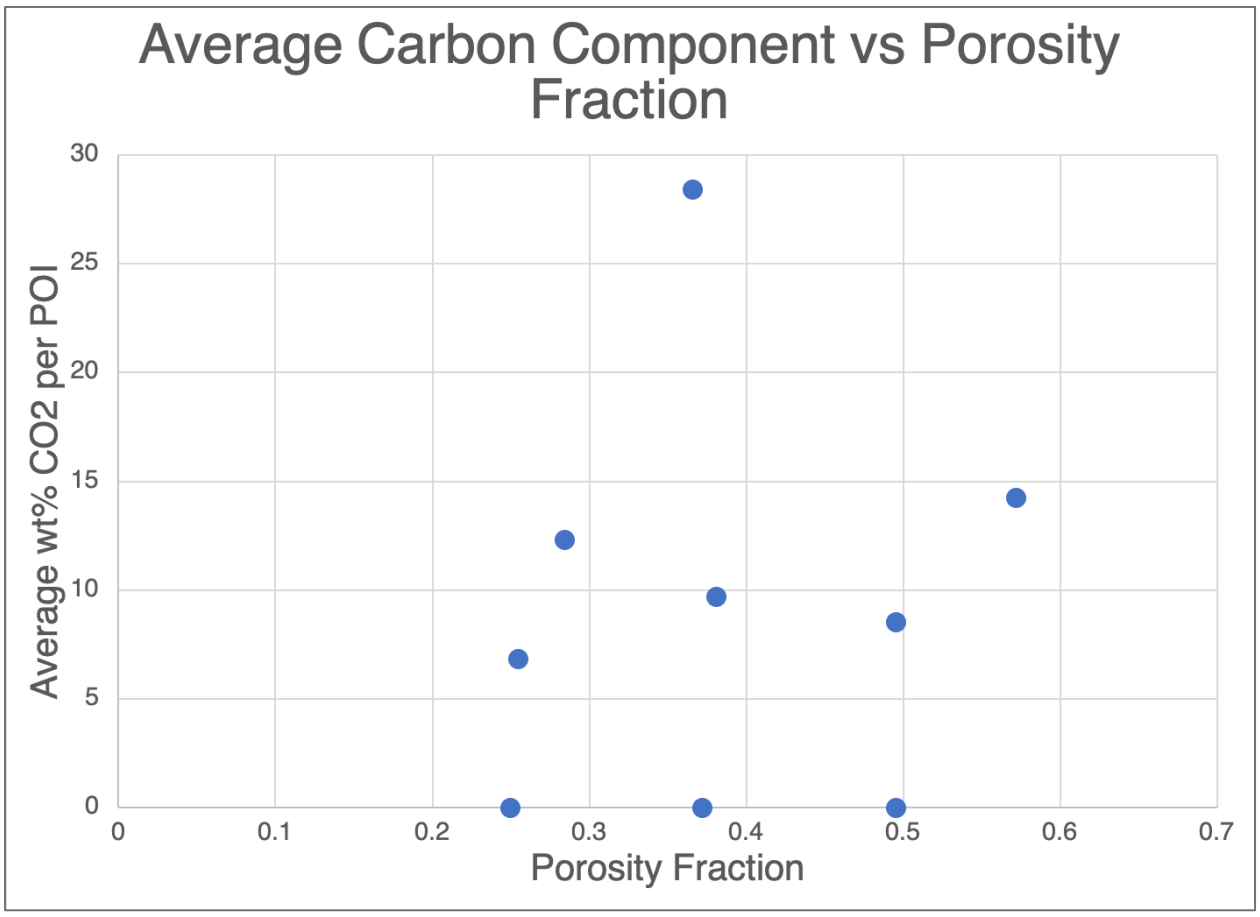

Figure 8.6 Plot of porosity fraction of each sample against the mean wt% CO_2 measured from all the POIs in each sample.

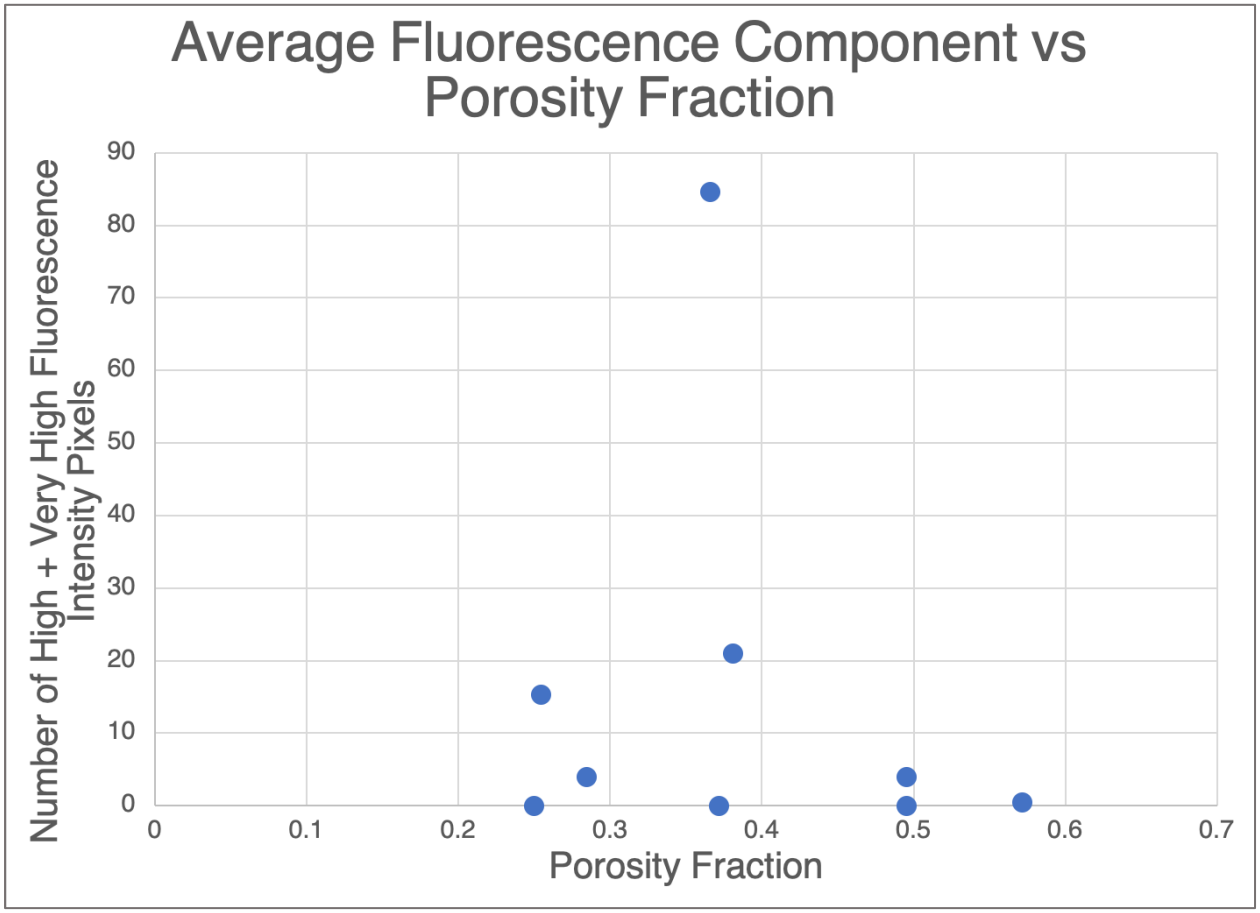

Figure 8.7 Plot of porosity fraction of each sample against the mean number of high or very high fluorescence intensity pixels measured in all the maps from each sample.

Figures 8.6 and 8.7 show that there is no clear relationship between the porosity of a sample and the fluorescent or organic properties it shows. This would appear to disagree with my fourth hypothesis. The porosity measurements taken in this study do not also account for permeability (i.e., the connectivity of the pore spaces within the rock, allowing for fluid to flow through the rock), a related but not directly equivalent property. It is possible that different permeabilities may affect the distribution of organic or fluorescent material, as it would allow for movement of material between pore spaces.

D(

8.5 Summary of hypotheses

My first hypothesis, that the high-temperature or fumarolic alteration of a sample will have an effect on the fluorescent and carbon-rich material found in the sample, is supported by the HI2016 results but not supported by the ID2016 results.

My second hypothesis, that the maximum time-resolved fluorescence intensity detected at a POI is related to the amount of carbon measured by the EDS at that same POI, is unsupported.

My third hypothesis, that there is some relationship between the presence of fluorescing material in a sample and its location within the sample, is both supported and unsupported by the evidence. There is no preference for fluorescent material to be found near a sample's exposed edge or its interior, but there is a strong preference for fluorescent material to be associated with WCM in sample vesicles.

My fourth hypothesis, that there is a relationship between the porosity of a sample and the presence of carbonaceous or fluorescent material, is unsupported.

8.6 LIF as an *in situ* instrument for detecting astrobiological biosignatures

Although there was no clear relationship between LIF results and carbon detected by EDS, it is still highly probable that the LIF results showed evidence of organic molecules, due to the short fluorescence decay periods detected by the time-resolved measurements. Furthermore, it has already been shown by Cockell et al. (2019) that these samples contain microbial colonies, which supports this hypothesis of detection of organic material through LIF.

Despite the issues discussed in Chapter 7 with respect to uneven sample surfaces, the York University LIF instrument was still capable of taking useful measurements. This shows that an instrument with similar capabilities on a Mars rover could be used for both mapping of a sample surface to determine POIs, and directly measuring those POIs to detect possible biosignatures. I believe the most useful aspect of the York University LIF instrument is the time-resolved measurement capabilities with a resolution down to the nanosecond level. None of the current or future Mars rover instruments have this capability, but advancements in technology could lead to its inclusion on a future mission.

9 Conclusions and Recommendations

In this body of research, nine samples collected during two BASALT analogue mission deployments were analyzed. LIF measurements were performed to detect any presence of organic material and characterize their distribution within the rocks. SEM-EDS measurements were performed in order to provide tentative validation of the presence of organic material, and identification of minerals in and around LIF POIs. Pycnometer and μCT measurements were performed to determine the porosity of the samples, providing an additional quantitative physical property to be used in comparison to the LIF and EDS results.

Overall, it was determined that the alteration style of the rocks from Hawai'i had some effect on the distribution and quantity of strong LIF results, with the sample from a relict meteoric fumarole showing the highest amount and intensity of fluorescent material, followed by the samples from active meteoric fumaroles, and the unaltered sample. This is somewhat in agreement with the results from Cockell et al (2019); the weight percent biomass of their samples was highest in the replicate of my relict fumarole sample, but second-highest in the replicate of my unaltered sample and lowest in the replicates of my active fumarole samples. This discrepancy could be explained by a more homogenous distribution of biomass in the unaltered sample, leading to a lower concentration in one area that is more favourably detected by LIF. The alteration style of the rocks from Idaho had no relationship with the LIF results. The ID2016 suite as a whole showed significantly lower amounts of fluorescing material compared to the HI2016 suite, with most of the sample maps showing none at all.

The location of fluorescent material within a sample was not influenced by proximity to a sample edge or sample interior. The only clear location influence was the strong association of fluorescent material with white crystalline material located inside a vesicle, although not all white crystalline material was highly fluorescent. The porosity of a sample similarly had no correlation with the presence and amount of fluorescent material.

Future measurements are necessary to strengthen or refute these conclusions. A further study that involved taking more maps from these and similar samples would provide a much larger sample size and potentially give new insights into the distribution

of fluorescent material within the rocks. More accurate measurements of fluorescence decay times could lead to potential identification of organic molecules. Using an instrument with better carbon-detection capabilities compared to the EDS could provide greater validation of the relationships between fluorescence intensity and carbon content. Finally, there is significant work to be done examining the vesicularity of these samples and their relationships to organic material distribution. Measurements of vesicle sizes and size distribution, as well as permeability, could be used in addition to porosity.

A UV LIF instrument with ns-resolution time-resolved capabilities could be a useful tool for future Mars robotic missions. The lack of substantial sample preparation needed means that LIF mapping and LIF time-resolved measurements can be taken directly on the surface of a sample and leave the sample available for other instrument measurements. LIF could be used for quick detection of organic material, providing POIs needed for further analyses.

References

Abbey, W. J., Bhartia, R., Beegle, L. W., DeFlores, L., Paez, V., Sijapati, K., et al. (2017). Deep UV Raman spectroscopy for planetary exploration: The search for in situ organics. *Icarus*, *290*, 201–214. https://doi.org/10.1016/J.ICARUS.2017.01.039

Abedin, M. N., Bradley, A. T., Sharma, S. K., Misra, A. K., Lucey, P. G., McKay, C. P., et al. (2015). Mineralogy and astrobiology detection using laser remote sensing instrument. *Applied Optics*, *54*(25), 7598. https://doi.org/10.1364/AO.54.007598

Adcock, C. T., Udry, A., Hausrath, E. M., & Tschauner, O. (2018). Craters of the Moon National Monument basalts as unshocked compositional and weathering analogs for martian rocks and meteorites. *American Mineralogist*, *103*(4), 502–516. https://doi.org/10.2138/am-2018-6193

Allwood, A. C., Grotzinger, J. P., Knoll, A. H., Burch, I. W., Anderson, M. S., Coleman, M. L., & Kanik, I. (2009). Controls on development and diversity of Early Archean stromatolites. *Proceedings of the National Academy of Sciences of the United States of America*, *106*(24), 9548–55. https://doi.org/10.1073/pnas.0903323106

Allwood, A. C., Clark, B., Flannery, D., Hurowitz, J., Wade, L., Elam, T., et al. (2015). Texture-specific elemental analysis of rocks and soils with PIXL: The Planetary Instrument for X-ray Lithochemistry on Mars 2020. In *2015 IEEE Aerospace Conference* (pp. 1–13). IEEE. https://doi.org/10.1109/AERO.2015.7119099

Allwood, A. C., Wade, L. A., & Hurowitz, J. A. (2016). PIXL Investigation on the Mars 2020 Rover. In *3rd International Workshop on Instrumentation for Planetary Missions* (p. 4138). https://doi.org/10.1017/S1473550410000273

Amils, R., Fernández-Remolar, D., & IBPSL team. (2014). Río Tinto: A Geochemical and Mineralogical Terrestrial Analogue of Mars. *Life*, *4*(3), 511–534. https://doi.org/10.3390/life4030511

Banerjee, N. R., Izawa, M. R. M., Sapers, H. M., & Whitehouse, M. J. (2011). Geochemical biosignatures preserved in microbially altered basaltic glass. *Surface and Interface Analysis*, *43*(1–2), 452–457. https://doi.org/10.1002/sia.3577

Baqué, M., Verseux, C., Böttger, U., Rabbow, E., Paul De Vera, J.-P., & Billi, D. (2016). Preservation of Biomarkers from Cyanobacteria Mixed with Mars Like Regolith Under Simulated Martian Atmosphere and UV Flux. *Orig Life Evol Biosph*, *46*, 13–

16. https://doi.org/10.1007/s11084-015-9467-9

Beaton, K. H., Chappell, S. P., Abercromby, A. F. J., Miller, M. J., Nawotniak, S. E. K., Brady, A. L., et al. (2019). Using Science-Driven Analog Research to Investigate Extravehicular Activity Science Operations Concepts and Capabilities for Human Planetary Exploration. *Astrobiology*, *19*(3). https://doi.org/10.1089/ast.2018.1861

Beegle, L., Bhartia, R., White, M., Deflores, L., Abbey, W., Wu, Y. H., et al. (2015). SHERLOC: Scanning habitable environments with Raman & luminescence for organics & chemicals. In *IEEE Aerospace Conference Proceedings* (Vol. 2015–June, pp. 1–11). IEEE. https://doi.org/10.1109/AERO.2015.7119105

Bibring, J.-P., Hamm, V., Pilorget, C., Vago, J. L., & the MicrOmega Team. (2017). The MicrOmega Investigation Onboard ExoMars. *Astrobiology*, *17*(6–7), 621–626. https://doi.org/10.1089/ast.2016.1642

Binsted, K. (2015). *Hawai'i Space Exploration Analog and Simulation*.

Bishop, J. L., Dobrea, E. Z. N., McKeown, N. K., Parente, M., Ehlmann, B. L., Michalski, J. R., et al. (2008). Phyllosilicate diversity and past aqueous activity revealed at Mawrth Vallis, Mars. *Science (New York, N.Y.)*, *321*(5890), 830–3. https://doi.org/10.1126/science.1159699

Blake, D., Vaniman, D., Achilles, C., Anderson, R., Bish, D., Bristow, T., et al. (2012). Characterization and Calibration of the CheMin Mineralogical Instrument on Mars Science Laboratory. *Space Science Reviews*, *170*(1–4), 341–399. https://doi.org/10.1007/s11214-012-9905-1

Blanco, A., D'Elia, M., Licchelli, D., Orofino, V., Fonti, S., & Marzo, G. A. (2011). Preservation of biosignatures in clay-rich systems: implications for Martian exobiology. *Memorie Della Societa Astronomica Italiana Supplementi*, *16*, 101–105.

Campbell, J. L., Perrett, G. M., Gellert, R., Andrushenko, S. M., Boyd, N. I., Maxwell, J. A., et al. (2012). Calibration of the Mars Science Laboratory Alpha Particle X-ray Spectrometer. *Space Science Reviews*, *170*(1–4), 319–340. https://doi.org/10.1007/s11214-012-9873-5

Chang, K. (2018, November 19). NASA Mars 2020 Rover Gets a Landing Site: A Crater That Contained a Lake. *The New York Times*.

Christensen, P. R., & Ruff, S. W. (2004). Formation of the hematite-bearing unit in Meridiani Planum: Evidence for deposition in standing water. *Journal of*

Geophysical Research, *109*(E8), E08003. https://doi.org/10.1029/2003JE002233

Clifford, S. M., & Parker, T. J. (2001). The Evolution of the Martian Hydrosphere: Implications for the Fate of a Primordial Ocean and the Current State of the Northern Plains. *Icarus*, *154*, 40–79. https://doi.org/10.1006/icar.2001.6671

Cockell, C. S., Harrison, J. P., Stevens, A. H., Payler, S. J., Hughes, S. S., Kobs Nawotniak, S. E., et al. (2019). A Low-Diversity Microbiota Inhabits Extreme Terrestrial Basaltic Terrains and Their Fumaroles: Implications for the Exploration of Mars. *Astrobiology*, *19*(3), 284–299. https://doi.org/10.1089/ast.2018.1870

Cronin, J. R., & Pizzarello, S. (1983). Amino acids in meteorites. *Advances in Space Research*, *3*(9), 5–18. https://doi.org/10.1016/0273-1177(83)90036-4

Dartnell, L. (2011). Biological constraints on habitability. *Astronomy & Geophysics*, *52*(1), 1.25-1.28. https://doi.org/10.1111/j.1468-4004.2011.52125.x

Dartnell, L. R., & Patel, M. R. (2014). Degradation of microbial fluorescence biosignatures by solar ultraviolet radiation on Mars. *International Journal of Astrobiology*, *13*(2), 112–123. https://doi.org/10.1017/S1473550413000335

Deer, W. A., Howie, R. A., & Zussman, J. (1992). *An Introduction to the Rock-forming Minerals* (2nd ed.). Harlow, Essex, England: Longman Group UK Ltd. https://doi.org/0-582-30094-0

Ehlmann, B. L., Mustard, J. F., Fassett, C. I., Schon, S. C., Head III, J. W., Des Marais, D. J., et al. (2008). Clay minerals in delta deposits and organic preservation potential on Mars. *Nature Geoscience*, *1*(6), 355–358. https://doi.org/10.1038/ngeo207

Ehlmann, B. L., Mustard, J. F., Swayze, G. A., Clark, R. N., Bishop, J. L., Poulet, F., et al. (2009). Identification of hydrated silicate minerals on Mars using MRO-CRISM: Geologic context near Nili Fossae and implications for aqueous alteration. *Journal of Geophysical Research E: Planets*, *114*(10), 1–33. https://doi.org/10.1029/2009JE003339

Ehlmann, B. L., Mustard, J. F., Murchie, S. L., Bibring, J.-P., Meunier, A., Fraeman, A. A., & Langevin, Y. (2011). Subsurface water and clay mineral formation during the early history of Mars. *Nature*, *479*(7371), 53–60. https://doi.org/10.1038/nature10582

Eigenbrode, J. L., Summons, R. E., Steele, A., Freissinet, C., Millan, M., Navarro-González, R., et al. (2018). Organic matter preserved in 3-billion-year-old mudstones at Gale crater, Mars. *Science*, *360*(6393), 1096–1101.

https://doi.org/10.1126/science.aas9185

ESA Media Relations Office. (2016). *Second ExoMars mission moves to next launch opportunity in 2020 / Press Releases / For Media / ESA*.

Eshelman, E., Daly, M. G., Slater, G., Dietrich, P., & Gravel, J.-F. (2014). An ultraviolet Raman wavelength for the in-situ analysis of organic compounds relevant to astrobiology. *Planetary and Space Science*, *93–94*, 65–70. https://doi.org/10.1016/j.pss.2014.01.021

Eshelman, E., Daly, M. G., Slater, G., & Cloutis, E. (2015). Time-resolved detection of aromatic compounds on planetary surfaces by ultraviolet laser induced fluorescence and Raman spectroscopy. *Planetary and Space Science*, *119*, 200–207. https://doi.org/10.1016/j.pss.2015.09.021

Eshelman, E., Daly, M. G., Slater, G., & Cloutis, E. (2017). Detecting aromatic compounds on planetary surfaces using ultraviolet time-resolved fluorescence spectroscopy. *Planetary and Space Science*. https://doi.org/10.1016/j.pss.2017.09.003

Eshelman, E. J. (2016). *STAND-OFF DETECTION OF ORGANIC COMPOUNDS ON MARS USING ULTRAVIOLET RAMAN SPECTROSCOPY AND TIME-RESOLVED LASER-INDUCED FLUORESCENCE*. York University.

Fassett, C. I., Ehlmann, B. L., Head, J. W., Mustard, J. F., Schon, S. C., & Murchie, S. L. (2007). Sedimentary Fan Deposits in Jezero Crater Lake, in the Nili Fossae Region, Mars: Meter- scale Layering and Phyllosilicate-Bearing Sediments. *American Geophysical Union*, *Fall Meeting*(P13D–1562).

Gerard, T. L., & McHenry, L. J. (2012). Fumarole alteration of Hawaiian basalts: A potential Mars analog. In *Geological Society of America Abstracts with Programs* (Vol. 44, pp. 1–8). Milwaukee, Wisconsin: Wisconsin Space Grant Consortium. https://doi.org/10.17307/wsc.v0i0.57

Goesmann, F., Brinckerhoff, W. B., Raulin, F., Goetz, W., Danell, R. M., Getty, S. A., et al. (2017). The Mars Organic Molecule Analyzer (MOMA) Instrument: Characterization of Organic Material in Martian Sediments. *Astrobiology*, *17*(6–7), 655–685. https://doi.org/10.1089/ast.2016.1551

Goetz, W., Brinckerhoff, W. B., Arevalo, R., Freissinet, C., Getty, S., Glavin, D. P., et al. (2018). MOMA: the challenge to search for organics and biosignatures on Mars. https://doi.org/10.1017/S1473550416000227

Goudge, T. A., Mustard, J. F., Head, J. W., Fassett, C. I., & Wiseman, S. M. (2015a). Assessing the mineralogy of the watershed and fan deposits of the Jezero crater paleolake system, Mars. *Journal of Geophysical Research: Planets*, *120*(4), 775–808. https://doi.org/10.1002/2014JE004782

Goudge, T. A., Mustard, J. F., Head, J. W., Fassett, C. I., & Wiseman, S. M. (2015b). Assessing the mineralogy of the watershed and fan deposits of the Jezero crater paleolake system, Mars. *Journal of Geophysical Research: Planets*, *120*(4), 775–808. https://doi.org/10.1002/2014JE004782

Goudge, T. A., Milliken, R. E., Head, J. W., Mustard, J. F., & Fassett, C. I. (2017). Sedimentological evidence for a deltaic origin of the western fan deposit in Jezero crater, Mars and implications for future exploration. *Earth and Planetary Science Letters*, *458*, 357–365. https://doi.org/10.1016/J.EPSL.2016.10.056

Groemer, G., Sattler, B., Weisleitner, K., Hunger, L., Kohstall, C., Frisch, A., et al. (2014). Field Trial of a Dual-Wavelength Fluorescent Emission (L.I.F.E.) Instrument and the Magma White Rover during the MARS2013 Mars Analog Mission. *Astrobiology*, *14*(5), 391–405. https://doi.org/10.1089/ast.2013.1081

Groemer, G., Soucek, A., Frischauf, N., Stumptner, W., Ragonig, C., Sams, S., et al. (2014). The MARS2013 Mars Analog Mission. *Astrobiology*, *14*(5), 360–376. https://doi.org/10.1089/ast.2013.1062

Grotzinger, J. P., Sumner, D. Y., Kah, L. C., Stack, K., Gupta, S., Edgar, L., et al. (n.d.). *A Habitable Fluvio-Lacustrine Environment at Yellowknife Bay, Gale Crater, Mars*.

Haskin, L. A., Wang, A., Jolliff, B. L., McSween, H. Y., Clark, B. C., Des Marais, D. J., et al. (2005). Water alteration of rocks and soils on Mars at the Spirit rover site in Gusev crater. *Nature*, *436*(7047), 66–69. https://doi.org/10.1038/nature03640

Hawaiian Volcano Observatory. (2017). 1969-1974 Mauna Ulu Eruption. Retrieved 4 February 2019, from https://volcanoes.usgs.gov/volcanoes/kilauea/geo_hist_mauna_ulu.html

Hughes, S. S., Haberle, C. W., Kobs Nawotniak, S. E., Sehlke, A., Garry, W. B., Elphic, R. C., et al. (2018). BASALT A: Basaltic Terrains in Idaho and Hawaii as Planetary Analogues for Mars Geology and Astrobiology. *Astrobiology*, *19*(3), ast.2018.1847. https://doi.org/10.1089/ast.2018.1847

Izawa, M. R. M., Banerjee, N. R., Flemming, R. L., Bridge, N. J., & Schultz, C. (2010).

Basaltic glass as a habitat for microbial life: Implications for astrobiology and planetary exploration. *Planetary and Space Science*, *58*(4), 583–591. https://doi.org/10.1016/j.pss.2009.09.014

Jackson, E. D., Stevens, R. E., & Bowen, R. W. (1967). A Computer-Based Procedure for Deriving Mineral Formulas from Mineral Analyses. In W. T. Pecora (Ed.), *Geological Survey Research* (pp. 23–31). Menlo Park, CA: United States Department of the Interior Geological Survey.

Khanna, M., & Stotzky, G. (1992). Transformation of Bacillus subtilis by DNA bound on montmorillonite and effect of DNase on the transforming ability of bound DNA. *Applied and Environmental Microbiology*, *58*(6), 1930–9.

Klingelhöfer, G., Morris, R. V., Bernhardt, B., Rodionov, D., de Souza, P. A., Squyres, S. W., et al. (2003). Athena MIMOS II Mössbauer spectrometer investigation. *Journal of Geophysical Research: Planets*, *108*(E12). https://doi.org/10.1029/2003JE002138

Klingelhöfer, G., Morris, R. V, Bernhardt, B., Schröder, C., Rodionov, D. S., de Souza, P. A., et al. (2004). Jarosite and hematite at Meridiani Planum from Opportunity's Mossbauer Spectrometer. *Science (New York, N.Y.)*, *306*(5702), 1740–5. https://doi.org/10.1126/science.1104653

Kuebler, K. E., Wang, A., Haskin, L. A., & Jolliff, B. L. (2003). A study of olivine alteration to iddingsite using Raman spectroscopy. In Lunar and Planetary Institute (Ed.), *Lunar and Planetary Science Conference* (Vol. 36, p. 1593). The Woodlands, TX, USA: Lunar and Planetary Institute.

Kuntz, M. A., Champion, D. E., Spiker, E. C., Lefebvre, R. H., & McBroome, L. A. (1982). The Great Rift and the Evolution of the Craters of the Moon Lava Field, Idaho. In W. Bonnichsen & R. M. Breckenridge (Eds.), *Cenozoic Geology of Idaho: Idaho Bureau of Mines and Geology Bulletin* (26th ed., pp. 423–437).

Lim, D. S. S., Abercromby, A. F. J., Kobs Nawotniak, S. E., Lees, D. S., Miller, M. J., Brady, A. L., et al. (2019). The BASALT Research Program: Designing and developing mission elements in support of human scientific exploration of Mars. *Astrobiology*, *19*(3), 1–15. https://doi.org/10.1089/ast.2018.1869

Lymer, E. A. (2017). *Laser-Induced Fluorescence Spectroscopy As a Non-Destructive Technique for Mineral and Organic Detection in Carbonaceous Chondrites*. York

University.

Mahaffy, P. R., Webster, C. R., Cabane, M., Conrad, P. G., Coll, P., Atreya, S. K., et al. (2012). The Sample Analysis at Mars Investigation and Instrument Suite. *Space Science Reviews*, *170*(1–4), 401–478. https://doi.org/10.1007/s11214-012-9879-z

Mars Exploration Program Analysis Group, & Hamilton, V. E. (2015). *Mars Science Goals, Objectives, Investigations, and Priorities: 2015 Version Mars Exploration Program Analysis Group (MEPAG)*.

Martín-Torres, F. J., Zorzano, M.-P., Valentín-Serrano, P., Harri, A.-M., Genzer, M., Kemppinen, O., et al. (2015). Transient liquid water and water activity at Gale crater on Mars. *Nature Geoscience*, *8*(5), 357–361. https://doi.org/10.1038/ngeo2412

Maurice, S., Wiens, R. C., Saccoccio, M., Barraclough, B., Gasnault, O., Forni, O., et al. (2012). The ChemCam Instrument Suite on the Mars Science Laboratory (MSL) Rover: Science Objectives and Mast Unit Description. *Space Science Reviews*, *170*(1–4), 95–166. https://doi.org/10.1007/s11214-012-9912-2

McLennan, S. M., Bell, J. F., Calvin, W. M., Christensen, P. R., Clark, B. C., de Souza, P. A., et al. (2005). Provenance and diagenesis of the evaporite-bearing Burns formation, Meridiani Planum, Mars. *Earth and Planetary Science Letters*, *240*(1), 95–121. https://doi.org/10.1016/J.EPSL.2005.09.041

Michalski, J., Poulet, F., Bibring, J.-P., & Mangold, N. (2009). Analysis of phyllosilicate deposits in the Nili Fossae region of Mars: Comparison of TES and OMEGA data. *Icarus*, *206*, 269–289. https://doi.org/10.1016/j.icarus.2009.09.006

Milliken, R. E., Grotzinger, J. P., & Thomson, B. J. (2010). Paleoclimate of Mars as captured by the stratigraphic record in Gale Crater. *Geophysical Research Letters*, *37*(4). https://doi.org/10.1029/2009GL041870

Ming, D. W., Gellert, R., Morris, R. V., Arvidson, R. E., Brückner, J., Clark, B. C., et al. (2008). Geochemical properties of rocks and soils in Gusev Crater, Mars: Results of the Alpha Particle X-Ray Spectrometer from Cumberland Ridge to Home Plate. *Journal of Geophysical Research*, *113*(E12), E12S39. https://doi.org/10.1029/2008JE003195

Newbury, D. E. (2009). Mistakes encountered during automatic peak identification of minor and trace constituents in electron-excited energy dispersive X-ray microanalysis. *Scanning: The Journal of Scanning Microscopies*, *31*(3), 91–101.

https://doi.org/10.1002/sca.20151

Van Olphen, H., & Fripiat, J. J. (1979). *Data Handbook for Clay Materials and Other Non-Metallic Minerals*. London, England, UK: Pergamon Press, Inc.

Orofino, V., Blanco, A., D'Elia, M., Licchelli, D., Fonti, S., & Marzo, G. A. (2010). Study of terrestrial fossils in phyllosilicate-rich soils: Implication in the search for biosignatures on Mars. *Icarus*, *208*(1), 202–206. https://doi.org/10.1016/J.ICARUS.2010.02.028

Osinski, G. R., Battler, M., Caudill, C. M., Francis, R., Haltigin, T., Hipkin, V. J., et al. (2018). The CanMars Mars Sample Return analogue mission. *Planetary and Space Science*.

Poulet, F., Bibring, J.-P., Mustard, J. F., Gendrin, A., Mangold, N., Langevin, Y., et al. (2005). Phyllosilicates on Mars and implications for early martian climate. *Nature*, *438*(7068), 623–627. https://doi.org/10.1038/nature04274

Preston, L. J., & Dartnell, L. R. (2018). Planetary habitability: lessons learned from terrestrial analogues. https://doi.org/10.1017/S1473550413000396

Quantin, C., Carter, J., Thollot, P., Broyer, J., Lozach, L., Davis, J., et al. (2015). Oxia Planum: a suitable landing site for ExoMars 2018 Rover. In *European Planetary Science Congress* (p. 704). Nantes, France: European Planetary Science Congress.

Rieder, R., Gellert, R., Brückner, J., Klingelhöfer, G., Dreibus, G., Yen, A., & Squyres, S. W. (2003). The new Athena alpha particle X-ray spectrometer for the Mars Exploration Rovers. *Journal of Geophysical Research: Planets*, *108*(E12). https://doi.org/10.1029/2003JE002150

Rieder, R., Gellert, R., Anderson, R. C., Brückner, J., Clark, B. C., Dreibus, G., et al. (2004). Chemistry of rocks and soils at Meridiani Planum from the Alpha Particle X-ray Spectrometer. *Science* , *306*(5702), 1746–9. https://doi.org/10.1126/science.1104358

Ross, A., Kosmo, J., & Janoiko, B. (2013). Historical synopses of desert RATS 1997–2010 and a preview of desert RATS 2011. *Acta Astronautica*, *90*(2), 182–202. https://doi.org/10.1016/J.ACTAASTRO.2012.02.003

Ruff, S. W., & Farmer, J. D. (2016). Silica deposits on Mars with features resembling hot spring biosignatures at El Tatio in Chile. *Nature Communications*, *7*(1), 1–10. https://doi.org/10.1038/ncomms13554

Ruff, S. W., Farmer, J. D., Calvin, W. M., Herkenhoff, K. E., Johnson, J. R., Morris, R. V., et al. (2011). Characteristics, distribution, origin, and significance of opaline silica observed by the Spirit rover in Gusev crater, Mars. *Journal of Geophysical Research*, *116*(E7), E00F23. https://doi.org/10.1029/2010JE003767

Rull, F., Maurice, S., Hutchinson, I., Moral, A., Perez, C., Diaz, C., et al. (2017). The Raman Laser Spectrometer for the ExoMars Rover Mission to Mars. *Astrobiology*, *17*(6–7), 627–654. https://doi.org/10.1089/ast.2016.1567

De Sanctis, M. C., Altieri, F., Ammannito, E., Biondi, D., De Angelis, S., Meini, M., et al. (2017). Ma_MISS on ExoMars: Mineralogical Characterization of the Martian Subsurface. *Astrobiology*, *17*(6–7), 612–620. https://doi.org/10.1089/ast.2016.1541

Sapers, H. M., Osinski, G. R., Banerjee, N. R., & Preston, L. J. (2014). Enigmatic tubular features in impact glass. *Geology*, *42*(6), 471–474. https://doi.org/10.1130/G35293.1

Sapers, H. M., Banerjee, N. R., & Osinski, G. R. (2015). Potential for impact glass to preserve microbial metabolism. *Earth and Planetary Science Letters*, *430*, 95–104. https://doi.org/10.1016/j.epsl.2015.08.011

Sapers, H. M., Banerjee, N. R., & Osinski, G. R. (2015). Potential for impact glass to preserve microbial metabolism. *Earth and Planetary Science Letters*, *430*, 95–104. https://doi.org/10.1016/J.EPSL.2015.08.011

Schiffman, P., Zierenberg, R., Marks, N., Bishop, J. L., & Dyar, M. D. (2006). Acid-fog deposition at Kilauea volcano: A possible mechanism for the formation of siliceous-sulfate rock coatings on Mars. *Geology*, *34*(11), 921. https://doi.org/10.1130/G22620A.1

Schon, S. C., Head, J. W., & Fassett, C. I. (2012). An overfilled lacustrine system and progradational delta in Jezero crater, Mars: Implications for Noachian climate. *Planetary and Space Science*, *67*(1), 28–45. https://doi.org/10.1016/J.PSS.2012.02.003

Seelos, K. D., Arvidson, R. E., Jolliff, B. L., Chemtob, S. M., Morris, R. V, Ming, D. W., & Swayze, G. A. (2010). Silica in a Mars analog environment: Ka'u Desert, Kilauea Volcano, Hawaii. *J. Geophys. Res*, *115*, 0–15. https://doi.org/10.1029/2009JE003347

Sehlke, A., Mirmalek, Z., Burtt, D., Haberle, C., Santiago-Materese, D., Kobs Nawotniak,

S. E., et al. (2019). Requirements for Portable Instrument Suites During Human Scientific Exploration of Mars. *Astrobiology*, *in press*, 1–50.

Skulinova, M., Lefebvre, C., Sobron, P., Eshelman, E., Daly, M., Gravel, J.-F., et al. (2014a). Time-resolved stand-off UV-Raman spectroscopy for planetary exploration. *Planetary and Space Science*, *92*, 88–100. https://doi.org/10.1016/J.PSS.2014.01.010

Skulinova, M., Lefebvre, C., Sobron, P., Eshelman, E., Daly, M., Gravel, J.-F., et al. (2014b). Time-resolved stand-off UV-Raman spectroscopy for planetary exploration. https://doi.org/10.1016/j.pss.2014.01.010

Smith, H. D., McKay, C. P., Duncan, A. G., Sims, R. C., Anderson, A. J., & Grossl, P. R. (2014). An instrument design for non-contact detection of biomolecules and minerals on Mars using fluorescence. *Journal of Biological Engineering*, *8*(1), 16. https://doi.org/10.1186/1754-1611-8-16

Squyres, S. W., & Kasting, J. F. (1994). Early Mars: how warm and how wet? *Science (New York, N.Y.)*, *265*(5173), 744–9. https://doi.org/10.1126/SCIENCE.265.5173.744

Squyres, S. W., Grotzinger, J. P., Arvidson, R. E., Bell, J. F., Calvin, W., Christensen, P. R., et al. (2004). In situ evidence for an ancient aqueous environment at Meridiani Planum, Mars. *Science (New York, N.Y.)*, *306*(5702), 1709–14. https://doi.org/10.1126/science.1104559

Stevens, A. H., Kobs Nawotniak, S. E., Garry, W. B., Payler, S. J., Brady, A. L., Miller, M., et al. (2019). Tactical Scientific Decision-Making During Crewed Astrobiology Mars Missions. *Astrobiology*, *19*(3). https://doi.org/10.1089/ast.2018.1837

Stout, M. Z., Nicholls, J., & Kuntz, M. A. (1994). Petrological and Mineralogical Variations in 2500-2000 yr B.P. Lava Flows, Craters of the Moon Lava Field, Idaho*. *Journal of Petrology*, *35*(6), 1681–1715.

Vago, J. L., Westall, F., Coates, A. J., Jaumann, R., Korablev, O., Rie Ciarletti, V., et al. (2017). ExoMars Rover Mission Habitability on Early Mars and the Search for Biosignatures with the ExoMars Rover Landing Site Selection Working Group. *Astrobiology*, *17*(6–7), 471–511. https://doi.org/10.1089/ast.2016.1533

Vinet, N., & Higgins, M. D. (2010). Magma Solidification Processes beneath Kilauea Volcano, Hawaii: a Quantitative Textural and Geochemical Study of the 1969-1974

Mauna Ulu Lavas. *Journal of Petrology*, *51*(6), 1297–1332. https://doi.org/10.1093/petrology/egq020

Voit, G. M. (1992). Destruction and survival of polycyclic aromatic hydrocarbons in active galaxies. *Monthly Notices of the Royal Astronomical Society*, *258*(4), 841–848. https://doi.org/10.1093/mnras/258.4.841

Wacey, D. (2010). Stromatolites in the ~3400 Ma Strelley Pool Formation, Western Australia: Examining Biogenicity from the Macro- to the Nano-Scale. *Astrobiology*, *10*(4), 381–395. https://doi.org/10.1089/ast.2009.0423

Westall, F., Foucher, F., Bost, N., Bertrand, M., Loizeau, D., Vago, J. L., et al. (2015). Biosignatures on Mars: What, Where, and How? Implications for the Search for Martian Life. *Astrobiology*, *15*(11), 998–1029. https://doi.org/10.1089/ast.2015.1374

Wiens, R. C., Newell, R., Clegg, S., Sharma, S. K., Misra, A., Bernardi, P., et al. (2017). THE SUPERCAM REMOTE RAMAN SPECTROMETER FOR MARS 2020. In *48th Lunar and Planetary Science Conference* (p. 2600). The Woodlands, TX: Lunar and Planetary Institute. https://doi.org/10.1109/AERO

Wiens, R. C., Maurice, S., & Rull Perez, F. (2017). *The SuperCam remote sensing instrument suite for the Mars 2020 rover mission: A preview*. Los Alamos, NM, USA.

Williams, R. M. E., Grotzinger, J. P., Dietrich, W. E., Gupta, S., Sumner, D. Y., Wiens, R. C., et al. (2013). Martian Fluvial Conglomerates at Gale Crater. *Science*, *340*(6136), 1068–1072. https://doi.org/10.1126/science.1237068